eISSN: 3108-5202

TRANSACTIONS ON

COMPUTATIONAL MODELING AND INTELLIGENT SYSTEMS

Volume 4, July 2026

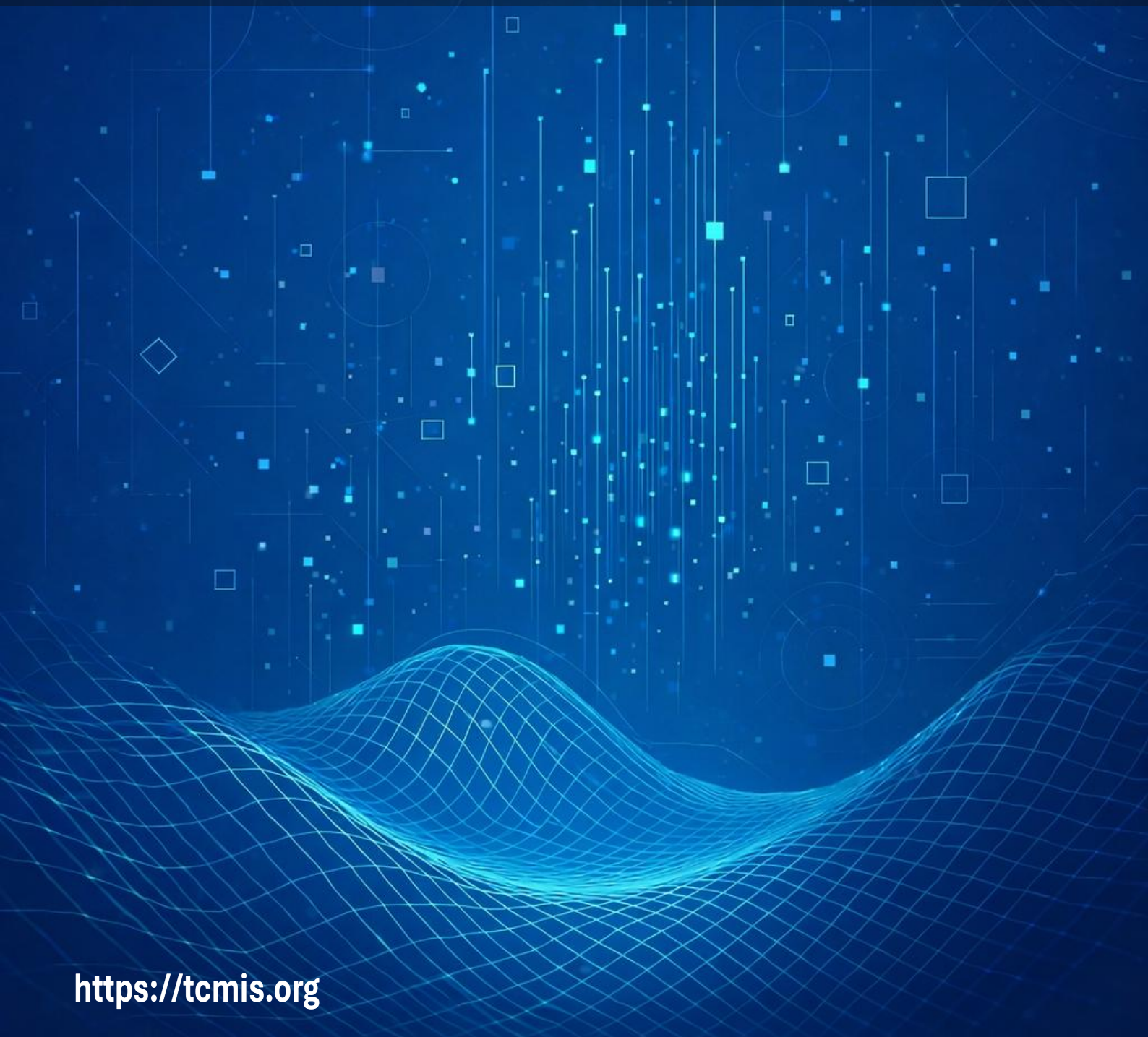

https://tcmis.org

Transactions on Computational Modeling and Intelligent Systems

Volume 4, July 2026

eISSN:

3108-5202

Editor-in-Chief:

Prof. Dumitru Baleanu
Institute of Space Sciences, Bucharest, Romania

Official Title:

Transactions on Computational Modeling and Intelligent Systems

Official Abbreviation:

Transact Comput Model Intell Syst

Publisher:

Gülşen Yaman

Publication Period:

Quarterly (in January, April, July, October)

Webpage:

https://tcmis.org

Email:

editor@tcmis.org

SCREENED BY iThenticate Professional Plagiarism Prevention

Crossref

Area Editors

Operational Research and Optimization

Gerhard W. Weber, Poznan University of Technology, Poland

Applied Mathematics and Control

Necati Ozdemir, Balikesir University, Turkiye
Zakia Hammouch, Moulay Ismail University, Morocco

Computational Modelling & Simulation

Guo-Cheng Wu, Chongqing University of Posts and Telecom., China

Intelligent Systems

Mukund N. Janardhanan, University of Warwick, United Kingdom

Editorial Board *(in alphabetical order)*

Amar Debbouche, Guelma University, Algeria
Zakia Hammouch, Moulay Ismail University, Morocco
Hossein Jafari, Department of Mathematics, University of South Africa, South Africa
Amin Jajarmi, University of Bojnord, Iran
Mukund N. Janardhanan, University of Warwick, United Kingdom
Yeliz Karaca, University of Massachusetts, United States
Luis Vázquez Martínez, Universidad Complutense de Madrid, Spain
Necati Ozdemir, Balikesir University, Turkiye
Mirco Peron, NEOMA Business School, France
Anett Rácz, University of Debrecen, Hungary
Jocelyn Sabatier, Bordeaux Université, France
Achyut Shankar, Bennett University, India
Gerhard W. Weber, Poznan University of Technology, Poland
Guo-Cheng Wu, Chongqing University of Posts and Telecommunications, China

English Language Editor *(in alphabetical order)*

Dilek Inan, Izmir Democracy University, Turkiye

Abstracted & Indexed in:

Crossref, DOAJ, Google Scholar, Harvard Hollis, OpenAIRE, OpenAlex, Research Commons, Worldcat OCLC

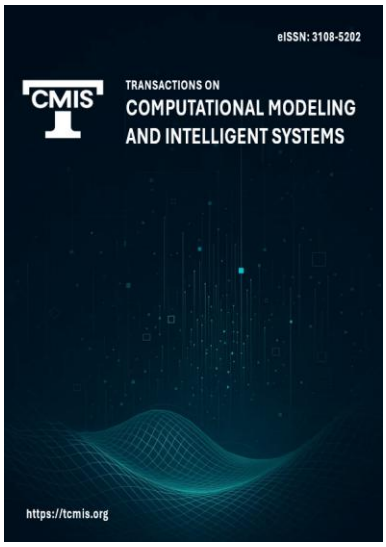

Volume 4, July 2026

Transactions on Computational Modeling and Intelligent Systems

eISSN: 3108-5202

Webpage: https://tcmis.org

An international peer-reviewed open-access journal published quarterly

CONTENTS (Article ID, Title and Authors)

Research Articles

10063 Simulation analysis of multi-objective one-dimensional cutting problems

Anett Rácz, Ákos Szabó

10078 Conformable sliding mode control and analysis of Lorenz chaotic system

Haris Calgan, Metin Demirtas

10023 Application of Upadhyaya transforms with machine learning for predictive and analytical solutions in complex systems

Yamini Parthiban, Raghavendran Prabakaran, Dinesh Thakur, Srinivasan Madhumitha

10092 A machine-learning decision support system for demand-driven nurse staffing in outpatient clinics: Design and validation at an Indonesian public hospital

Muhammad Fadhillah Hadi, Asmuliardi Muluk

10087 Nonlinear buoyancy-driven thermal energy transport on a moving vertical plate with boundary slips and non-uniform heat source/sink

Astick Banerjee, Sohita Rajput, Krishnendu Bhattacharyya, Mitu Dular, Dimpal Sharma, Sanat Kumar Mahato

10080 Comparative study on heat and mass transfer performance of ternary hybrid nanoliquid over an exponentially stretching surface

Gangadhar Poojari Ashwinkumar, Uppar Shivakumar, Bhandare Ranjana, Pradeep Nanda

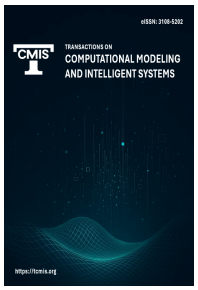

Transactions on
Computational Modeling
and Intelligent Systems

Volume 4, July 2026, Article 10063
https://doi.org/10.65112.tcmis.10063

eISSN: 3108-5202
www.tcmis.org

RESEARCH ARTICLE

Simulation analysis of multi-objective one-dimensional cutting problems

Anett Rácz[1,*] and Ákos Szabó[1]

[1] *Department of Applied Mathematics and Probability Theory, University of Debrecen, Debrecen, Hungary.*
[*] *Corresponding Author. Email: racz.anett@inf.unideb.hu (A. Rácz)*

Article Information

Received: 27 January 2026
Accepted: 22 June 2026
Published 11 July 2026

AMS Classification:
90-10, 90C11

Abstract

In this paper, we compare published studies about optimization models for multi-objective one-dimensional cutting problems. Although all of the models address multiple objectives, they implement these goals in different ways. Some focus primarily on minimizing the amount of waste while setting limits on reusable bars returned to stock, whereas others combine these criteria with additional factors, such as the number of affected bars and the number of cuts. First, we provide a brief overview of these mathematical models, including one developed and published by the authors earlier, as well as three others from the existing literature that pursue objectives very similar to ours. In addition to comparing the models based on the included objectives such as the number of cuts, the amount of waste, and the number of reusable bars, our goal was also to analyse the computational requirements and limitations of the models in case of large-scale problems.

Keywords: Mixed integer programming, one-dimensional cutting problems, simulation

1. Introduction

The one-dimensional cutting stock problem (1DCSP) involves a set of available one-dimensional stock items (referred to as bars) in order to serve smaller required pieces (referred as orders) in specified lengths and quantities.

In today's competitive industrial environment the optimization problems related to cutting raw materials are of critical importance for companies. Cutting stock problems have numerous application areas in industrial sectors, such as construction and civil engineering [1], steel industry [2], woodworking [3] and many other fields, where efficient solutions have a direct impact on production costs and the amount of waste generated. More recently, [4] combined building information modelling (BIM) with a multi-objective cutting-pattern optimization to reduce rebar cutting waste in construction projects, again balancing several practical objectives within a single pipeline. Researchers have moved beyond the classical single-objective CSP model, which focuses solely on waste minimization, and now focus on more complex multi-objective variants that more accurately reflect real industrial environments. In practice, multi-objective one-dimensional cutting optimization models may aim to achieve several objectives simultaneously, including:

- minimizing the number of required cuts,

- reducing the amount of waste produced,
- minimizing the number of stock bars involved.

The following research directions have received particular attention:

- **Integrated models:** Several studies, such as [5], focus on integrating the lot-sizing and cutting stock problems. These kinds of studies investigate how production quantities and cutting patterns can be optimized simultaneously, with the aim of minimizing setup costs and inventory levels.
- **Side constraints:** There is a growing number of models that incorporate additional practical considerations. Model of [6] implements cutting setups and open stacks, which are critical in the paper and tube manufacturing industries for improving production efficiency and reducing logistical challenges.
- **Usable leftovers**: The handling of reusable remainders, which is also a central concern of MACROPT-1D, has recently been revisited in the literature. Senergues et al. [7] published an updated and comprehensive review of the cutting stock problem with usable leftovers (CSPUL), extending the earlier survey of Cherri et al. [8] with more than fifty studies published after 2008; unlike our comparative simulation study, however, this work remains a literature synthesis and does not provide a numerical, model-to-model comparison.

  Ma et al. [9] extended the usable-leftover concept to a two-dimensional, multi-objective steel-cutting problem minimizing waste area, order overrun, and slitter adjustments. As the problem is two-dimensional and thus structurally different from the models compared here, it is solved with an iterated local search heuristic rather than an exact MILP solver.
- **New algorithmic approaches:** Due to the computational complexity of the CSP, new heuristics and metaheuristics are continuously being developed. Recent studies also demonstrate the increasing adoption of artificial intelligence–based methods, such as [10] and tree-based heuristics [11], which aim to significantly reduce computational time while maintaining solution quality. Similarly, [12] proposed a column-generation-based local branching matheuristic for a multi-period cutting stock problem with due dates and setups, in which the objective combines tardiness, earliness, and setup costs; their results confirm that as additional objectives and side constraints are introduced, exact solution approaches—such as the four MILP models compared in this paper—face rapidly increasing computational demands, which is consistent with the runtime behavior we report in Section 3.6.

1.1. Contributions of this study

The aim of this study is to analyze and compare our previously published **M**ultiobjective, **A**djustable **C**ost and **R**ecycling parametric **OPT**imization model for **1D**imensional cutting stock problems (MACROPT-1D) [13] with three other theoretical models proposed in the literature: the two mixed-integer linear programming formulations of Abuabara and Morabito (A&Mv1 and A&Mv2) [14], and the multi-objective model of Trkman and Gradišar (T&G) [15]. The comparison considers not only the objectives of the models, such as cost or waste reduction, but also implementation aspects, practical applicability, and computational performance, including runtime behavior. Although several multi-objective formulations of the one-dimensional cutting stock problem exist, including the models discussed above, they are typically validated either on small illustrative examples or evaluated only with respect to their own native objective function. As a result, it remains unclear how these models behave on criteria that are not part of their own objective, for instance, the number of cuts produced by a waste-only model, or the number of stock bars affected by a cost-minimizing model. This gap motivates the specific contributions of the present study, which can be summarized as follows.

- We conduct a large-scale simulation study comprising 900 randomly generated instances, structured into nine scenario groups along two independent dimensions (stock level and order volume), in contrast to the small numerical examples typically used to validate such models in the literature.

- We cross-evaluate all four models with respect to five criteria simultaneously: the number of cuts, the amount of waste, the number of affected bars, the total cost, and the runtime, regardless of which of these criteria is part of a model's own objective, in order to reveal trade-offs that may remain hidden when a model is assessed only against its native objective function.
- We investigate whether the parametric flexibility of MACROPT-1D, which allows the relative importance of cutting cost, waste, and the number of bars used to be tuned through three independent coefficients, without altering the model structure, translates into a measurable advantage over models with a fixed or more restrictive objective, such as A&Mv1, A&Mv2, and T&G.
- We examine the theoretical correctness of the compared formulations, with particular attention to the logical relationship between the binary indicator variables governing bar usage and the return of remainders to stock in the A&Mv2 model.

2. Theoretical background of selected 1DCS models

In this section we provide a brief overview of the models that were implemented, analyzed, and compared in Python. The models presented in this study are based on the papers reviewed in the survey [8], complemented by our MACROPT-1D model published in [13]. In [8], the authors highlight and discuss the following one-dimensional cutting stock models: two versions of a waste minimization model proposed by Abuabara and Morabito [14] and the multi-objective model of Trkman and Gradišar [15], which incorporates not only the amount of waste but also the cost associated with returning reusable-length bars to inventory within the objective function. These models were selected for comparison and analysis. In the following section, we provide an overview of the models, beginning with the general notation in table 1.

Table 1. Notation.

Input data	
Symbol	Description
$B_1, B_2, \ldots, B_m$	Bars available in stock.
$O_1, O_2, \ldots, O_n$	Orders, that should be served.
$bl_1, bl_2, \ldots, bl_m$	Length of the bars in stock.
$ol_1, ol_2, \ldots, ol_n$	Requested length of the orders.
W	Waste limit, below which a remaining part is considered waste.
cC	Cost of a cut.
wP	Penalty associated with the generated waste, expressed on a per-unit basis.
rC	Recycling cost, i.e. the cost of returning a part back to stock.
Variables, technological constants	
Symbol	Description
x_{ij}	Elements of an $n \times m$ binary matrix assigning orders to stock bars.
$Rl_1, Rl_2, \ldots, Rl_m$	Residual length of a stock bar after cutting.
$Wl_1, Wl_2, \ldots, Wl_m$	Waste length of a stock bar after cutting.
$YU_1, YU_2, \ldots, YU_m$	Binary variable indicating whether a bar is involved.
$YR_1, YR_2, \ldots, YR_m$	Binary variable indicating whether a stock bar has a remainder.
$YRC_1, YRC_2, \ldots, YRC_m$	Binary variable indicating whether the remainder of a stock bar is reusable.
$YRT_1, YRT_2, \ldots, YRT_m$	Binary variable indicating whether the remainder returns to stock.
M	Large enough constant.
ϵ	Small enough constant.

2.1. MACROPT-1D

We developed a multi-objective mixed-integer linear programming (MILP) model for one-dimensional cutting stock problem. The model minimizes a linear combination of the number of cuts, weighted by the cut cost coefficient (cC), the resulting waste, weighted by the waste coefficient (wP) and the number of stock bars used to fulfill the orders. The model includes constraints that set remainder lengths (Rl_j) and the binary indicator variables (Wl_j, YU_j) according

to the waste length limit and utilization of stock bars $j = 1, 2, \ldots, m$. In this section we give a brief overview of the model, for detailed explanation see [13].

$$\begin{aligned} \min \quad & cC \cdot \sum_{j=1}^{m} \left(\sum_{i=1}^{n} (x_{ij}) - 1 + YR_j \right) \\ & + wP \cdot \sum_{j=1}^{m} Wl_j \\ & + \sum_{j=1}^{m} YU_j \end{aligned} \tag{1}$$

st.

$$\sum_{i=1}^{n} x_{ij} ol_i + Rl_j = bl_j \qquad j = 1, 2, \ldots, m \tag{2}$$

$$\sum_{j=1}^{m} x_{ij} = 1 \qquad i = 1, 2, \ldots, n \tag{3}$$

$$YR_j \geq \frac{Rlj}{bl_j} \qquad j = 1, 2, \ldots, m \tag{4}$$

$$Rl_j - Wl_j \leq M \cdot YRC_j \qquad j = 1, 2, \ldots, m \tag{5}$$

$$W - Rl_j \leq M \cdot (1 - YRC_j) \qquad j = 1, 2, \ldots, m \tag{6}$$

$$YU_j \geq 1 - \frac{Rl_j}{bl_j} \qquad j = 1, 2, \ldots, m. \tag{7}$$

Objective function (1) combines three goals: minimizing the cutting cost, the waste penalty and the number of stock bars used. Constraint (2) ensures that the length of each stock bar is equal to the total length of the orders assigned to it plus the length of the remainder. Equation (3) guarantees a unique assignment of every order to a stock bar. (4) sets the appropriate value of the binary variables YR_j, while the subsequent pair of constraints provides an if-then logical formulation that equates the waste length to the remainder length whenever it is below the waste limit. Finally, (7) sets the value of the binary variables YU_j depending on their usage.

2.2. 1st version model of Abuabara and Morabito

The next model is a mixed integer linear programming model from Abuabara and Morabito, [14] (A&Mv1). This single objective model was developed for solving the cutting stock problem arising in the processing of metal structural tubes with the minimization of the waste. We give a short overview of the model, for more detailed explanation see [14].

$$\min \sum_{j=1}^{m} Wl_j \tag{8}$$

$$\sum_{i=1}^{n} x_{ij} ol_i + Rl_j = bl_j \qquad j = 1, 2, \ldots, m \tag{9}$$

$$\sum_{j=1}^{m} x_{ij} = 1 \qquad i = 1, 2, \ldots, n \tag{10}$$

$$YU_j \leq \sum_{i=1}^{n} x_{ij} \qquad j = 1, 2, \ldots, m \tag{11}$$

$$M \cdot YU_j \geq \sum_{i=1}^{n} x_{ij} \qquad j = 1, 2, \ldots, m \tag{12}$$

$$Rl_j - W \geq -M \cdot (1 - YRC_j) + \epsilon \qquad j = 1, 2, \ldots, m \tag{13}$$

$$Rl_j - W \leq M \cdot YRC_j \qquad j = 1, 2, \ldots, m \tag{14}$$

$$Wl_j - M \cdot (1 - YRC_j) \leq 0 \qquad j = 1, 2, \ldots, m \tag{15}$$

$$Wl_j - M \cdot YU_j \leq 0 \qquad j = 1, 2, \ldots, m \tag{16}$$

$$-Rl_j + Wl_j \leq 0 \qquad j = 1, 2, \ldots, m \tag{17}$$

$$Rl_j - Wl_j + M \cdot (1 - YRC_j) + M \cdot YU_j \leq 2M \qquad j = 1, 2, \ldots, m \tag{18}$$

$$-YU_j + YRT_j \leq 0 \qquad j = 1, 2, \ldots, m \tag{19}$$

$$(1 - YRC_j) + YRT_j \leq 1 \qquad j = 1, 2, \ldots, m \tag{20}$$

$$YU_j - (1 - YRC_j) - YRT_j \leq 0 \qquad j = 1, 2, \ldots, m \tag{21}$$

$$\sum_{j=1}^{m} YRT_j \leq 1 \tag{22}$$

Objective (8) minimizes the total waste generated during the cutting process. Constraint (9), and (10) relate to the total length and order-to-bar assignments, analogous to (2) and (3). In Abuabara's 1st version model, the values of the binary variables YU_j, which represent bar usage, are determined by constraints (11) and (12), while the variables YRC_j are set by (13) and (14) using the waste limit W. Following constraints (15) and (16) ensure that if the remainder is reusable (i.e. $YRC_j = 1$) then no waste is generated on bar j (i.e. $Wl_j = 0$), and vice versa. This requirement is extended with (17), which guarantees that the length of the waste cannot be larger than the length of the remainder. Next one is a compound logical relationship that ensures the coordinated assignment of values to the corresponding variables. The constraint (18) restricts the values of the remainder and waste variables only if the given stock bar is used ($YU_j = 1$) and not reusable ($YRC_j = 0$). In this case, the entire remainder must be considered as waste. (19) states that a remainder can be returned to stock (YRT_j) if the corresponding bar has actually been used ($YU_j = 1$), while (20) ensures that a non reusable remainder ($YRC_j = 0$) cannot be returned to stock ($YRT_j = 0$). Finally, the last two constraints (21) and (22) formulate a special requirement of the real life application, they operate such that if multiple remainders of reusable length are generated, the model allows only one of them to be actually returned to stock. In all other cases, the variable YRC_j is forced to zero. This is achieved by modifying the cutting plan so that the corresponding remainder lengths do not reach the reusability threshold.

2.3. 2nd version model of Abuabara and Morabito

The authors of [14] simplified the previous model and corrected some infeasibility issues in the second version. We now provide a brief overview of this revised model (A&Mv2). Detailed explanation can be found in the mentioned paper.

$$\min \sum_{j=1}^{m} Wl_j \tag{23}$$

$$\sum_{i=1}^{n} x_{ij} ol_i \leq bl_j \qquad j = 1, 2, \ldots, m \tag{24}$$

$$\sum_{j=1}^{m} x_{ij} = 1 \qquad i = 1, 2, \ldots, n \tag{25}$$

$$W \cdot YRT_j \leq bl_j \cdot YU_j - \sum_{i=1}^{n} x_{ij} ol_i \qquad j = 1, 2, \ldots, m \tag{26}$$

$$Wl_j + YRT_j \cdot M \geq bl_j \cdot YU_j - \sum_{i=1}^{n} x_{ij} ol_i \qquad j = 1, 2, \ldots, m \tag{27}$$

$$\sum_{j=1}^{m} YRT_j \leq 1 \tag{28}$$

Besides the conditions identical to those of the first version, constraint (26) establishes a relationship between the remainder length on a given bar and its return to stock. Furthermore, constraint (27) ensures that any unused material is classified either as waste or as a sufficiently long remainder returned to inventory.

2.4. Multi-objective model of Trkman and Gradisar

Finally, we selected a model very similar to ours, which incorporates a linear combination of multiple goals in its objective [15]. In this section we give a brief overview of the Trkman model (T&G), for more details see the mentioned paper.

$$\min \sum_{j=1}^{m} Wl_j \cdot wP + YRT_j \cdot rC \tag{29}$$

$$\sum_{i=1}^{n} x_{ij} ol_i + Rl_j = bl_j \cdot YU_j \qquad j = 1, 2, \ldots, m \tag{30}$$

$$\sum_{j=1}^{m} x_{ij} = 1 \qquad i = 1, 2, \ldots, n \tag{31}$$

$$W - Rl_j + W \cdot (YRT_j - 1) \leq 0 \qquad j = 1, 2, \ldots, m \tag{32}$$

$$Rl_j - Wl_j - (YRT_j + (1 - YU_j)) \cdot \max_k \{bl_k\} \leq 0 \qquad j = 1, 2, \ldots, m \tag{33}$$

Constraints (30) and (31) are about the length balance and order-to-bar assignment analogous to those in the previous models. (32) ensures that the remainder is returned to stock if and only if its length exceeds the waste limit W. Constraint (33) manages the two possible states of a remainder, namely, being returned to stock or being treated entirely as waste.

3. Computational tests and comparison

3.1. Experimental Design and Computational Environment

The models were implemented in the Python programming language and solved by GUROBI solver. For the purposes of the simulation experiments, the test instances were categorized based on the level of the stock and volume of the orders into the groups presented in Table 2. For each scenario (LIL-LOV, ..., HIL-HOV), 100 randomly generated problem instances were created, each comprising the number and dimensions of stock bars as well as the orders.

Although fixed priority coefficients were employed for the different objectives (number of cuts, amount of waste, and number of stock bars used), the results were also analyzed separately according to each objective. The corresponding input parameters were as follows:

- Cost of cuts was fixed to 400, i.e. $cC = 400$.
- Penalty associated with the waste, on a per unit basis was fixed to 100, i.e. $wP = 100$.
- Recycling cost was 200, i.e. $rC = 200$.
- We used a waste limit fixed to 45, i.e. $W = 45$.

In the graphs, plots, and figures, the models are identified using the following colors and abbreviations:

Table 2. Scenario groups.

	Low Inventory Level (LIL) $5 < m \leq 80$	Medium Inventory Level (MIL) $80 < m \leq 100$	High Inventory Level (HIL) $100 < m \leq 150$
Low Order Volume (LOV) $5 < n \leq 10$	LIL - LOV	MIL - LOV	HIL - LOV
Medium Order Volume (MOV) $10 < n \leq 20$	LIL - MOV	MIL - MOV	HIL - MOV
High Order Volume (HOV) $20 < n \leq 30$	LIL - HOV	MIL - HOV	HIL - HOV

- Multi-objective, adjustable cost and recycling parametric optimization model [13] - MACROPT-1D, is highlighted by blue.
- First version of the mixed integer linear programming model of Abuabara and Morabito [14], (A&Mv1) is highlighted by orange.
- For the second version of the mixed integer linear programming model of Abuabara and Morabito [14], (A&Mv2) we use red.
- The multi-objective model of Trkman and Gradisar (T&G) is labelled by green.

Experiments were conducted on a Toshiba Satellite C50-A-1JV PC with Intel Pentium N3520 4 core CPU (2.16 GHz), and 4 GB DDR3 RAM.

3.2. Comparison of the number of cuts

In this section, we compare the number of cuts as a performance metric. Although the objective functions of the models differ, it is essential to evaluate the optimal solutions with respect to this common criterion, namely the number of cuts, irrespective of the associated cost coefficient.
Figure 1 presents box plots of the number of cuts, grouped by stock level across three different scenarios (LIL, MIL, and HIL).

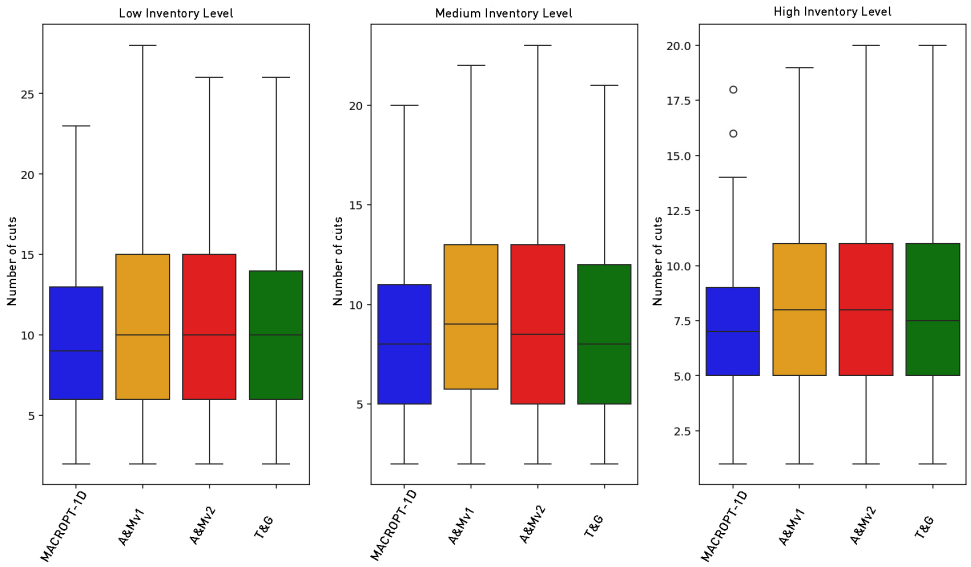

Figure 1. Comparison of the number of cuts in the optimal solutions across models

The objective functions of models A&Mv1 and A&Mv2 focus on waste minimization and do not explicitly account for the number of cuts; therefore, it is expected that these models perform the

worst with respect to this criterion. In contrast, the MACROPT-1D and T&G models employ similar multi-objective formulations, in which identical cost coefficients were applied. The results shown in the figures indicate that MACROPT-1D offers better cutting plans in terms of the number of cuts, and consequently, in cutting costs as well.

3.3. Comparison of the generated waste

In this section, we focus exclusively on the amount of waste generated. This objective is common to all four models. The objective functions of the A&Mv1 and A&Mv2 models are solely devoted to waste minimization, whereas the MACROPT-1D and T&G models include waste minimization in combination with other objectives.

Figure 2 shows the boxplots of generated waste in the three mentioned category, from low to high stock level.

The first observation we highlight, is that cutting tasks generate less waste when a larger inventory is available. This outcome is logically expected and is consistently confirmed by the simulation results. This is unsurprising, as a greater stock variety provides increased flexibility in matching orders to stock lengths, thereby enabling more efficient material utilization.

A more unexpected result, however, is that although the A&Mv1 and A&Mv2 models exclusively aim at waste minimization, they nevertheless produce cutting plans associated with the highest amounts of waste compared to the other two models (MACROPT-1D and T&G). This behavior is presumably attributable to the constraint limiting the number of stock bars returned to the inventory. This restriction is intended to prevent the accumulation of a large variety of stock bars with different lengths, which may be difficult to track and could increase administrative complexity.

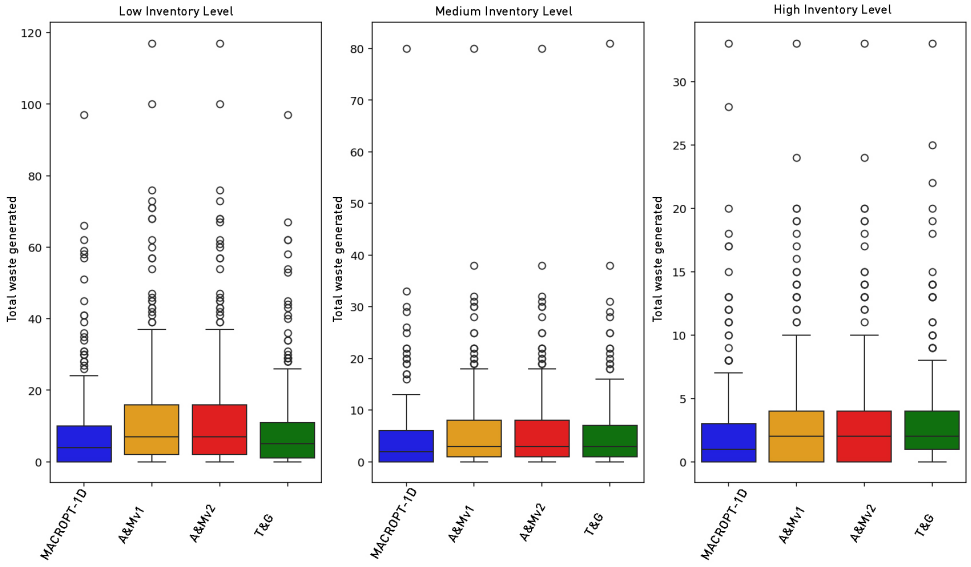

Figure 2. Comparison of the waste generated in the optimal solutions across models

3.4. Comparison of the affected bars

If the objective is waste minimization itself, the most straightforward approach would be to generate cutting patterns in which the residual length just exceeds the reusability threshold W. In this case, the leftover is not classified as waste but is returned to inventory. While this strategy is mathematically optimal, it is not necessarily desirable from a business perspective, as it may lead to inventory explosion and excessive heterogeneity.

For this reason, the A&Mv1 and A&Mv2 models attempt to restrict the generation of recycled stock by enforcing constraints (22) and (28), thereby limiting the number of reusable leftovers. From a managerial standpoint, this consideration can be highly relevant; however, it also entails

the generation of a larger amount of residual material classified as waste, as discussed in the previous section.

In this section, we therefore examine the results from the perspective of inventory heterogeneity by comparing the models in terms of the number of stock bars affected (used) during the cutting process.

Figure 3 clearly shows that, in order to achieve exceptionally low levels of waste, the MACROPT-1D and T&G models require the involvement of a larger number of stock bars.

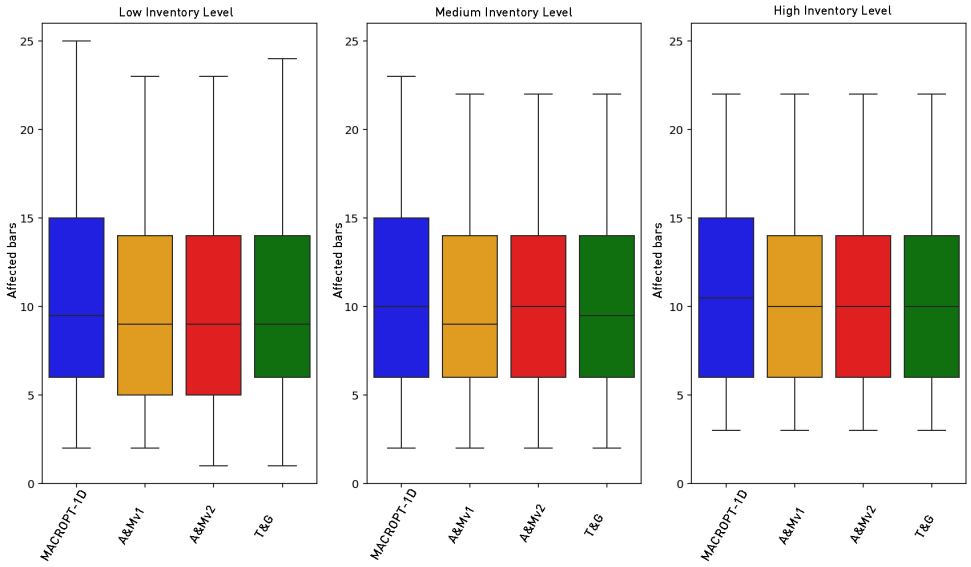

Figure 3. Comparison of the bars affected across models

3.5. Comparison of total cost

Using the cost coefficients introduced in Section 3.1, we compare the total cost of the cutting problems, which includes the cost of cuts, penalties for waste, and the impact on stock bars. Since each model focuses on a different objective, the total cost calculated using these general random cost coefficients may yield a different ranking. Therefore, this comparison is provided here solely to complete the analysis and should not be considered a definitive basis for model evaluation.

Figure 4 contains the boxplots of total cost in the three stock levels.

3.6. Comparison of runtime

An exponential function of the form $T(x) = a \cdot e^{bx}$ was fitted to the measured runtimes, and the resulting approximations are shown in Figure 5. For all models, an exponentially increasing trend is observed with respect to the number of orders. The three scenarios illustrate how inventory levels affect the rate of this increase. In general, it can be stated that beyond a certain critical number of orders, the runtimes of the models diverge, with A&Mv1 exhibiting the highest computational demand and the T&G model being the least resource-intensive.

4. Theoretical inaccuracy of the A&Mv2 model and a necessary correction

In this section we present a theoretical inaccuracy of the A&Mv2 model and propose a correction.

Authors of [14] state that for the A&Mv2 model, YRT_j indicates if the slackness Rl_j of a used object j is a leftover, i.e., if $Rl_j \geq W (YRT_j = 1)$

$$YRT_j = \begin{cases} 1 & \text{if bar } j \text{ was used AND the leftover } Rl_j \geq W \\ 0 & \text{if the bar was not used OR the leftover } Rl_j < W \end{cases}$$

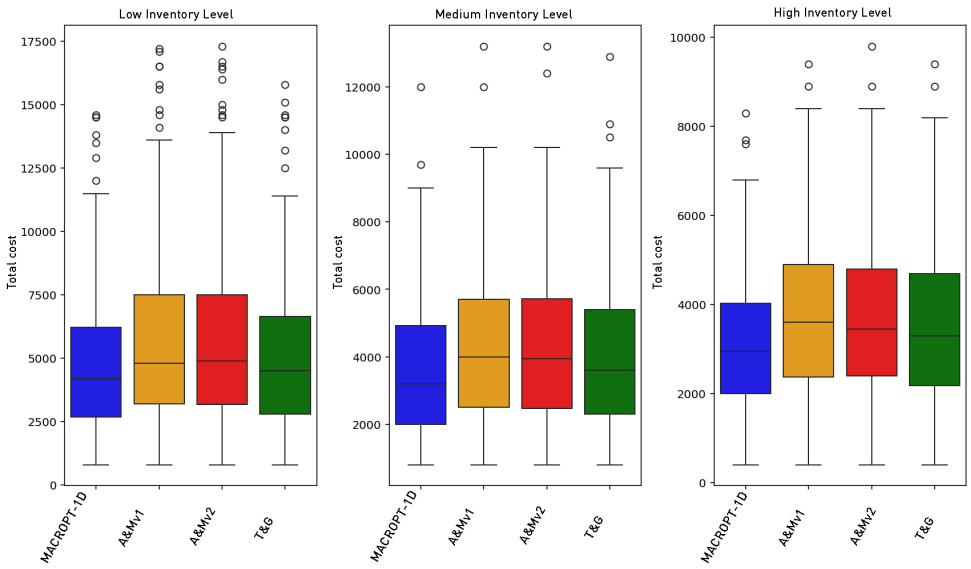

Figure 4. Comparison of total cost across models

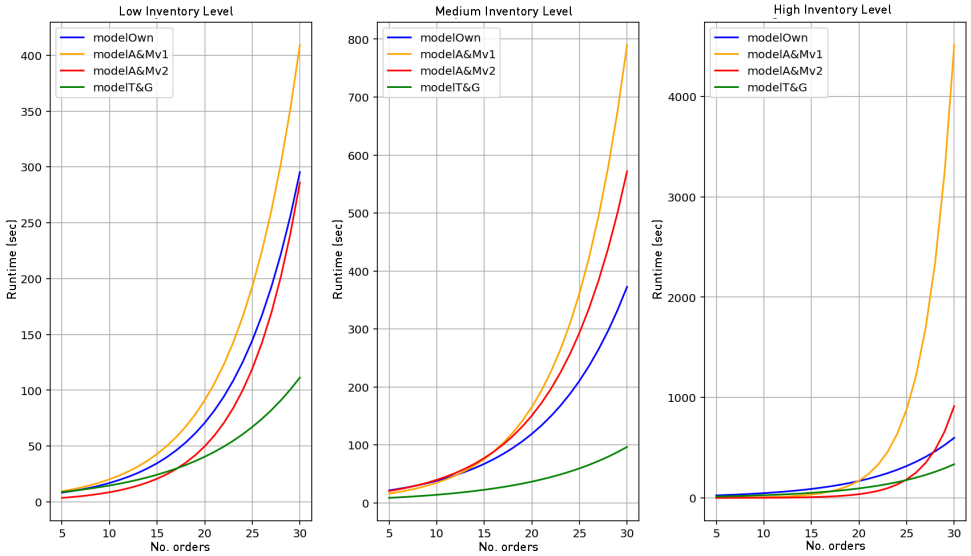

Figure 5. Comparison of runtime

Let us suppose we have an optimal solution in which all bars except j_0 were not returned to the stock, i.e.

$$\sum_{j=1|j\neq j_0}^{m} YRT_j = 0$$

and moreover, none of the orders was assigned to the bar j_0.

$$\sum_{i=1}^{n} x_{ij_0} = 0.$$

Denote the optimal value of the other variables by
$Wl^* = (Wl_1^*, Wl_2^*, \ldots, Wl_m^*)$,
$YU^* = (YU_1^*, YU_2^*, \ldots, YU_{j_0-1}^*, YU_{j_0+1}^*, \ldots, YU_m^*)$,
$YRT^* = (YRT_1^*, YRT_2^*, \ldots, YRT_{j_0-1}^*, YRT_{j_0+1}^*, \ldots, YRT_m^*)$.
In this case both of the values $YU_j = 0; YRT_j = 0$ and $YU_j = 1; YRT_j = 1$ are feasible and also optimal solutions for model (23) - (28)

Case $YU_{j_0} = 0; YRT_{j_0} = 0$

As bar j_0 has no orders assigned to it, $\sum_{i=1}^{n} x_{ij_0} ol_i = 0$. Constraints (26) and (27), that contain those variables are satisfied so

$$W \cdot 0 \ \leq \ bl_j \cdot 0 - 0 \ \leq \ Wl^*_{j_0} + 0 \cdot M.$$

Case $YU_{j_0} = 1; YRT_{j_0} = 1$

Beside the previous case, values $YU_{j_0} = 1; YRT_{j_0} = 1$ are also possible and satisfy the affected constraints, so

$$W \cdot 1 \ \leq \ bl_j \cdot 1 - 0 \ \leq \ Wl^*_{j_0} + 1 \cdot M.$$

Because the value of YU_{j_0} and YRT_{j_0} do not influence the objective value, this means both are optimal solutions.

This may be misleading information, as the new variable incorrectly indicates that the given bar is returned to inventory during the operation, even though it was not used at all to fulfill the orders. In other words it is possible YU_{j_0} and YRT_{j_0} to be 1 even though bar j_0 is not used, i.e. does not have any orders assigned to it $\sum_{i=1}^{n} x_{ij_0} ol_i = 0$.

An appropriate correction could be the following change of constraint (24) :

$$\sum_{i=1}^{n} x_{ij} ol_i + Wl_j = bl_j \cdot YU_j \qquad j = 1, 2, \ldots, m$$

So, this constraint and the objective (23) together will force variables YU_{j_0} and YRT_{j_0} in case of an unused bar j_0 to be 0, correctly.

Instead of changing the constraint (24) another possible way for correction is to introduce the following two restrictions:

$$\sum_{i=1}^{n} x_{ij} \geq YU_j \qquad\qquad j = 1, 2, \ldots, m$$

$$\sum_{i=1}^{n} x_{ij} \geq YRT_j \qquad\qquad j = 1, 2, \ldots, m$$

These constraints force the binary variables YU_j and YRT_j to be zeros if the bar j has no orders assigned to it, so it is not used neither returned to stock.

5. Summary

This paper addresses multi-objective one-dimensional cutting stock problems, with the aim of improving the efficiency of industrial resource utilization while reducing operational costs and material waste. The primary objective is the implementation and extensive simulation-based evaluation of a previously developed multi-objective cutting optimization model and three other models. MACROPT-1D is compared against three models published in the literature: two variants of the model introduced by Abuabara and Morabito [14], and the model proposed by Trkman and Gradisar [15].

All models were implemented in Python using the academic version of Gurobi Optimizer.

With respect to the first research objective outlined in Section 1.1, the comparative analysis is based on both a numerical example and a large-scale simulation study comprising 900 randomly generated test instances, structured into nine scenario groups along two independent dimensions: three inventory levels (low, medium, high) and three order-size scenarios.

Regarding the second objective, model performance was cross-evaluated with respect to five criteria simultaneously: the number of cuts generated, the amount of waste produced, the number of stock bars used, total cost (including cutting and waste penalties), and computational runtime, irrespective of which of these criteria forms part of a model's own native objective. This

cross-evaluation revealed trade-offs that would have remained hidden under a single-criterion assessment. Most notably, the waste-only models of Abuabara and Morabito [14] were found to generate *more* waste, on average, than the multi-objective MACROPT-1D and T&G models, a consequence of the side constraint limiting the number of recycled remainders, which is intended to prevent inventory explosion but inadvertently penalizes waste minimization itself.

Concerning the third objective, the results show that the proposed multi-objective model MACROPT-1D, which simultaneously minimizes the number of cuts, waste, and the number of used stock bars, achieves superior performance in reducing the number of cuts and total cost, and in many cases also outperforms waste-focused models in waste minimization. This improved performance comes at the expense of increased raw material usage, as the proposed model tends to utilize a larger number of stock bars. In terms of computational efficiency, the T&G model proved to be the fastest, while the proposed model exhibited moderate running times.

Finally, with respect to the fourth objective, the theoretical correctness analysis identified an inconsistency in the A&Mv2 model. Simulation results revealed that in approximately 1.33% of the cases, the model may incorrectly classify a stock bar as both used and returned to inventory, despite no order being assigned to it. To address this issue, two additional linear constraints or an appropriate change of the original length balance constraint are proposed, restoring logical consistency and yielding correct results in subsequent tests.

5.1. Future research directions

The findings of this study suggest several promising directions for future work. First, the comparison presented here relies on a fixed set of cost coefficients and a single, weighted-sum scalarization of the competing objectives; an explicit Pareto-based analysis, using scalarization techniques such as the ε-constraint or Chebyshev methods, would allow the trade-offs between the number of cuts, waste, and the number of affected bars to be characterized more comprehensively than a single linear combination of weights permits.

Second, the runtime analysis in Section 3.6 indicates that all four exact MILP formulations face rapidly increasing computational demands as the number of orders grows; extending MACROPT-1D with a matheuristic or heuristic solution approach, in the spirit of recent column-generation- and local-branching-based methods for related cutting stock variants [12], could substantially improve scalability to industrial-size instances without sacrificing the model's multi-objective structure. Third, the present model and its competitors are formulated for a single planning period with deterministic order lengths and quantities; incorporating multiple planning periods or demand uncertainty, following recent developments in the broader cutting stock literature [7], would bring the model closer to real industrial practice, where orders typically arrive over time and are subject to variability. Fourth, extending the present one-dimensional framework to a two-dimensional setting, analogous to recent multi-objective formulations for sheet and plate cutting [9], would broaden the applicability of the proposed adjustable, parametric objective beyond bar-cutting industries.

Finally, validating MACROPT-1D on real industrial datasets, following the practice of recent applied studies, such as BIM-based rebar cutting optimization in construction [4], rather than relying solely on randomly generated instances, would provide further evidence of its practical applicability and help quantify the managerial trade-off between waste reduction and inventory heterogeneity observed in this study.

Acknowledgments

None.

Funding

None.

Conflict of interest

There is no conflict of interest to disclose.

Author contributions

Anett Rácz: Conceptualization, Methodology, Supervision, Writing – original draft, Writing – review & editing.
Ákos Szabó: Software, Visualization, Writing – original draft, Writing – review & editing.

Declaration of using AI tools

The authors declare that they have not used any type of generative artificial intelligence for the conceptual writing of this manuscript, nor for the creation of images, graphics, tables, or their corresponding captions. AI tools were solely used to identify relevant recent literature for the literature review and for basic linguistic corrections. All AI-suggested sources were independently verified by the authors before being cited.

References

[1] A.A. Shahin and O.M. Salem. "Using genetic algorithms in solving the one-dimensional cutting stock problem in the construction industry." *Canadian Journal of Civil Engineering*, vol. 31, no. 2, 2004, pp. 321-332. https://doi.org/10.1139/l03-101

[2] D. Tanır, O. Ugurlu, A. Guler and U. Nuriyev. "One-dimensional cutting stock problem with divisible items: A case study in steel industry." *TWMS Journal of Applied and Engineering Mathematics*, vol. 9, no. 3, 2019, pp. 473-484.

[3] G.A. Ogunranti and A.E. Oluleye. "Minimizing waste (off-cuts) using cutting stock model: The case of one dimensional cutting stock problem in wood working industry." *Journal of Industrial Engineering and Management (JIEM)*, vol. 9, no. 3, 2016, pp. 834-859. https://doi.org/10.3926/jiem.1653

[4] Z. Wang, et al. "Minimization of rebar cutting waste using BIM and cutting pattern-oriented multiobjective optimization." *Journal of Construction Engineering and Management*, vol. 150, no. 11, 2024, 04024166. https://doi.org/10.1061/JCEMD4.COENG-15104

[5] B.S.C. Campello, et al. "A multiobjective integrated model for lot sizing and cutting stock problems." *Journal of the Operational Research Society*, vol. 71, no. 9, 2020, pp. 1466-1478. https://doi.org/10.1080/01605682.2019.1619892

[6] G.G. Guimarães, K.C. Poldi and M. Martin. "Mathematical models for the one-dimensional cutting stock problem with setups and open stacks." *Journal of Combinatorial Optimization*, vol. 49, no. 3, 2025, pp. 43. https://doi.org/10.1007/s10878-025-01276-5

[7] V. Senergues, N. Brahimi, A.C. Cherri, F. Klein and O. Péton. "Cutting stock problem with usable leftovers: A review." *European Journal of Operational Research*, vol. 328, no. 1, 2026, pp. 1-14. https://doi.org/10.1016/j.ejor.2025.03.014

[8] A.C. Cherri, M.N. Arenales, H.H. Yanasse, K.C. Poldi and A.C.G. Vianna. "The one-dimensional cutting stock problem with usable leftovers-A survey." *European Journal of Operational Research*, vol. 236, no. 2, 2014, pp. 395-402. https://doi.org/10.1016/j.ejor.2013.11.026

[9] Y. Ma, J. Zhang, X. Yang, J. Li, X. Su and H. Chen. "Two-dimensional cutting stock problem with flexible length and usable leftovers in the steel industry." *European Journal of Operational Research*, vol. 326, no. 2, 2025, pp. 207-219. https://doi.org/10.1016/j.ejor.2025.04.036

[10] L.J. Montiel-Arrieta, et al. "Minimizing the total waste in the one-dimensional cutting stock problem with the African buffalo optimization algorithm." *PeerJ Computer Science*, 9, 2023, e1728. https://doi.org/10.7717/peerj-cs.1728

[11] G.M. Bressan, M.H. Pimenta-Zanon and F. Sakuray. "A tree-based heuristic for the one-dimensional cutting stock problem optimization using leftovers." *Materials*, vol. 16, no. 22, 2023, 7133. https://doi.org/10.3390/ma16227133

[12] E. de Araújo Silva Oliveira, et al. "A local branching-based solution for the multi-period cutting stock problem with tardiness, earliness, and setup costs." *Journal of Heuristics*, vol. 31, no. 1, 2025, 16. https://doi.org/10.1007/s10732-025-09547-4

[13] A. Rácz. "A MILP model for one dimensional cutting stock problem with adjustable leftover threshold and cutting cost." *An International Journal of Optimization and Control: Theories & Applications*, vol. 15, no. 2, 2025, pp. 215-224. https://doi.org/10.36922/ijocta.1660

[14] A. Abuabara and R. Morabito. "Cutting optimization of structural tubes to build agricultural light aircrafts." *Annals of Operations Research*, vol. 169, no. 1, 2009, pp. 149-165. https://doi.org/10.1007/s10479-008-0438-7

[15] P. Trkman and M. Gradisar. "One-dimensional cutting stock optimization in consecutive time periods." *European Journal of Operational Research*, vol. 179, no. 2, 2007, pp. 291-301. https://doi.org/10.1016/j.ejor.2006.03.027

All open access articles published in Transactions on Computational Modeling and Intelligent Systems (http://tcmis.org) are distributed under the terms of the CC BY-NC 4.0 license (Creative Commons Attribution Non-Commercial 4.0 International Public License as currently displayed at http://creativecommons.org/licenses/by-nc/4.0/legalcode) which permits unrestricted use, distribution, and reproduction in any medium, for non-commercial purposes, provided the original work is properly cited.

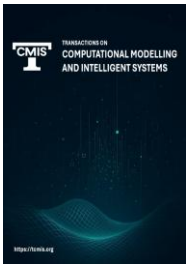

Transactions on
Computational Modeling and Intelligent Systems

Volume 4, July 2026, Article 10078
https://doi.org/10.65112/tcmis.10078

eISSN: 3108-5202
www.tcmis.org

RESEARCH ARTICLE

Conformable sliding mode control and analysis of Lorenz chaotic system

Haris Calgan[1,2*], Metin Demirtas[1]

[1]*Department of Electrical and Electronics Engineering, University of Balikesir, Balikesir, Türkiye.*
[2]*Mechatronics Research Group, Faculty of Engineering and Physical Science, University of Southampton, Southampton, SO171BJ, United Kingdom.*

[*]*Corresponding Author. Email: haris.calgan@balikesir.edu.tr (H. Calgan)*

Article Information

Received: 23 March 2026
Accepted: 16 June 2026
Published: 11 July 2026

AMS 2020 Classification: 26A33, 34H10

Abstract

This study comparatively and innovatively examines linear state feedback control (LSFC) of the Conformable Sliding Mode Control (CSMC) methods on the conformable fractional-order Lorenz system. The extreme sensitivity of chaotic systems to initial conditions and their nonlinear nature present significant challenges for classical control methods. In this context, the conformable fractional derivative approach integrates the memory effect and fractional order character of the system into the model by adding a t^{q-1} multiplier to the system dynamics, while preserving the classical differential form. Thus, both analytical simplification is achieved and the physical interpretation of fractional dynamics is preserved. One of the original contributions of the study is the investigation of the conformable fractional-order form of the Lorenz system under control and the systematic comparison of two different control strategies under the same performance criteria. Innovatively, the effect of the conformable fractional-order on control performance is parametrically analysed, and the decisive role of the fractional order (q) on system stability and convergence speed is revealed. By activating the control signals after a specific delay, the natural evolution of the system in a chaotic regime was observed, and a realistic suppression scenario was created. This approach offers a more practical engineering perspective compared to instantaneous control applications. The results showed that the LSFC method provides a simple control structure and smooth control action. In contrast, the CSMC method achieves shorter settling time, faster convergence, improved disturbance rejection capability, and higher robustness against external disturbances and parameter uncertainties.

Keywords: Conformable, fractional, sliding mode, Lorenz, chaotic system

1. Introduction

The concept of conformable fractional-order derivatives has been developed as an alternative to classical fractional derivative definitions (such as Riemann–Liouville and Caputo) and has become a noteworthy approach in recent years, particularly in the field of control systems. Defined by reference, the conformable derivative largely preserves the classical structure of the differential operator while imparting fractional-order behaviour to the system via a t^{q-1} multiplier. This feature simplifies analytical operations and makes it possible to integrate the memory effect of fractional systems into control design [1].

Conformable fractional calculus has been extensively investigated from both theoretical and numerical perspectives. New mathematical properties of conformable fractional derivatives have been reported in the literature, further strengthening their analytical foundation [2], [3]. Moreover, conformable finite-element formulations have been developed for fractional partial differential equations, demonstrating the applicability of the conformable framework to large-scale engineering problems [4]. Recent studies have also addressed the stability analysis of conformable infinite-dimensional systems [5], semilinear systems [6] and conformable Θ-H systems [7], highlighting the growing importance of conformable fractional calculus in modern control theory and dynamical systems analysis.

Although not directly classified by this name in traditional control literature, conformable fractional differential systems are addressed within the scope of controllability and model-based feedback design. In this context, Wang and Fečkan provided a theoretical basis for model-based control design by examining the controllability conditions of conformable differential systems [8]. Similarly, Ding et al. investigated conformable impulsive differential equations by establishing solution representations and analyzing asymptotic as well as generalized Ulam–Hyers–Rassias stability [9]. Furthermore, Sadek contributed to model-based control approaches by examining the stability and observability conditions in conformable linear dynamic systems [10]. In linear state feedback control, the main goal is to cancel out nonlinear terms through feedback and transform the fault dynamics into a stable structure under the assumption that the system dynamics are known. Lyapunov-based analyses are generally used in such studies, and the effect of the fractional degree parameter (q) on system performance is examined [8]. Current research shows that the fractional degree can be used not only as a mathematical extension but also as an adjustable design parameter on control energy and settling time. CSMC has a more application-oriented and broader scope in the literature. Its robust structure and high performance under parameter uncertainties and external disturbances have led to its adaptation to conformable fractional systems. Alfi demonstrated the stability of conformable fractional chaotic systems by designing a sliding mode control system using the Lyapunov approach [11]. This work is significant because it shows how a conformable derivative operator can be used in sliding surface design. Conformable versions of terminal sliding mode control are also found in the literature. Haghighatnia designed a conformable fractional terminal sliding mode controller for uncertain nonlinear systems and analysed its finite-time convergence property [12]. Furthermore, Muñoz-Vázquez et al. proposed a generalized conformable sliding mode control approach, redefining the classical sliding surface with a conformable derivative structure and presenting their stability analyses in detail [13]. When these studies are evaluated, it is seen that conformable sliding mode control is extensively investigated, especially in the suppression of chaotic systems, stabilization of uncertain nonlinear systems, and finite-time control problems [11], [12]. The fractional-order parameter can affect both the convergence speed and the robustness level by shaping the dynamics of the sliding surface [13].

In this paper, the authors propose an approach that simplifies this task by creating novel sufficient conditions that allow the Lyapunov function candidate to increase in certain regions when traditional Lyapunov-based stability analysis is not feasible. The study examines equilibrium point stability, asymptotic stability, and global asymptotic stability [14]. Generally, the literature shows that conformable traditional control stands out with its model accuracy and low energy consumption, while conformable sliding mode control provides high robustness, fast convergence, and resilience to uncertainties [15]; the fractional order parameter is used as a decisive design parameter in both methods, influencing the behaviour of the control signal and system stability. A review of the literature reveals that studies on conformable linear state feedback control are more focused on theoretical controllability and model-based design, while studies on conformable sliding mode control are more intensively addressed with a focus on application and robustness. The linear state feedback control approach generally stands out with its simple implementation and smooth control signal generation, while conformable sliding mode control provides faster convergence and resilience to parameter uncertainties. Current studies demonstrate that the fractional order can be used as an important design parameter in both methods.

2. Mathematical modelling and formulation

2.1 Sliding mode control

SMC is a widely used method for controlling nonlinear systems due to its high robustness against uncertainties and external disturbances. The classical SMC approach aims to achieve asymptotic stability by orienting and holding system states on a predefined sliding surface. The main advantage of this method is that when the sliding mode is reached, the system dynamics become independent of parameter uncertainties and coupled disturbances. The fundamental principles of SMC were first systematically formulated by Vadim Utkin [16]. In sliding mode control, a sliding surface is primarily defined. System states hit this sliding surface, causing them to return to the origin. In this state, the system becomes stable. Sliding mode control consists of two phases reaching and sliding phases. In classical sliding mode control, high-frequency oscillations (chattering) occur on the sliding surface. In the control of dynamic systems such as electric motors, this chattering causes the motor to run erratically or jerkily, thus damaging the device. To eliminate this harmful effect, a bounded layer is created around the sliding surface. In the literature, functions such as fuzzy logic, tanh, and saturation are used for this purpose [17]. In this study, the saturation function was used instead of the signum function used in classical sliding mode structure as shown in Figure 1. Sliding mode control design consists of two phases: sliding surface design and controller design. The sliding condition forces the system states to reach the sliding surface (reaching phase) and sends them back to the origin via the surface, holding them at the equilibrium point.

In the article, the authors propose a novel piecewise continuous system by introducing a threshold level for states in Lorenz and Rabinovich systems. They used sliding mode control to achieve adaptive synchronization between switched dynamic systems with unknown parameters [18]. This article presents the design of an adaptive terminal sliding mode controller for dynamic systems. The proposed sliding surface has finite-time convergence capability. The gains of the access law are adjusted as a function of the sliding surface. The control law has been applied to

quad copter unmanned aerial vehicles, and it has been observed that the controller is robust against external disturbances and parametric uncertainties [19].

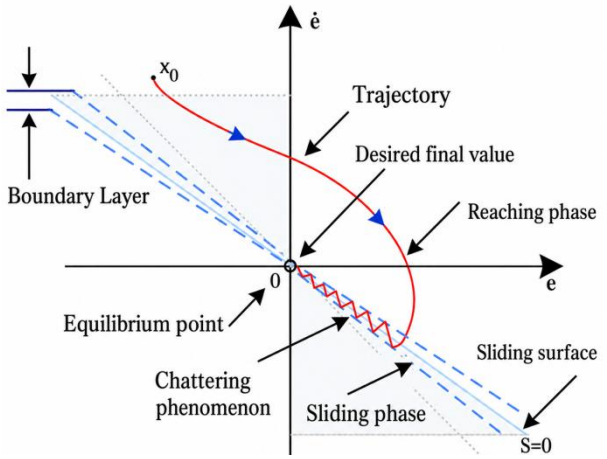

Figure 1. Sliding mode structure

2.2 Lorenz system equations

The Lorenz system is a system of nonlinear differential equations developed by Edward Lorenz in 1963 to simplify the model of atmospheric convection [20]. It played a fundamental role in the birth of chaos theory and demonstrated the possibility of unpredictable behaviour in deterministic systems. The system consists of three related nonlinear differential equations as below [20]:

$$\begin{aligned} \dot{x}_1 &= \sigma(x_2 - x_1) \\ \dot{x}_2 &= x_1(\rho - x_3) - x_2 \\ \dot{x}_3 &= x_1 x_2 - \beta x_3 \end{aligned} \tag{1}$$

When system parameters set to $\sigma = 10$, $\rho = 28$, $\beta = 8/3$, Lorenz system produces chaotic flows. On the other hand, the conformable fractional-order Lorenz system is a generalization of the classical Lorenz system using the concept of fractional derivatives. The classical Lorenz system, developed by Edward Lorenz in 1963 to model atmospheric convection movements, is one of the best-known examples of chaotic behaviour. The system consists of three nonlinear differential equations and produces chaotic (irregular but deterministic) solutions at certain parameter values. In fractional order systems, the derivative order does not have to be an integer (such as 1, 2, 3); it can be a fractional value such as $0 < q \leq 1$ [21]. A conformable derivative is a definition of a fractional derivative that possesses properties similar to the classical derivative (linearity, multiplication rule, etc.) and is easier to analyse. Therefore, it is frequently preferred in engineering and physics problems. In conformable fractional derivatives, *q*-order conformable derivatives are used instead of first-order time derivatives in Lorenz equations.

For a differentiable function, the conformable fractional derivative compatible with order is defined as follows [12]:

$$T^q x(t) = t^{1-q} \frac{dx(t)}{dt}, 0 < q \leq 1 \tag{2}$$

Using the conformable derivative definition $T^q x(t) = t^{1-q} \frac{dx(t)}{dt}$, the ordinary derivative can be expressed as $\frac{dx(t)}{dt} = t^{q-1} T^q x(t)$. Therefore, a conformable fractional-order system of the form $T^q x = f(x)$ can be equivalently rewritten as $\dot{x} = t^{q-1} f(x)$. This equivalent representation enables the conformable system to be simulated using conventional ODE solvers while preserving the influence of the conformable fractional-order parameter (q). Using this formulation, the classical Lorenz system given in Eq. (2) can be rewritten as [20]:

$$\begin{aligned} T^q x_1 &= \sigma(x_2 - x_1) \\ T^q x_2 &= x_1(\rho - x_3) - x_2 \\ T^q x_3 &= x_1 x_2 - \beta x_3 \end{aligned} \tag{3}$$

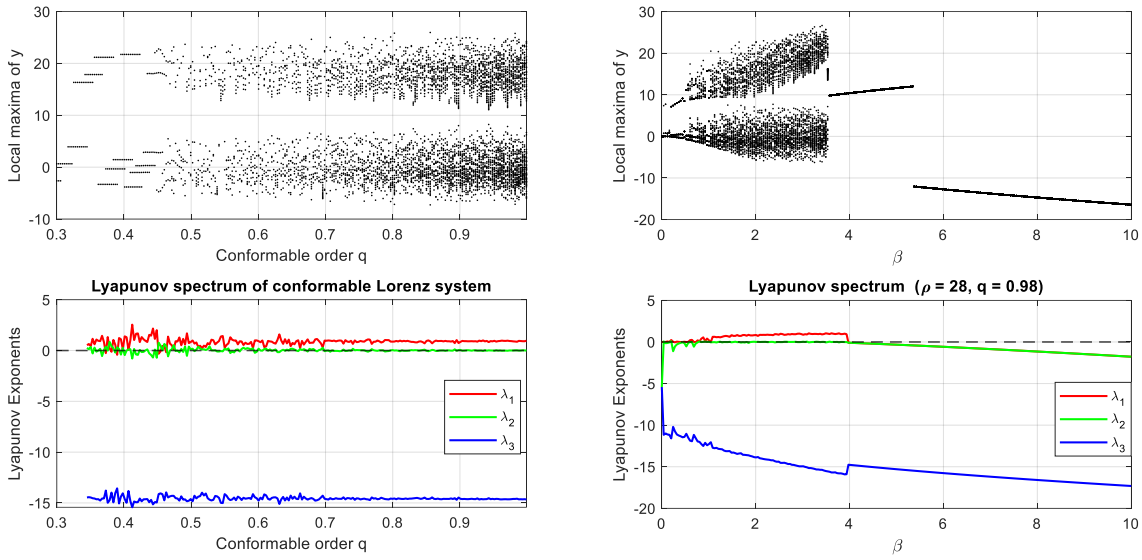

(a) (b)

Figure 2. Bifurcation diagram and Lyapunov spectrum of conformable fractional-order Lorenz chaotic system (a) $\sigma = 10$, $\rho = 28$ and $\beta = 8/3$, (b) $\sigma = 10$, $\rho = 28$ and $q = 0.98$.

To investigate the influence of the conformable fractional-order parameter on the system dynamics, bifurcation diagrams and Lyapunov exponent spectra were generated with respect to both q and β, as shown in Figure 2. Figure 2(a) demonstrates that the system exhibits a transition from periodic to chaotic behavior as the conformable order q increases. The corresponding Lyapunov spectrum confirms this observation, where the largest Lyapunov exponent becomes positive for $q \geq 0.4$, indicating the onset of chaos. Moreover, the chaotic regime persists over a wide range of q values, including the selected operating point q=0.98. Figure 2(b) presents the bifurcation and Lyapunov analyses with respect to the parameter β while keeping q=0.98. It can be observed that the system maintains chaotic dynamics for (0< β <4), where the largest Lyapunov exponent remains positive. These results verify that the chosen parameter set $\sigma = 10$, $\rho = 28$, $q = 0.98$ lies within a well-developed chaotic region and is therefore suitable for the subsequent control studies. For given parameters values, the system exhibits chaotic behaviour.

2.1. Control law design

Feedback linearization-based state feedback control is employed as a benchmark controller in this study. The control law given in Eq. (4) is designed to cancel the nonlinear dynamics of the Lorenz system and impose stable linear closed-loop dynamics.

$$u(t) = -f(x) - Kx \tag{4}$$

where K>0 is the feedback gain matrix. The conformable Lorenz system is represented as

$$\dot{x} = t^{q-1}\left(f(x) + Bu\right) \tag{5}$$

where $B = \begin{bmatrix} 1 & 0 & 0 \end{bmatrix}^T$ is the input distribution vector, indicating that the control signal is applied through the first state equation. Substituting Eq. (4) into the system dynamics yields:

$$\begin{aligned} \dot{x} &= t^{q-1}\left(f(x) - f(x) - Kx\right) \\ \dot{x} &= t^{q-1}(-Kx) \end{aligned} \tag{6}$$

Therefore, the nonlinear dynamics are cancelled and the resulting closed-loop system behaves as a conformable linear state-feedback system. As the control input is applied through the first state equation, the controller directly regulates the x_1 state, while the x_2 and x_3 states are influenced indirectly through the inherent coupling of the Lorenz dynamics.

Fractional-order systems produce more realistic results in many physical and engineering systems due to their ability to model memory and hereditary properties compared to classical integer-order models. In this context, the

conformable derivative, which is among the fractional derivative definitions, offers significant advantages in control design because it both preserves the local structure and has chain rule and linearity properties similar to the classical derivative.

CSMC is achieved by adapting the classical SMC structure to conformable fractional-order systems. In this approach, system dynamics are modelled using a conformable derivative operator, and the sliding surface is usually defined as a linear combination:

$$s = cx \tag{7}$$

Error vector of system can be written as below:

$$e(t) = x(t) - x_{ref} \tag{8}$$

Since the goal is for the states to go directly to zero, the x_{ref} value is taken as zero. In this case, the error is written as follows.

$$e_1(t) = x_1(t), \quad e_2(t) = x_2(t), \quad e_3(t) = x_3(t) \tag{9}$$

c is a suitably chosen constant coefficient vector in sliding mode. The aim is to arrange the conformable derivative of the sliding variable such that it is negative definite. In this respect, a typical reaching law can be defined as follows:

$$c(f(x) + Bu) = -ks - \eta sat(s/\phi) \tag{10}$$

Here, k>0 represents the control gain, boundary layer thickness parameter is ϕ and $sat(\cdot)$ represents the saturation function. Increasing ϕ enlarges the boundary layer around the sliding surface, which reduces switching activity and mitigates the chattering phenomenon. However, an excessively large ϕ may decrease tracking accuracy and increase the steady-state error [22]. Using the saturation function reduces the chattering effect compared to the classical sign function. If the control signal 'u' in the equation is left alone:

$$u = -\frac{cf(x) + ks + \eta sat(s/\phi)}{cB} \tag{11}$$

Since the system is single-input, the input distribution vector is selected as $B = \begin{bmatrix} 1 & 0 & 0 \end{bmatrix}^T$ which results in $cB = 1$. The derivative of sliding surface can be written as below:

$$\dot{s} = c\dot{x} = t^{q-1}(-ks - \eta sat(s/\phi) \tag{12}$$

To verify the stability of the proposed conformable sliding mode controller, consider the Lyapunov candidate function

$$V(s) = \frac{1}{2}s^2 \tag{13}$$

Taking the time derivative yields dot $V = s\dot{s}$. Substituting Eq. (12) gives

$$\dot{V} = s, t^{q-1}\left(-ks - \eta, sat\left(\frac{s}{\phi}\right)\right) \tag{14}$$

Thus,

$$-t^{q-1}\left(ks^2 + \eta, s, sat\left(\frac{s}{\phi}\right)\right) \tag{15}$$

Since ($0<q\leq 1$), it follows that ($t^{q-1}>0$) for (t>0). Moreover, $[s, sat\left(\frac{s}{\phi}\right) \geq 0.]$ and $\dot{V} \leq -t^{q-1}ks^2 \leq 0.$ Hence, $V(s)$ is a non-increasing function and the sliding variable converges toward the sliding surface. Consequently, the proposed conformable sliding mode control law guarantees asymptotic stability of the closed-loop system.

The control applies pressure not only to x_1 but also to x_2 and x_3 via the combination selected with c, forcing them onto the sliding surface simultaneously (c=[1 0.8 0.5]). Depending on the sliding surface c values, it can be written as follows:

$$s = x_1 + 0.8x_2 + 0.5x_3 \tag{16}$$

In both methods, the conformable part is used in the same location.

$$\dot{x} = t^{q-1}(...) \tag{17}$$

The most important advantage of SMC in the conformable framework is that it offers lower computational complexity compared to classical fractional derivative definitions (e.g., Riemann–Liouville or Caputo) and can be easily integrated with standard numerical solution methods thanks to its time-scaling structure. Therefore, it stands out as an effective and practical method for stabilizing chaotic systems.

Especially in strongly nonlinear and conditionally sensitive systems like the Lorenz System, CSMC enables the systematic convergence of the sliding variable to zero, allowing all state variables to be guided to a stable equilibrium point in a coordinated manner. Furthermore, its invariance against coupled disturbances allows for faster convergence and higher robustness performance compared to traditional control methods.

The superior disturbance rejection capability of the proposed CSMC method can be explained by the structure of the sliding surface. In the LSFC approach, the control input is applied through a single channel and directly regulates only the x_1 state, while the x_2 and x_3 states are influenced indirectly through the inherent coupling of the Lorenz dynamics. Consequently, disturbances acting on the system may propagate through the uncontrolled states and lead to larger oscillations. In contrast, the proposed CSMC method employs a sliding surface of the form $s = cx$, where all state variables participate simultaneously in the control objective. Therefore, deviations in any state variable contribute to the sliding variable and are actively compensated by the controller. This coordinated state regulation improves disturbance attenuation, accelerates convergence, and enhances the overall robustness of the closed-loop system.

3. Simulation studies

In this study, the Lorenz chaotic system was mathematically modeled using the conformable derivative definition, and the system's control performance was analyzed through numerical simulations performed in MATLAB. The system equations were coded in MATLAB, and both the LSFC method and the proposed CSMC method were applied comparatively under the same initial conditions and disturbance scenarios. In the simulations, the robustness performance of the control methods was evaluated by applying the disturbance to the system at a specific time point. The results obtained are presented graphically, and the changes in state variables over time are examined. The coefficient values, are used in the conformable sliding mode controller in the simulation studies were taken as k=6, η=10, ϕ=0,05. Lorenz parameters were taken as $x(0)$=[1,5 -2 3] and and q=0.98. Both controllers become active after 20 seconds. The proposed CSMC operates faster and goes to zero compared to the LSFC.

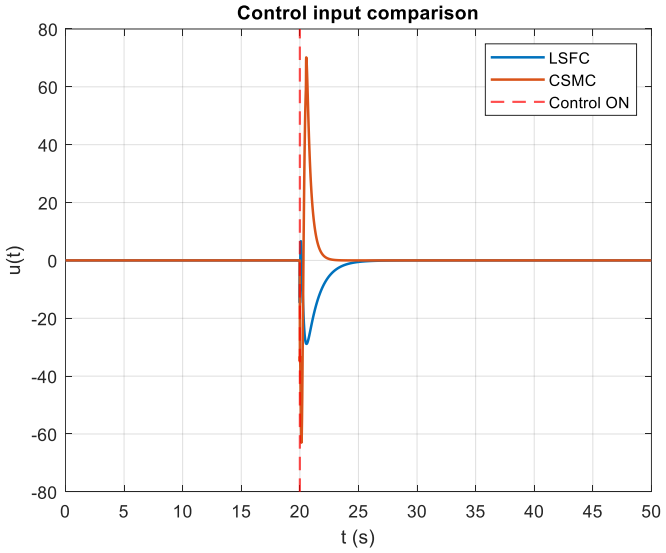

Figure 3. Comparison of LSFC and CSMC control input signals after controller activation.

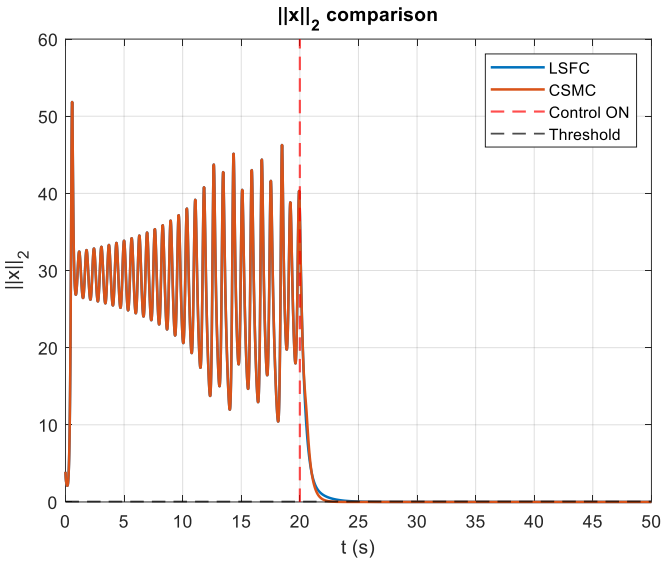

Figure 4. Comparison of the Euclidean norm of the state vector ||x||₂ for the LSFC and CSMC methods when the control action is activated at t=20 s.

Figure 4 shows that the CSMC method drives the state norm to zero significantly faster than the LSFC method. This result demonstrates the superior convergence performance of the proposed controller.

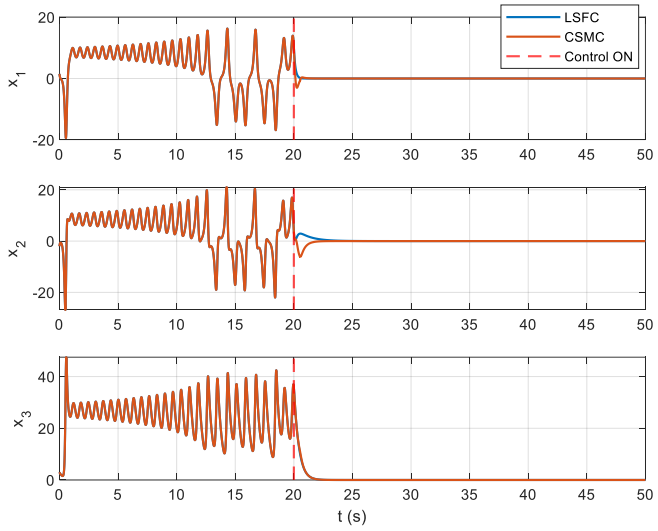

Figure 5. State trajectories of the conformable fractional-order Lorenz system under LSFC and CSMC.

Looking at the state trajectories given in Figure 5, it can be seen that x_1 and x_2 settle at approximately the same time (equilibrium point), while the CSMC settles at zero earlier in x_3.

4. Comparative analysis of two controllers

To measure the system's response to disturbances, a variable signal was added to the circuit after 20 seconds. The mathematical expression for the added complex signal is given below.

$$d(t)=\begin{cases}0, & t<t_{on}\\ 8\sin(4t)+6\cos(2t)+4\sin(0.5t) & t>t_{on}\end{cases} \tag{17}$$

The disturbance signal is activated in 20 seconds along with the controller. The change in the disturbance signal over time is shown in Figure 6. To ensure accurate comparison, the same disturbance was added to both controllers for the same duration.

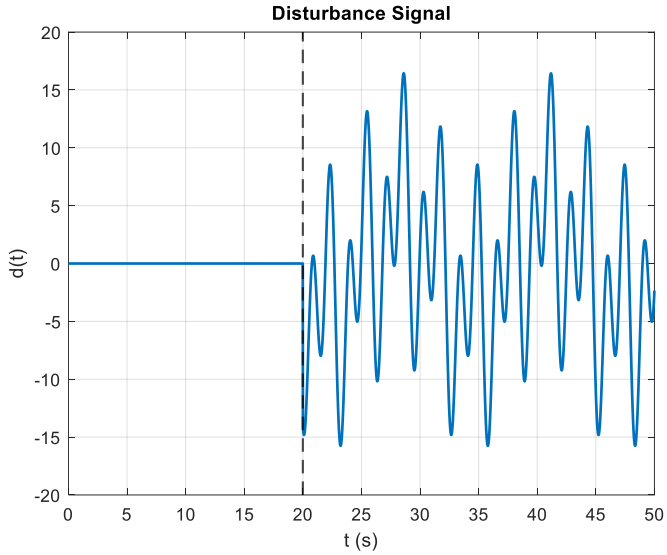

Figure 6. External disturbance signal applied to both controllers after t = 20 s.

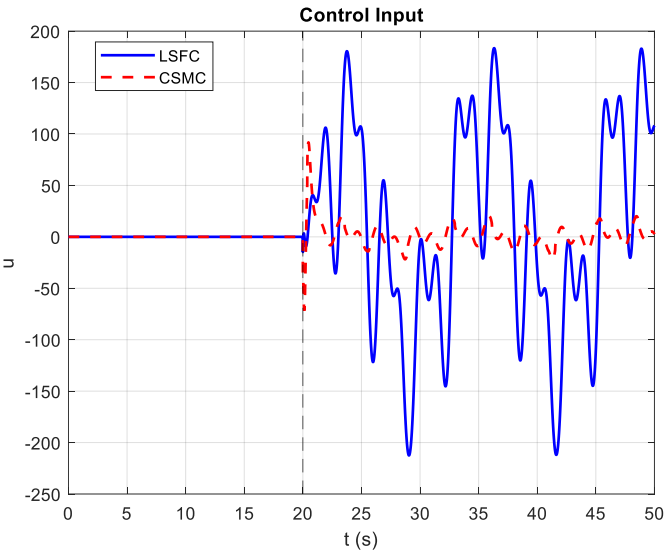

Figure 7. Comparison of LSFC and CSMC control signals under external disturbance conditions. Disturbance and control are activated at t=20 s.

Figure 7 compares the control signals generated by the LSFC and CSMC methods under external disturbance conditions. Before the activation instant ((t<20) s), the control inputs remain zero. After the controllers and disturbance are activated at (t=20) s, both methods generate control actions to suppress the chaotic dynamics. It can be observed that the LSFC method requires significantly larger control effort, resulting in high-amplitude control oscillations. In contrast, the CSMC method produces a more bounded control signal while maintaining effective stabilization performance. These results indicate that the proposed CSMC approach achieves robust disturbance rejection with a lower control amplitude and smoother control behaviour under the considered operating conditions.

Figure 8 compares the Euclidean norm of the state x_1, for the LSFC and CSMC methods under external disturbance conditions. During the first 20 seconds, when no control action is applied, the state norm exhibits oscillatory behaviour due to the chaotic nature of the Lorenz system. After the controllers are activated at (t=20) s, the CSMC method rapidly drives the state norm toward zero and maintains it close to the equilibrium point despite the presence of disturbances. In contrast, the LSFC method reduces the state norm but fails to completely suppress the oscillations, resulting in persistent fluctuations. These results indicate that the proposed CSMC approach provides faster convergence, improved disturbance rejection capability, and enhanced robustness compared with the LSFC method.

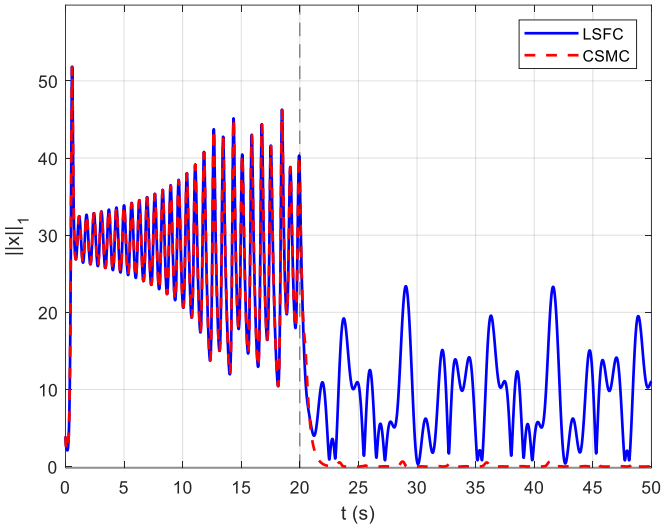

Figure 8. Comparison of the Euclidean norm of the state x_1 under external disturbance for the LSFC and CSMC methods.

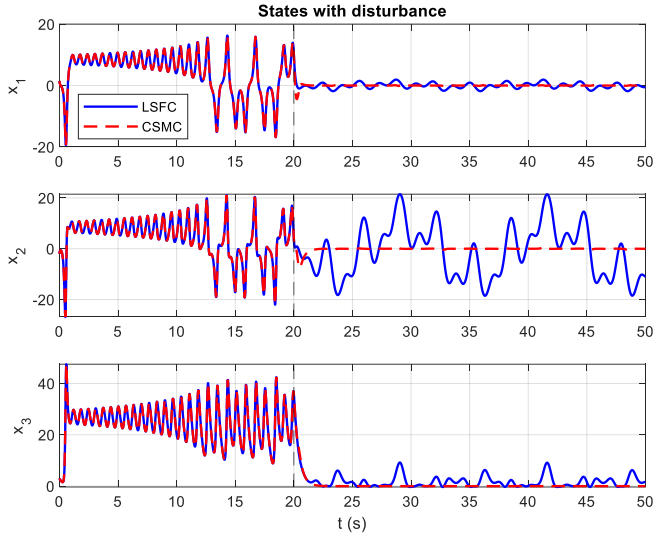

Figure 9. Comparison of state trajectories under external disturbance for LSFC and CSMC methods.

Figure 9 presents the performance of LSFC and CSMC methods for three state variables (x_1, x_2, x_3) of a Lorenz system under external disturbance. Up to approximately 20 seconds after the control is activated, increasing amplitude oscillations originating from the chaotic structure are observed in all state variables. After the disturbance is applied, the LSFC method reduces the oscillation amplitudes but cannot completely suppress the disturbance effects, particularly in the x_2 and x_3 states. In contrast, the CSMC method rapidly attenuates the oscillations and maintains all state variables close to the equilibrium point, demonstrating superior robustness against external disturbances. It is particularly noteworthy that CSMC provides both faster transient regime performance and lower steady-state error. These results demonstrate that the conformable sliding mode control method offers higher stability, stronger external disturbance suppression, and superior robust control performance for all state variables of chaotic systems under external disturbance. When all the results obtained are evaluated together, it is seen that the Conformable Sliding Mode Control method offers much higher robustness, faster convergence, lower oscillation amplitude, and superior stability compared to the LSFC method in controlling nonlinear and chaotic systems such as Lorenz under disturbing effects.

In the LSFC method, the control rule uses only linear feedback. In this approach, only the x_1 state is directly suppressed via a single input channel. x_2 and x_3 are indirectly affected. In the case of a chaotic Lorentz system, when the control is activated, x_1 is rapidly damped, while the deviations of the other states may decrease more slowly. This method does not have a chattering problem, and the control inputs are smooth. However, model accuracy is critical for high performance; the stabilization and accuracy of the system can be seriously affected in the presence of parameter deviations or measurement noise. In conformable sliding mode control, all states are

oriented together across the sliding surface. The control law includes both a linear and a switching term. Thanks to this structure, the surface dynamics work in accordance with the conformable derivative factor, and coordinated damping of all states is ensured. In addition, this control strategy is more robust against parameter uncertainty and external disturbances, i.e., it offers robust control characteristics. Although there is an inherent risk of chattering in the control, these effects can be greatly reduced with the saturation function and boundary layer.

In the literature, SMC in single-input chaotic systems is mostly performed with linearization + classical sliding surface. In this study, stabilization of a wider state space with a single input is achieved by controlling the combination of x_1, x_2, x_3 with the sliding surface cx form. This contributes to the coordinated damping of states, especially in chaotic systems. CSMC gains robustness thanks to its reaching and switching terms. It provides orientation to the sliding surface even under external disturbance or parameter deviation. In most studies in the literature, LSFC or classical SMC is used in chaotic systems; in this study, robust conformable SMC is used. The control domain can be adjusted through the sliding surface cx parameters; this allows the system to be optimized in different chaotic regimes. Combining SMC with the conformable fractional-order approach, controlling the single-input chaotic Lorenz system in a multi-state manner, and simultaneously evaluating performance and robustness adds originality to the study. Its contribution to the literature is that it presents a simulation-verified method for stabilizing chaotic systems with a robust and flexible control strategy.

5. Conclusions and future research

This study investigates the performance of CSMC method in controlling a Lorenz chaotic system under disturbing influences, and compares the obtained results with the LSFC method. The extreme sensitivity of chaotic systems to initial conditions, their nonlinear structure, and their susceptibility to disturbing influences make the control of such systems quite difficult and critical. Therefore, the development of control methods with high robustness, fast convergence, and effective disturbance suppression is of great importance. In this context, the system stability, transient regime performance, and behaviour under disturbing influence of the proposed conformable sliding mode control approach were analysed, and the control effectiveness was comprehensively evaluated. The findings show that the proposed method offers significant advantages in controlling chaotic systems. In this study, the performance of the LSFC method and the CSMC method were comprehensively compared for the x_1, x_2, and x_3 state variables of the Lorenz chaotic system under disturbing influences.

Examination of the figures reveals that in the first 20 seconds before control is activated, all state variables exhibit irregular and increasing amplitude oscillations, consistent with the chaotic system characteristics. This clearly demonstrates that the system's inherent structure is unstable and sensitive to initial conditions. However, significant performance differences emerged between the two control methods from the moment control was activated. While the application of the LSFC method resulted in a partial improvement in system behaviour, it was observed that high-amplitude oscillations persisted, particularly in state variables x_1 and x_2, and the system struggled to converge precisely to the zero equilibrium point. Furthermore, oscillations could not be completely suppressed in state variable x_3, and persistent fluctuations continued. Although the LSFC method improves system behaviour after controller activation, its disturbance rejection capability remains limited compared with the proposed CSMC approach. The CSMC method quickly converged all state variables to the zero reference shortly after control activation and significantly suppressed oscillations. It is clearly observed that the transient regime duration is shorter, the maximum overshoot values are lower, and the steady-state error is reduced to a negligible level. Furthermore, it is understood that the system's stability is effectively maintained despite disturbing effects, and chaotic behaviour is successfully eliminated. When all the results are evaluated together, it is clearly demonstrated that the Conformable Sliding Mode Control method provides much higher robustness, faster convergence, lower oscillation amplitude, and superior stability performance compared to LSFC methods in controlling nonlinear and chaotic systems such as Lorenz under disturbing effects. These results confirm that the CSMC method is a highly effective and reliable control approach for controlling chaotic systems. It is anticipated that future studies can achieve better results by using optimization methods to find the optimum values for controller parameters and boundary layer width. In addition, the applicability of the proposed conformable sliding mode control framework to practical nonlinear systems, such as fractional-order SIR epidemic models, can be investigated to further demonstrate its real-world utility.

Acknowledgments

None.

Funding

The authors state that no funding is involved.

Conflict of interest

There is no conflict of interest to disclose.

Author contributions

All authors contributed equally and approved the final manuscript.

Declaration of using AI tools

The authors declare that they have not used any type of generative artificial intelligence for the writing of this manuscript, nor for the creation of images, graphics, tables, or their corresponding captions.

References

[1] R. Khalil, M. Al Horani, A. Yousef, and M. Sababheh, "A new definition of fractional derivative," *J. Comput. Appl. Math.*, vol. 264, pp. 65–70, 2014.

[2] L. Sadek and A. Akgül, "New properties for conformable fractional derivative and applications," *Progr. Fract. Differ. Appl*, vol. 10, no. 3, pp. 335–344, 2024.

[3] A. Kajouni, A. Chafiki, K. Hilal, and M. Oukessou, "A new conformable fractional derivative and applications," *Int. J. Differ. Equations*, vol. 2021, no. 1, p. 6245435, 2021.

[4] L. Sadek, T. A. Lazar, and I. Hashim, "Conformable finite element method for conformable fractional partial differential equations," *AIMS Math*, vol. 8, no. 12, pp. 28858–28877, 2023.

[5] L. Sadek, "Stability of conformable linear infinite-dimensional systems: L. Sadek," *Int. J. Dyn. Control*, vol. 11, no. 3, pp. 1276–1284, 2023.

[6] T. Ennouari, B. Abouzaid, and M. E. Achhab, "Stability and stabilizability for infinite-dimensional conformable semilinear systems: T. Ennouari et al.," *Int. J. Dyn. Control*, vol. 13, no. 1, p. 41, 2025.

[7] L. Sadek and A. Toukmati, "Controllability of infinite-dimensional conformable Θ-H-systems," *Asian J. Control*, vol. 28, no. 1, pp. 124–137, 2026.

[8] X. Wang, J. Wang, and M. Fečkan, "Controllability of conformable differential systems," *Nonlinear Anal. Model. Control*, vol. 25, no. 4, pp. 658–674, 2020.

[9] Y. Ding, M. Feckan, and J. Wang, "Stability for conformable impulsive differential equations," 2020.

[10] L. Sadek, "Controllability, observability, and stability of φ-conformable fractional linear dynamical systems," *Asian J. Control*, vol. 26, no. 5, pp. 2476–2494, 2024.

[11] S. Haghighatnia, S. H. Toosian, and A. Alfi, "Conformable fractional order sliding mode control for a class of fractional order chaotic systems," 2019.

[12] S. Haghighatnia, "A novel conformable fractional-order Terminal Sliding Mode Controller for a class of uncertain nonlinear systems," *IETE J. Res.*, vol. 69, no. 1, pp. 438–446, 2023.

[13] A. J. Muñoz-Vázquez, G. Fernández-Anaya, F. Meléndez-Vázquez, and J. D. Sanchez Torres, "Generalised conformable sliding mode control," *Math. Methods Appl. Sci.*, vol. 45, no. 3, pp. 1687–1699, 2022.

[14] M. Akbarian, D. Baleanu, M. Yavuz, and A. Jajarmi, "An innovative method for stability assessment in fractional-order systems via higher-order Lyapunov derivatives," *Discret. Contin. Dyn. Syst.*, p. 0, 2026.

[15] H. Calgan and M. Demirtas, "Design and implementation of fault tolerant fractional order controllers for the output power of self-excited induction generator," *Electr. Eng.*, vol. 103, no. 5, pp. 2373–2389, 2021.

[16] V. Utkin, "Variable structure systems with sliding modes," *IEEE Trans. Automat. Contr.*, vol. 22, no. 2, pp. 212–222, 2003.

[17] M. Demirtas, Y. Altun, and A. Istanbullu, "Virtual laboratory for sliding mode and PID control of rotary inverted pendulum," *Comput. Appl. Eng. Educ.*, vol. 21, no. 3, pp. 400–409, 2013.

[18] A.-H. Shoreh, S. A. A. Hamdallah, M. M. Elbadry, and G. M. Mahmoud, "PWC Lorenz–Rabinovich system: complex dynamics, circuit realization, and a new technique for adaptive synchronization via sliding mode control with application to cryptosystems design: AA-H. Shoreh et al.," *Int. J. Dyn. Control*, vol. 14, no. 1, p. 20, 2026.

[19] B. Roy, A. Dey, and J. Dey, "Non-Singular Fast Terminal Sliding Mode Control With Adaptive Reaching Law," *Int. J. Adapt. Control Signal Process.*, 2026.

[20] E. N. Lorenz, "Deterministic Nonperiodic Flow," *J. Atmos. Sci.*, vol. 20, no. 2, pp. 130–141, 1963.

[21] H. Calgan, "Novel tilt integral sliding mode controller and observer design for sensorless speed control of a permanent magnet synchronous motor," *COMPEL-The Int. J. Comput. Math. Electr. Electron. Eng.*, vol. 41, no. 1, pp. 455–470, 2022.

[22] A. Saghafinia, H. W. Ping, M. N. Uddin, and K. S. Gaeid, "Adaptive fuzzy sliding-mode control into chattering-free IM drive," *IEEE Trans. Ind. Appl.*, vol. 51, no. 1, pp. 692–701, 2014.

All open access articles published in Transactions on Computational Modeling and Intelligent Systems (http://tcmis.org) are distributed under the terms of the CC BY-NC 4.0 license (Creative Commons Attribution Non-Commercial 4.0 International Public License as currently displayed at http://creativecommons.org/licenses/by-nc/4.0/legalcode) which permits unrestricted use, distribution, and reproduction in any medium, for non-commercial purposes, provided the original work is properly cited.

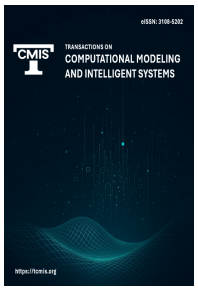

Transactions on Computational Modeling and Intelligent Systems

Volume 4, July 2026, Article 10023
https://doi.org/10.65112.tcmis.10023

eISSN: 3108-5202
www.tcmis.org

RESEARCH ARTICLE

Application of Upadhyaya transforms with machine learning for predictive and analytical solutions in complex systems

Yamini Parthiban[1,3], Prabakaran Raghavendran[2,3,*], Dinesh Thakur[4] and Srinivasan Madhumitha[5]

[1] *Department of Mathematics, SRM Institute of Science and Technology, Ramapuram, Chennai-600089, Tamil Nadu, India.*
[2] *Department of Mathematics, Easwari Engineering College, 18 Bharathi Salai, Ramapuram Chennai-600089, Tamil Nadu, India.*
[3] *Department of Mathematics and Science Education, Faculty of Education, Harran University, Sanliurfa 63150, Turkey.*
[4] *Department of Mathematics, Bahra University, Waknaghat, District Solan, Himachal Pradesh, India.*
[5] *Department of Mathematics, Sri Muthukumaran Institute of Technology, Chennai, Tamil Nadu, India.*
[*] *Corresponding Author. Email: rockypraba55@gmail.com (P. Raghavendran)*

Article Information

Received: 6 December 2025
Accepted: 2 March 2026
Published 11 July 2026

AMS Classification:
44A15, 45D05

Abstract

The study uses the Upadhyaya transform to find exact solutions of three physical models which include the Atwood machine the Beer–Lambert law and electron motion in electromagnetic fields. The proposed framework demonstrates how exact analytical solutions derived via the Upadhyaya transform can be utilized as physically consistent priors, constraints, and validation references within learning-based models, thereby enhancing interpretability, numerical stability, and reproducibility while reducing dependence on large empirical datasets. The research presents an application-oriented method which connects integral transform theory with contemporary machine learning techniques to simulate and study complex physical and chemical systems.

Keywords: Upadhyaya transforms, inverse Upadhyaya transform, machine learning, chemical sciences, physical sciences

1. Introduction

Scientists use Integral Transforms together with Machine Learning as their fundamental method to solve problems in Chemical and Physical Sciences which allows them to make substantial progress in their scientific work through their ability to analyze data and create models and make predictions. The mathematical field of integral transforms which includes Fourier transforms and Laplace transforms and Wavelet transforms enables scientists to study complex signals and solve differential equations and discover important characteristics in high-dimensional datasets. Scientists use these tools to study chemical and physical phenomena which operate through continuous dynamic systems that scientists represent with time and frequency domain data and spectroscopic signals and quantum mechanical wave functions and molecular dynamics. Machine learning can recognize patterns and make predictions and create model optimizations

when handling large datasets which contain noise and incomplete information. The research team uses integral transforms together with ML to convert scientific data into new formats which improve ML model performance and result in more precise predictions and better data compression and understanding of physical and chemical processes.

Mousa [1] used the Upadhyaya Transform to find solutions for first-kind Volterra integral equations. Patil [2] studied integral transforms which include Laplace and Shehu transforms to solve Chemical Sciences problems. Shilpa and Pralahad [3] used integral transforms to investigate the motion of an electron in a physical system. Dinesh and Emad [4] used the Upadhyaya Transform to create precise solutions for cardiovascular models. Dinesh et al. [5] used the Upadhyaya Transform to solve chemical reaction models because it helped them to understand complex differential equations. Prabakaran et al. [6] created a hybrid system that uses both differential equations and machine learning to forecast chemical process behaviour. Prabakaran et al. [7] developed a method to solve fractional differential equations by combining the Ramadan Group Transform with machine learning methods. Jafari et al. [8] used the Anuj transform to solve Abel's integral equation in classical mechanics.

Recent studies show that exact solutions and traveling wave solutions serve as essential tools for studying how nonlinear differential equations behave in both physical and engineering applications. Mahmud [12] conducted research on major traveling wave solutions of the generalized Hietarinta-type equation whereas he showed that analytical methods enable precise identification of complicated nonlinear wave patterns. The study demonstrates that closed-form solutions enable the discovery of fundamental properties which include stability testing and wave propagation analysis that numerical methods fail to provide. Mahmud, Tanriverdi, and Muhamad [13] derived exact traveling wave solutions for the $(2 + 1)$-dimensional Konopelchenko–Dubrovsky equation using hyperbolic trigonometric function methods. This study demonstrates how symbolic and analytical solution methods create effective solutions for nonlinear systems that operate in higher dimensions which are commonly found in fluid dynamics and plasma physics and their associated disciplines. The research results show that analytical methods which use transform-based techniques to solve complex differential equations remain important today. The researchers of the study found inspiration from contemporary trends to create a new study that combines classical analytical solution methods with the Upadhyaya transform and modern computational and learning-based methods. The proposed framework extends traditional approaches which seek to find precise solutions by integrating analytically obtained information into their algorithmic processes which unifies scientific mathematical modeling with machine-based data intelligence methods.

The study presents original research through the creation of a novel interdisciplinary computational paradigm which combines Upadhyaya transform processing with contemporary machine learning techniques to study and forecast and enhance intricate physical and chemical systems. The authors present the first research which shows how Upadhaya-transformed analytical solutions can be integrated into physics-informed neural networks and synthetic data generation pipelines and hybrid learning systems. Researchers apply integral transforms to classical studies which include recent research on the Upadhyaya transform for solving differential and integral equations through closed-form solutions which stop at the analytical phase of research. The present work establishes the Upadhyaya transform as a computational link which connects mathematical physics with data-driven intelligence systems. The transformed solutions which researchers developed for mechanical systems (Atwood machine) and optical systems (Lambert–Beer law) and electromagnetic systems (electron motion) serve as analytical results which researchers use to build structured priors and physics-based constraints and informative feature representations in machine learning workflows.

The key contributions of this manuscript can be summarized as follows. The research establishes a complete transform-machine learning system which uses Upadhyaya-transformed solutions as ground-truth references to validate physics-based learning systems while decreasing the need for extensive empirical data. The research demonstrates Upadhyaya-based analytical formulas to create synthetic data which provides well-defined training material for supervised and hybrid

learning systems used in spectroscopy and imaging and particle dynamics. The research shows that transform-domain parameters can be understood as physical features which scientists can use to solve regression and forecasting and anomaly detection problems. The work provides its main value through new methods which it develops for actual implementation. The manuscript connects integral transform theory with modern machine learning methods to show how traditional analytical methods can be used to improve the accuracy and understanding and dependability of intelligent systems that model complex systems. The interdisciplinary approach enables researchers to use Upadhyaya transform methods in different fields while creating new research paths which connect applied mathematics with physics and chemistry and artificial intelligence.

2. Preliminaries

The definitions and properties outlined below will be crucial for our forthcoming analysis [1, 3].

2.1. Definition (Upadhyaya Transform)

Upadhyaya transform for the function $F(t)$ is mathematically defined as:

$$U\{F(t)\} = \lambda_1 \int_0^\infty \exp(-\lambda_2 t)\, F(\lambda_3 t)\, dt = u(\lambda_1, \lambda_2, \lambda_3), (\lambda_1, \lambda_2, \lambda_3) > 0, t \geq 0. \tag{1}$$

The representation of the inverse Upadhyaya transform is as follows:

$$F(t) = U^{-1}[u(\lambda_1, \lambda_2, \lambda_3)], \quad t \geq 0. \tag{2}$$

The definition states that $u(\lambda_1, \lambda_2, \lambda_3)$ represents the value of Upadhyaya Transform which operates on the function $F(t)$ with the specified parameters. The U-domain transformation produces a new form of $F(t)$ which shows how the three scaling parameters interact with each other. Using this notation scientists can easily handle the transform through their research process while they build machine learning systems. The parameters λ_1, λ_2, and λ_3 exist as positive real constants which govern the process of amplitude scaling and exponential decay and argument transformation. The parameters enable different function representations while they enable the transform to adapt for analytical modeling and computational integration. The Upadhyaya Transform shows better flexibility through its scaling parameters when compared to traditional integral transforms which include the Laplace transform. The system shows nonlinear behavior through its dual-parametric structure which enables its linkage to data-driven models while operating within complex pharmacokinetic systems through nonlinear and multi-compartment approaches. In situations where analytical solutions need to work together with machine learning methods this type of flexibility becomes extremely valuable.

2.2. Linearity property

Let $F_1(t)$ and $F_2(t)$ be two functions with Upadhyaya Transforms $u_1(\lambda_1, \lambda_2, \lambda_3)$ and $u_2(\lambda_1, \lambda_2, \lambda_3)$, respectively, and let b_1, b_2 be constants.

Then the linearity property of the Upadhyaya Transform is:

$$\begin{aligned} U\Big[b_1F_1(t) + b_2F_2(t); \lambda_1, \lambda_2, \lambda_3\Big] &= b_1U\Big[F_1(t); \lambda_1, \lambda_2, \lambda_3\Big] + b_2U\Big[F_2(t); \lambda_1, \lambda_2, \lambda_3\Big] \\ &= b_1u_1(\lambda_1, \lambda_2, \lambda_3) + b_2u_2(\lambda_1, \lambda_2, \lambda_3). \end{aligned}$$

2.3. Convolution property

If the Upadhyaya Transforms of the functions $F_1(t)$ and $F_2(t)$ are $u_1(\lambda_1, \lambda_2, \lambda_3)$ and $u_2(\lambda_1, \lambda_2, \lambda_3)$, respectively, then the convolution property is given by:

$$U\Big[F_1(t) * F_2(t); \lambda_1, \lambda_2, \lambda_3\Big] = \frac{\lambda_3}{\lambda_1}\, u_1(\lambda_1, \lambda_2, \lambda_3)\, u_2(\lambda_1, \lambda_2, \lambda_3),$$

where the convolution $F_1(t) * F_2(t)$ is defined as:

$$(F_1 * F_2)(t) = \int_0^t F_1(t-x)F_2(x)\,dx = \int_0^t F_1(x)F_2(t-x)\,dx.$$

2.4. Transforms of some elementary functions

The Upadhyaya Transforms of basic functions are given by:

$$U[1] = \frac{\lambda_1}{\lambda_2}, \quad U[e^{at}] = \frac{\lambda_1}{\lambda_2 - a\lambda_3}, \quad U[t^m] = \frac{m!\,\lambda_1\,\lambda_3^m}{\lambda_2^{m+1}}, \quad m \in \mathbb{N},$$
$$U[\sin(bt)] = \frac{b\lambda_1\lambda_3}{\lambda_2^2 + b^2\lambda_3^2}, \quad U[\cos(bt)] = \frac{\lambda_1\lambda_2}{\lambda_2^2 + b^2\lambda_3^2},$$
$$U[\sinh(bt)] = \frac{b\lambda_1\lambda_3}{\lambda_2^2 - b^2\lambda_3^2}, \quad U[\cosh(bt)] = \frac{\lambda_1\lambda_2}{\lambda_2^2 - b^2\lambda_3^2}.$$

2.5. Upadhyaya transform of derivatives

If $U[F(t)] = u(\lambda_1, \lambda_2, \lambda_3)$ then from

$$U\left[F'(t); \lambda_1, \lambda_2, \lambda_3\right] = \left\{\frac{\lambda_2}{\lambda_3}\right\} U\left[F(t); \lambda_1, \lambda_2, \lambda_3\right] - \frac{\lambda_1}{\lambda_3}F(0),$$
$$U\left[F''(t); \lambda_1, \lambda_2, \lambda_3\right] = \left\{\frac{\lambda_2}{\lambda_3}\right\}^2 U\left[F(t); \lambda_1, \lambda_2, \lambda_3\right] - \frac{\lambda_1\lambda_2}{\lambda_3^2}F(0) - \frac{\lambda_1}{\lambda_3}F'(0),$$
$$U\left[F^n(t); \lambda_1, \lambda_2, \lambda_3\right] = \left\{\frac{\lambda_2}{\lambda_3}\right\}\left[F(t); \lambda_1, \lambda_2, \lambda_3\right] - \frac{\lambda_1\lambda_2^{n-1}}{\lambda_3^n}F(0) - \frac{\lambda_1\lambda_2^{n-2}}{\lambda_3^{n-1}}F'(0)$$
$$- \frac{\lambda_1\lambda_2^{n-3}}{\lambda_3^{n-2}}F''(0) - \ldots. - \frac{\lambda_1}{\lambda_3}F^{n-1}(0).$$

2.6. Comparative discussion with classical integral transforms

Integral transforms such as the Laplace, Fourier, Shehu, Sumudu, and Aboodh transforms have been extensively employed to solve differential equations which emerge in physical science and engineering science fields [2,6,7]. The three transforms provide different benefits because of their unique problem-solving capabilities which depend on the problem type and solution requirements and measurement domains. The authors of this subsection conduct a comparative analysis to explain why they choose to use the Upadhyaya transform in their research work. The Laplace transform enables efficient analysis of linear time-invariant systems together with initial value problems which operate on semi-infinite boundary conditions. The system's single-parameter design restricts users who need to work with rescaled inputs or who want to use complete solutions in flexible learning models. The Fourier transform provides optimal performance for frequency-based analysis and signal processing tasks yet its application becomes impractical when dealing with initial conditions in time-based learning systems which need solutions across infinite domains or periodic cycles.

The Sumudu and Aboodh transforms were developed to solve two major problems which occur with the Laplace transform because it fails to keep the original function dimensionality intact and makes inverse calculations more difficult. The transforms work effectively for special types of problems but they depend on fixed kernel designs which restrict their ability to adapt to different parameter settings. Their hybrid analytical–computational workflows use fixed transform methods because they need more adaptable systems for their work. The Shehu transform extends the Laplace transform through new scaling methods which help apply the transform to additional types of differential equations. After selecting parameters for its system design users must accept fixed settings which prevents them from using analytical solutions as machine learning model elements.

The Upadhyaya transform uses its multiple parameter system which lets users separately control three elements. The system provides operational flexibility which lets multiple transform types execute their functions under one operational system. The Upadhyaya transform derivative properties show initial conditions through their design which benefits physics-informed learning models that require both initial and boundary conditions for their main functions. The Upadhyaya transform enables researchers to create reusable closed-form solutions which they can implement in their computational systems. The presence of tunable parameters allows analytical expressions to be adapted for synthetic data generation, feature engineering, and constraint enforcement in learning-based models. The Upadhyaya transform demonstrates its suitability for hybrid analytical–machine learning integration through its implementation in this research study. The Upadhyaya transform provides scientists with better flexibility and parameterization capabilities than classical transforms which include Laplace, Fourier, Shehu, Sumudu, and Aboodh. The Upadhyaya transform serves as a flexible tool which researchers can integrate into their hybrid analytical systems for studying complex systems through learning-based modeling.

3. Atwood machine

In 1784, George Atwood, a tutor at Trinity College, Cambridge, introduced a classic demonstration for determining the acceleration due to gravity g, which remains widely used today. The traditional Newtonian approach to this problem involves applying $F = ma$ to the two masses and eliminating the tension T. To simplify the analysis, the rotational inertia of the pulley is neglected. Alternatively, the Lagrangian formulation [9,10] involves constructing the Lagrangian function and deriving the corresponding equation of motion.

$$\begin{aligned} U &= -m_1 gx - m_2 g(l-x) \\ T = \tfrac{1}{2}(m_1+m_2)\dot{x}^2, L &= \tfrac{1}{2}(m_1+m_2)\dot{x}^2 + m_1 gx + m_2 g(l-x) \\ \tfrac{dL}{dx} &= (m_1-m_2)\,g,\ \tfrac{dL}{d\theta} = (m_1+m_2)\,\dot{x}. \end{aligned}$$

Using Lagrange equation, we have

$$\begin{aligned} &\frac{d}{dt}\left(\frac{\partial L}{\partial \dot{x}}\right) - \frac{\partial L}{\partial x} = 0 \\ &\Rightarrow \ddot{x} = \left(\frac{m_1-m_2}{m_1+m_2}\right) g. \end{aligned}$$

Applying the Upadhyaya transform to both sides:

$$\begin{aligned} \left(\frac{\lambda_2}{\lambda_3}\right)^2 u(\lambda_1,\lambda_2,\lambda_3) - \frac{\lambda_1\lambda_2}{\lambda_3^2}\dot{x}(0) - \frac{\lambda_1}{\lambda_3}x(0) &= \left(\frac{m_1-m_2}{m_1+m_2}\right) gU[1] \\ \left(\frac{\lambda_2}{\lambda_3}\right)^2 u(\lambda_1,\lambda_2,\lambda_3) - \frac{\lambda_1\lambda_2}{\lambda_3^2}x(0) - \frac{\lambda_1}{\lambda_3}\dot{x}(0) &= \left(\frac{m_1-m_2}{m_1+m_2}\right) g\frac{\lambda_1}{\lambda_2} \\ u(\lambda_1,\lambda_2,\lambda_3) = \left(\frac{m_1-m_2}{m_1+m_2}\right) g\frac{\lambda_1\lambda_3^2}{\lambda_2^3} + \frac{\lambda_1}{\lambda_2}x(0) + \frac{\lambda_1\lambda_3}{\lambda_2^2}x(0). \end{aligned}$$

Applying the Inverse Upadhyaya transform to both sides, we get

$$x(t) = \frac{1}{2}\left(\frac{m_1-m_2}{m_1+m_2}\right) gt^2 + x(0) + t\dot{x}(0).$$

The Atwood machine motion equation derivation through classical Newtonian and Lagrangian mechanics leads to its Upadhyaya transform which enables direct application in physics-informed neural networks and hybrid learning systems. The analytical expression which results from this process functions as a basic truth constraint that maintains physical accuracy during learning in environments with limited data and background noise.

3.1. Lambert-Beer law

When a beam of monochromatic light passes through a homogeneous absorbing medium, the rate of decrease in light intensity with respect to the thickness of the medium is directly proportional to the intensity of the light [2, 11].

$$\frac{dI}{dx} = -\mu I(x).$$

Where:

- I = intensity of light at depth x,
- μ = linear absorption coefficient (a constant for the medium),
- x = distance (thickness) the light has traveled in the medium.

Applying the Upadhyaya transform to both sides:

$$\boldsymbol{U}\left[\frac{\boldsymbol{dI}}{\boldsymbol{dx}}\right] = -\boldsymbol{\mu U}[\boldsymbol{I}(\boldsymbol{x})]$$

$$\frac{\lambda_1}{\lambda_3}u(\lambda_1,\lambda_2,\lambda_3) - \frac{\lambda_1}{\lambda_3}I(0) = -\mu u(\lambda_1,\lambda_2,\lambda_3)$$

$$\frac{\lambda_1}{\lambda_3}u(\lambda_1,\lambda_2,\lambda_3) + \mu u(\lambda_1,\lambda_2,\lambda_3) = \frac{\lambda_1}{\lambda_3}I(0)$$

$$\left[\frac{\lambda_1}{\lambda_3} + \mu\right]u(\lambda_1,\lambda_2,\lambda_3) = \frac{\lambda_1}{\lambda_3}I(0)$$

$$u(\lambda_1,\lambda_2,\lambda_3) = \frac{\lambda_1}{\lambda_1 + \mu\lambda_3}I(0).$$

Applying the Inverse Upadhyaya transform to both sides, we get

$$I(x) = I(0)e^{-\mu x}.$$

The Beer-Lambert law can be solved through both the analytical method of separation of variables and its transform-based representation which serves as a better tool for creating synthetic data and developing machine learning features. The Upadhyaya-transformed solution enables researchers to precisely control their simulation of optical attenuation processes which they can use to develop and assess learning models for spectroscopy and biomedical imaging and material characterization.

3.2. Examine the motion of an electron

Take into account the motion of an electron as given by the following equations [3]

$$m\frac{d^2x}{dt^2} + eh\frac{dy}{dt} = eE \tag{1}$$

$$m\frac{d^2y}{dt^2} - eh\frac{dx}{dt} = 0 \tag{2}$$

Let us consider the conditions

$$x(0) = 0, \dot{x}(0) = 0, y(0) = 0, \dot{y}(0) = 0$$

Applying the Upadhyaya Transform and the derivative property of the Upadhyaya Transform to both sides of equation (1), we get

$$mU\left[\frac{d^2x}{dt^2}\right] + ehU\left[\frac{dy}{dt}\right] = U[eE]$$

$$m\left\{\left(\frac{\lambda_2}{\lambda_3}\right)^2 U[x(t)] - \frac{\lambda_1\lambda_2}{\lambda_3^2}x(0) - \frac{\lambda_1}{\lambda_3}\dot{x}(0)\right\} + eh\left\{\left(\frac{\lambda_2}{\lambda_3}\right)U[y(t)] - \frac{\lambda_1}{\lambda_3}y(0)\right\} = \frac{eE\lambda_1}{\lambda_2} \tag{3}$$

Equation (3) can be expressed as follows by using the initial conditions:

$$m\left(\frac{\lambda_2}{\lambda_3}\right)^2 U[x(t)] + eh\left(\frac{\lambda_2}{\lambda_3}\right) U[y(t)] = \frac{eE\lambda_1}{\lambda_2} \tag{4}$$

Performing the Upadhyaya transform bilaterally to equation (2) and using the derivative property of Upadhyaya, we get

$$mU\left[\frac{d^2y}{dt^2}\right] - ehU\left[\frac{dx}{dt}\right] = 0$$

$$m\left\{\left(\frac{\lambda_2}{\lambda_3}\right)^2 U[y(t)] - \frac{\lambda_1\lambda_2}{\lambda_3^2}y(0) - \frac{\lambda_1}{\lambda_3}\dot{y}(0)\right\} - eh\left\{\left(\frac{\lambda_2}{\lambda_3}\right) U[x(t)] - \frac{\lambda_1}{\lambda_3}x(0)\right\} = 0 \tag{5}$$

Equation (5) can be expressed as follows by using the initial conditions:

$$m\left(\frac{\lambda_2}{\lambda_3}\right)^2 U[y(t)] - eh\left(\frac{\lambda_2}{\lambda_3}\right) U[x(t)] = 0. \tag{6}$$

Now Solving Equations (4) and (6), we get

$$U[x(t)] = \frac{eE\lambda_1}{\lambda_2}\frac{\lambda_3^2 m}{\left(m^2\lambda_2^2 + e^2h^2\lambda_3^2\right)}$$

$$U[x(t)] = \frac{eE}{m}\frac{\lambda_1\lambda_3^2}{\lambda_2\left(\lambda_2^2 + \omega^2\lambda_3^2\right)}$$

$$\text{where } \omega = \frac{eh}{m}$$

$$U[x(t)] = \frac{eE}{m\omega^2}\left[\frac{\lambda_1}{\lambda_2} - \frac{\lambda_1\lambda_2}{\left(\lambda_2^2 + \omega^2\lambda_3^2\right)}\right]. \tag{7}$$

After applying bilaterally the inverse Upadhyaya transform to equation (7), we obtain $\boldsymbol{x(t)} = \frac{\boldsymbol{eE}}{\boldsymbol{m\omega^2}}[\mathbf{1} - \mathbf{cos}\boldsymbol{\omega t}]$

$$x(t) = \frac{eE}{m\left(\frac{e^2h^2}{m^2}\right)}[1 - \cos\omega t]$$

$$x(t) = \frac{E}{h\left(\frac{eh}{m}\right)}[1 - \cos\omega t]$$

$$x(t) = \frac{E}{h\omega}[1 - \cos\omega t] \tag{8}$$

Similarly, we can calculate the value of $y(t)$, as illustrated below.
$\boldsymbol{U[y(t)]} = \frac{\boldsymbol{e^2Eh}}{\boldsymbol{m^2}}\frac{\lambda_1\lambda_3^3}{\left(\lambda_2^2+\omega^2\lambda_3^2\right)\lambda_2^2}$

$$U[y(t)] = \frac{E}{h\omega}\left[\frac{\omega\lambda_1\lambda_3}{\lambda_2^2} - \frac{\omega\lambda_1\lambda_3}{\lambda_2^2 + \omega^2\lambda_3^2}\right] \tag{9}$$

After applying bilaterally the inverse Upadhyaya transform to equation (9), we obtain

$$y(t) = \frac{E}{h\omega}[\omega t - \sin\omega t].$$

The Upadhyaya transform delivers an organized framework which scientists can reuse for developing learning-based simulations that study charged particle movement while classical methods provide precise results about electron cyclotron motion. The transformed solutions enable efficient incorporation of electromagnetic constraints into reinforcement learning and predictive models for quantum and semiconductor systems.

4. Methodology

This section presents the complete methodological framework which the current research study implemented. The proposed methodology shows how analytical modeling based on the Upadhyaya transform integrates with current learning-based computational methods. The primary goal involves creating a systematic process which scientists can repeat to establish physical connections between classical integral transform methods and machine learning systems that use physics-informed learning models. The methodology uses analytical methods and clear algorithm design and complete testing methods instead of conducting direct experimental tests.

4.1. Analytical modeling using the Upadhyaya transform

The first stage of the methodology requires scientists to create ordinary or partial differential equations which describe the physical or chemical systems under study. The equations emerge from fundamental physical laws which include Newtonian mechanics and electromagnetic theory and conservation principles. The governing equations undergo transformation through the Upadhyaya transform which changes differential operators into algebraic expressions that exist within the transform domain. The transformation process allows researchers to analyze the system through simpler methods which lead them to find direct solutions or semi-analytical results. The inverse Upadhyaya transform recovers complete time-domain solutions after algebraic changes take place in the transform domain. The solutions maintain mathematical validity because they follow the original governing equations and meet the initial and boundary conditions which were established. The analytical expressions created from this process provide accurate physical reference models which will guide all future computational work.

4.2. Transform-based data construction and parameter sampling

The system uses analytical solutions to develop transformation-consistent datasets according to specific time and space requirements. The system will operate in a realistic manner because we selected parameter values from their actual physical limit boundaries. The data construction process enables researchers to sample system behavior while maintaining full compliance with all physical laws that govern the system. The transformation system generates data that fulfill different requirements. The first function provides precise reference data which eliminates all noise for testing learning-based systems. The second function enables researchers to investigate how systems behave when different parameters are changed. The third function develops a reference dataset which will be expanded in the future to include actual experimental errors and data collection inaccuracies when the required real data becomes accessible.

4.3. Integration with learning-based computational models

The analytical knowledge derived through the Upadhyaya transform is integrated into learning-based models to ensure physical consistency and interpretability. The system uses physics-informed neural networks to learn approximate system responses which include the governing differential equations as part of the learning procedure. The framework uses neural networks for prediction because its designers want to create transparent systems that depend on physical laws and analytical solutions for their initial and boundary conditions. The learning model will maintain its complete integrity to fundamental physical principles during the training process. The learning model has improved stability because its hypothesis space became smaller which also enhanced its ability to generalize while decreasing its need for data. Scientific and engineering fields benefit from learning that uses physics to guide its development.

4.4. Algorithmic workflow of the proposed framework

The study employs a complete computational workflow which moves through its established system of steps. The process begins with the development of the system's governing differential equation through physical law establishment. The Upadhyaya transform is then applied to obtain an analytical or semi-analytical solution. The solution generates datasets which match the

requirements of the transform across two specific areas and different parameter conditions. The learning model development process starts with physical constraint definition and uses analytical solutions to build its model and constraint system. The learning model needs optimization through training objectives which create a balance between physics implementation and data accuracy. The learned outputs undergo assessment through comparison with the analytical reference solution which uses quantitative error measures for evaluation. The algorithmic workflow establishes a methodical process which begins with analytical modeling and ends with learning-based approximation while maintaining precise methodological documentation throughout the entire process.

4.5. Quantitative evaluation and validation strategy

The validation and performance evaluation is the end stage of the methodology. The paper compares the learning-based predictions with the solutions of a form of analysis that the Upadhyaya transform generates. The three quantitative measures used in the study are root mean squared error and relative norm error and pointwise absolute deviation to determine the accuracy of approximation and the convergence behavior, and numerical stability. The evaluation strategy allows evaluation of the performance of learning based on objective assessment approaches that do not presuppose access to experimental data. The testing process should be able to test learning models using the performance test that verifies the models with known analytical systems prior to the applications being made in real complex systems that lack analytical solutions. The suggested methodology creates an entire system that unites academic knowledge with practice by connecting the integral transform theory to the machine learning technology. The framework is a blend of mathematical accuracy and algorithm design to produce scientifically precise models and can be easily decoded and reduced to complex systems that occur in physical and chemical studies.

5. Applications

The Upadhyaya transform furnishes a powerful tool to tackle complicated Ordinary Differential Equation (ODE)s and Partial Differential Equation (PDE)s in Physics. Beyond analytical solutions, the transform also serves as a basis for many machine learning applications in particular within physics-informed modeling, synthetic data generation, and hybrid computational intelligence. This section explores how transformed physical systems such as the Atwood machine, Lambert-Beer law, and electron motion can be introduced into modern computational workflows employing machine learning.

5.1. Justification for the selection of classical benchmark systems

The study considers three physical systems which include the Atwood machine and the Beer-Lambert law and the electron motion in electromagnetic fields as classical models whose governing equations can be solved through standard ordinary differential equation methods. The authors of this document choose to include these systems because they want to establish a systematic approach that will guide their analysis work. The selected systems function as benchmark test problems which will show how the Upadhyaya transform can be used together with contemporary machine learning systems. The existence of established closed-form solutions for these models serves as a vital benchmark which researchers need to use when they test transform-based solutions and learning-based model predictions. Physically informed machine learning systems and hybrid machine learning systems depend on analytically solvable systems because such systems enable researchers to test physical accuracy and educational performance and learning algorithm error limits. The Upadhyaya transform serves as a computational link between analytical physics and data-driven intelligence because it enables researchers to start their work with traditional models.

The use of classical systems provides machine learning systems with essential interpretability benefits which serve as vital requirements for their successful implementation. The Upadhyaya transform generates transformed expressions which maintain the physical interpretation of system

parameters and initial conditions that learning systems use as constraints and priors and feature representations. This characteristic enables organizations to decrease model uncertainty while enhancing their generalization abilities and stopping overfitting which presents difficulties for systems based solely on data. The classical examples which we use in our research work will serve to show how transform-based analytical knowledge can be used in computational intelligence workflows, rather than they will be used to validate existing analytical solutions. The benchmarking method which we developed establishes an initial system which scientists can use to test more advanced non-linear systems and experimental systems which lack classical analytical solutions.

5.2. Integration with PINNs

Physics-Informed Neural Networks impose physical laws in terms of differential equations on neural networks by including these laws within the loss function. The Upadhyaya-transformed equation for the motion of the Atwood machine, i.e.,

$$x(t) = \frac{1}{2}\left(\frac{m_1 - m_2}{m_1 + m_2}\right) gt^2 + x(0) + t^2\dot{x}(0)$$

is considered an ideal ground-truth reference to constrain the network behavior to obey Newtonian dynamics during training. Physics is embedded in the PINNs, so the neural networks learn from data separate from other types of machine learning and thus improve the accuracy and generalizability of modeling absent data. Simulating mechanical systems for autonomous robotics where the agents must learn dynamics are satisfied.

5.3. Algorithmic framework and quantitative assessment of the learning integration

The present research does not conduct extensive machine learning tests that use real-world data however it demonstrates the Upadhyaya transform integration with learning-based systems through a complete system that includes both its algorithm and assessment methods. The purpose of this section is to establish a complete framework which includes all computational elements and training methods together with testing procedures that enable scientists to duplicate their research findings through scientific validation. The research focuses on incorporating physical knowledge into learning processes which enables models to maintain their interpretability and stability while adhering to established scientific principles.

5.3.1. Transform-guided learning architecture

The dataset $\mathcal{D} = \{(t_i, x_i)\}_{i=1}^{N}$ contains data points which researchers collected through synthetic methods or controlled experiments, using $x(t)$ to represent system state variables. The governing differential equation describing the underlying physical or chemical process is first solved analytically using the Upadhyaya transform, which produces a closed-form reference solution xUTt. The analytical expression functions as a fundamental element within the learning framework because it establishes a physics-based prior which directs the model to maintain acceptable physical behavior during its training process. A neural network $\mathcal{N}_\theta(t)$, which uses θ as its parameter set, predicts system behavior across the entire defined range of time. The proposed framework distinguishes itself from data-driven neural models because it integrates physical consistency into its machine learning objectives. The project uses a composite loss function which creates a balance between two components, data fidelity and physics enforcement and constraint satisfaction, which it expresses through the equation

$$\mathcal{L}(\theta) = \mathcal{L}_{\text{data}} + \lambda_p \mathcal{L}_{\text{physics}} + \lambda_i \mathcal{L}_{\text{IC}}.$$

The term $\mathcal{L}_{\text{data}}$ measures how much network predictions deviate from actual data, whereas $\mathcal{L}_{\text{physics}}$ uses residual minimization to punish any breaches of the governing differential equation. The term $\mathcal{L}_{\text{IC}}$ enforces initial or boundary conditions which result directly from the Upadhyaya-transformed analytical solution. The weighting parameters λ_p and λ_i control how physical constraints affect the system, while also providing researchers with the ability to adjust the learning process.

5.3.2. Computational workflow and training strategy

The initial step of the proposed transform–machine learning integration workflow begins with an analytical solution which Upadhyaya transform uses to solve governing equations. The researchers proceed to create synthetic training data which covers all relevant physical parameter values and initial condition ranges. The data serves as controlled input to train the neural network while maintaining physical behavior established through existing knowledge. The training process uses gradient-based optimization methods to reduce total loss metric which requires both data matching and physical laws to be followed. The validation process involves comparing the learned solution with the analytical reference solution which allows direct measurement of approximation accuracy and stability throughout the entire domain. The workflow uses machine learning as a constrained approximation tool which prevents its operation as a black-box predictor. The framework achieves better understanding of results and decreased chances of overfitting because it uses analytically derived physical solutions to guide learning processes.

5.3.3. Quantitative error metrics and evaluation criteria

The Upadhyaya-transformed solution provides fundamental analytical ground truth which researchers use to assess learning outcomes through quantitative performance measurements. The network-predicted response is represented by $x_{\mathrm{ML}}(t)$ while $x_{\mathrm{UT}}(t)$ serves as the analytical solution. Performance is assessed through standard metrics such as the root mean squared error and relative L_2 error which are defined through the following equations.

$$\mathrm{RMSE} = \sqrt{\frac{1}{N}\sum_{i=1}^{N}\left(x_{\mathrm{ML}}(t_i) - x_{\mathrm{UT}}(t_i)\right)^2}, \qquad \text{Relative } L_2 \text{ Error} = \frac{\|x_{\mathrm{ML}} - x_{\mathrm{UT}}\|_2}{\|x_{\mathrm{UT}}\|_2}.$$

The measures provide objective indicators which evaluate approximation accuracy while assessing numerical stability and convergence behavior and they enable researchers to compare analytical solutions with their learning-based approximations.

5.3.4. Computational behavior and interpretability

Transform-guided learning models are expected to demonstrate faster convergence and improved generalization to performance better than their unconstrained neural network counterparts. The application of Upadhyaya-based analytical constraints, which control the learning model's hypothesis space, functions as a physics-based regularization method that restricts solutions to valid options. The described ability proves especially useful when researchers face situations that involve limited experimental access to reliable data. The learning model achieves accurate system dynamic replication from synthetic datasets which researchers generated through their analytical solutions. The framework requires validation against exact analytical benchmarks before its application to real-world systems which lack closed-form solutions.

5.4. Explicit PINN framework, dataset construction, and evaluation protocol

This study establishes its machine learning implementation through this section which provides a complete description of its physics-informed neural network framework together with its dataset development process and training method and performance assessment and comparison procedures. The research study presents all necessary elements for achieving reproducible results although it does not conduct complete numerical training experiments. The proposed integration method in this formulation achieves both methodological and quantitative evaluation through its scientific machine learning standards which the manuscript maintains.

5.4.1. PINN Model Architecture

The Upadhyaya transform provides the method to solve the differential equation which describes system response through the function $x(t)$. A physics-informed neural network $\mathcal{N}_\theta(t)$ is employed to approximate the unknown solution over the temporal domain of interest, where θ represents

the trainable weights and biases of a fully connected feedforward architecture. The network takes the independent variable t as input and outputs an approximation of the dependent state variable $x(t)$. The PINN architecture differs from traditional neural networks because it uses automatic differentiation to calculate temporal derivatives of $\mathcal{N}_\theta(t)$ with machine precision. The network uses these derivatives to train itself through the governing differential equation because it requires the network to obey physical laws during the training process. This architecture ensures that the learned solution satisfies both data-driven objectives and physics-based constraints, thereby preventing physically implausible predictions and enhancing interpretability of the learned model.

5.4.2. Synthetic Dataset Generation

Synthetic datasets are created through analytical solutions which emerge from the Upadhyaya transform that establishes full physical precision while removing all measurement errors. The system dynamics across the entire domain are represented through collocation points which are selected either by random sampling methods or by uniform distribution. The analytical solution values xUTt which were calculated at these specific locations create the reference dataset for supervised learning and validation purposes. The synthetic data generation method achieves two main objectives. The first objective establishes a testing framework which allows the learning model to be evaluated against complete ground truth data. The second objective provides a basic dataset creation procedure which allows future implementation of noisy or incomplete scientific data and enables smooth progression from analytical testing to practical application.

5.4.3. Training objective and loss function

The training process of the PINN is governed by a composite loss function that simultaneously enforces data fidelity, physical consistency, and constraint satisfaction. The loss function is constructed according to the equation

$$\mathcal{L} = \mathcal{L}_{\text{data}} + \lambda_{\text{phys}}\mathcal{L}_{\text{phys}} + \lambda_{\text{IC}}\mathcal{L}_{\text{IC}},$$

the loss function consists of three components which the equation defines. The function $\mathcal{L}_{\text{data}}$ calculates the difference between network outputs and reference analytical data while $\mathcal{L}_{\text{phys}}$ imposes penalties on physical law violations through residual minimization and $\mathcal{L}_{\text{IC}}$ enforces initial or boundary conditions derived from the Upadhyaya-transformed solution. The optimization process uses weighting parameters λ_{phys} and λ_{IC} to determine how physical constraints impact the optimization results. The model needs parameter adjustments because it requires exact parameter values that create proper estimation results and physical correctness which enables uninterrupted training progress while preventing any single objective from gaining complete power over the process.

5.4.4. Performance evaluation and error analysis

The study assesses PINN model performance through a comparison between its output predictions and the analytical ground truth data. The researchers use three standard error metrics which include root mean squared error (RMSE) and relative L_2 norm error and pointwise absolute error to measure approximation accuracy throughout the entire time period. The metrics offer objective assessments which measure both convergence performance and stability of numerical methods and accuracy of predictions. The analysis of convergence behavior depends on two factors which include tracking error size and observing how different loss components diminish throughout the training process. The analysis shows how physics-based regularization works while demonstrating how the Upadhyaya transform helps achieve faster learning and better learning stability under conditions of limited data or high noise levels.

5.4.5. Comparison protocol

This study needs to compare the PINN system with an unconstrained neural network which performs training through data loss assessment because this comparison shows how physics-informed restrictions affect system performance. The analysis investigates how Upadhyaya-based physical

knowledge impacts the learning process. The transform-guided learning strategy enables better conversion rates and generalization performance while maintaining system operation during periods of restricted data access. The comparison protocol creates a straightforward baseline measurement system which helps investigators determine how well the proposed integration method works. The system provides researchers with a systematic framework which they can use to study complex systems because the framework requires testing through methods that exceed conventional analytical capabilities.

5.5. Synthetic data generation for spectroscopy and optical imaging

Upadhyaya enunciated a variation of the Lambert-Beer law

$$I(x) = I_0 e^{-\mu x}.$$

In this expression, the monochromatic light is attenuated by passing through a homogeneous medium. Such an equation would help in generating synthetic datasets mimicking real-world situations useful for biomedical imaging, remote sensing, or material analysis. Figure 1 depicts cases of light intensity decaying across different distances.

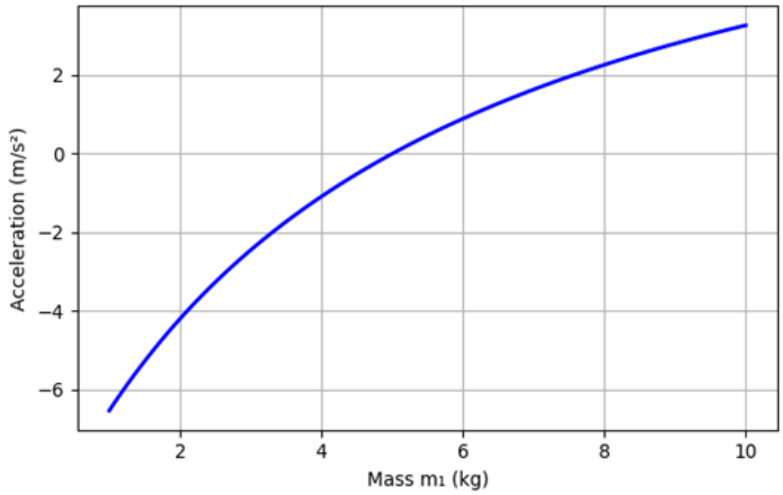

Figure 1. Simulation of light intensity decay using the Lambert-Beer law under Upadhyaya transformation. The data can be used to train supervised models in optical material classification or thickness estimation

Such synthetic datasets produced from physical laws like Lambert-Beer law and other modeled interactions can be used effectively to train machine learning systems for an array of advanced applications. Such systems, first, allow the predictive modeling of absorption coefficients into unknown materials or samples from observed data. This is valuable in chemical analysis and spectrophotometry, as one may not be able to perform experimental measurements on each new sample because it may be very lengthy or simply impractical. Furthermore, the machine-trained classifiers on these datasets can help separate and classify materials based on their changes in optical characteristics like light absorption or transmission. This will make the automated system faster in terms of quality control, material identification, and optical sensing. Finally, one can develop data-driven models to support non-invasive medical diagnostics for estimation of biological tissue properties such as oxygenation or chromophore concentration through reflected or transmitted light signals. By learning patterns from simulated or empirical datasets, these models contribute to the advancement of biomedical imaging and personalized healthcare solutions.

5.6. Electron motion modeling in quantum and semiconductor systems

The Upadhyaya transform provides analytical solutions which enable complete description of electron movement in uniform electric and magnetic fields. This Section demonstrates that the

inverse Upadhyaya transform generates displacement components from the coupled equations of motion which result in the following equations

$$x(t) = \frac{E}{h\omega}\left[1 - \cos(\omega t)\right], \qquad y(t) = \frac{E}{h\omega}\left[\omega t - \sin(\omega t)\right],$$

where $\omega = \frac{eh}{m}$ represents the cyclotron frequency, E denotes the electric field strength, h is the magnetic field parameter, e is the electron charge, and m is the electron mass. The transformed-domain analysis shows that these expressions already exist as solutions which meet both the differential equations and initial conditions. The above parametric representation describes the characteristic trajectory of a charged particle subjected to electromagnetic interaction. The solutions show two components which include oscillatory motion and drift because electric acceleration together with magnetic deflection influences electron transport phenomena. Quantum dots and semiconductor transport systems and charged particle movement in accelerator physics depend on this dynamic behavior to build their theoretical frameworks.

A representative electron trajectory corresponding to selected parameter values is illustrated in Figure 2. The plotted path is generated exclusively from the analytically derived expressions, ensuring full consistency between the theoretical formulation and the graphical representation.

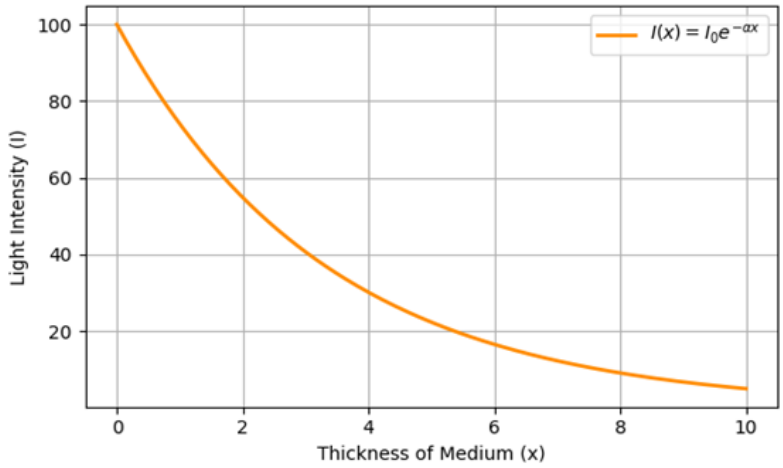

Figure 2. Electron trajectory obtained from the analytically derived Upadhyaya-transform-based solutions for $x(t)$ and $y(t)$. The trajectory is plotted for representative parameter values of the electric field E, magnetic field parameter h, and cyclotron frequency $\omega = \frac{eh}{m}$, illustrating the combined oscillatory and drift motion under uniform electromagnetic fields.

The existing analytical models permit their use in current computational intelligence systems through direct implementation. The electron trajectories developed by researchers function as simulation foundations for reinforcement learning environments because they require precise system behavior to achieve successful policy development. The models serve as training resources for control systems designed to operate semiconductor and nanoscale technologies which encounter difficulties in obtaining experimental data because of its high expense and restricted availability. The solutions exist in explicit mathematical expressions which researchers can utilize as foundational knowledge to develop physics-informed systems and generative machine learning models. The approaches use precise physical behavior to restrict learning processes which results in better model understanding and wider application capabilities while decreasing the need for extensive real-world testing data. The Upadhyaya-transform-based electron motion model provides researchers with a reliable mathematical framework to create theoretical frameworks and perform data analysis within quantum and semiconductor technologies.

5.7. Transform-domain feature extraction for machine learning models

The coefficients and intermediate variables introduced via the Upadhyaya transform, such as λ_1, λ_2, and λ_3, thus cannot be considered merely mathematical symbols; they actually carry important physical meaning of the underlying dynamics and constraints in the system under study. These variables may thus be used as engineered features for a number of machine learning tasks. With time-series forecasting models, for example, the inclusion of such physically informed features serves to enhance prediction accuracy because it grounds the learning procedure in domain knowledge. In physical anomaly detection, more or less, these variables define the baseline of the normal functioning of the system, which eases the identification of deviations or anomalies that denote the onset of faults or malfunctions. Besides, in the setting of regression that seeks to predict the temporal evolution of real-world physical systems, these features prove to be valuable inputs encapsulating time and structural relations of the system. Thus, harnessing the interpretability and physical significance of the Upadhyaya transform variables will ultimately permit building more robust and generalizable machine learning models.

Figure 3 shows an example of a damped oscillatory signal. Such patterns appear in vibrational systems and decay-based quantum transitions, and their extracted parameters (frequency, damping rate) can be used as ML features.

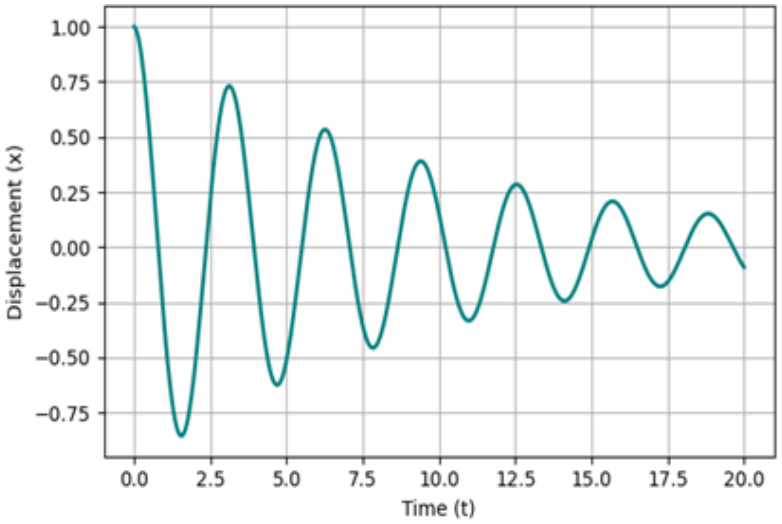

Figure 3. Damped oscillatory motion showing exponential decay in amplitude over time. Common in resistive systems or radiative decay, such curves are valuable for time-series feature engineering

5.8. Hybrid modeling and model explainability

One of the promising avenues in the area of intelligent systems is the arrangement of hybrid setups, wherein machine learning components are used to render the complicated or unknown portions of the system while well-defined physical settings are given by the Upadhyaya-transformed equations. This synergy equips both data- and physics-based approaches with their mutual strengths in one modeling architecture. An important selling point of such hybrid models is explainability-an aspect deriving from being based in physics and thereby offering a clear and interpretable structure grounded in known scientific principles. Hence, second, such models tend to be more efficient regarding data; through physical knowledge embedded into the learning process, one reduces the need for acquiring vast empirical data for training. The argument supporting hybrid models shows that they develop better generalization abilities when researchers use out-of-sample testing in their applications. The physics-based component functions as a regularizer which controls the machine-learning model's solution space to produce results that maintain physical realism. The Upadhyaya transform needs hybrid learning systems to enhance their predictive power

while improving their trustworthiness and result understanding in all scientific disciplines and engineering applications. The classical exponential decay function represented by Figure 4 can be modeled through both analytical methods and hybrid ML approaches. Research continues to explore these modeling techniques across multiple domains which include climate modeling and intelligent manufacturing systems and advanced robotics control systems. The Upadhyaya transform functions as a standard method to convert differential equations into a format which allows easier solution through analytical methods used in physics. The system generates interpretable results which maintain physical accuracy thus becoming an effective method to transfer domain expertise to machine learning systems. The figures presented in this study (Figures 1,2, 3, and 4) make it clear that these transformed representations of physical phenomena provide structured and meaningful data useful to learning systems, which can then be applied to interdisciplinary problems in engineering design, theoretical and applied physics, and material characterization. By grounding learning algorithms in the underlying physics of the system, such approaches enable enhanced generalization, improved model interpretability, and more reliable predictions in complex real-world environments.

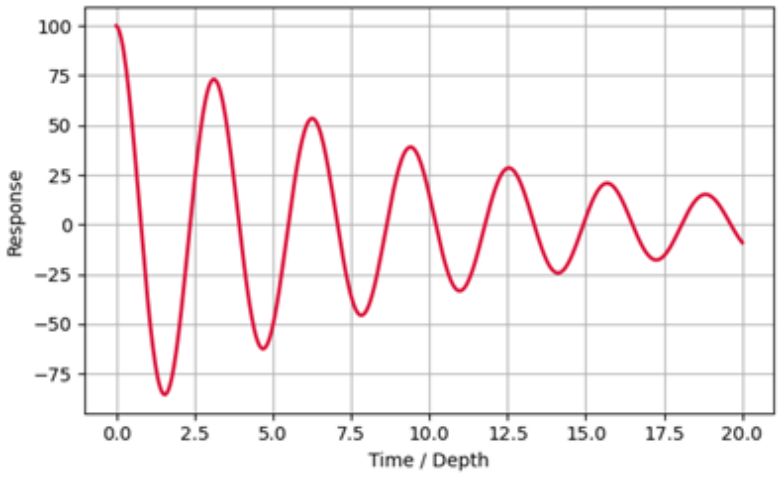

Figure 4. Exponential decay curve illustrating Lambert-Beer behavior or radiative losses. Such curves are often modeled using hybrid machine learning frameworks where the analytical shape is preserved

6. Conclusions and future research

The Upadhyaya transform, when combined with machine learning, establishes a systematic approach that uses scientific principles to solve difficult challenges in physical and chemical research. The Upadhyaya transform provides exact analytical solutions to differential equations which machine learning uses to create flexible models that can make predictions and learn from data. The hybrid models use their combined strengths to connect analytical methods with computational intelligence. The study uses three physical systems: the Atwood machine and the Beer-Lambert law and the electron motion under electromagnetic fields to show how transform-based analytical solutions enable new applications beyond traditional problem-solving methods. The solutions provide physically valid prior information, which functions as restrictions and testing criteria that operators use in learning-based processes. The system achieves better model performance through the integration process which leads to better understanding and more stable operations while increasing the ability of models to handle larger tasks.

The research presents no new integral transform or algebraic theorem yet its main achievement establishes a new function for the Upadhyaya transform. The study creates an application-driven framework which combines integral transform theory with predictive modeling and artificial intelligence by incorporating exact transform-based solutions into contemporary machine learning systems. The paradigm enables learning that maintains physical consistency while needing fewer

empirical datasets and achieving better model transparency which addresses current scientific computing challenges. The present work establishes a solid base for analytical and algorithmic development which enables hybrid transform–machine learning system building. The proposed framework enables complete reproducibility through analytical ground truth which can be used to evaluate its performance even though the study does not include large-scale numerical experiments or real-world datasets. The upcoming research will conduct comprehensive numerical testing while adding experimental findings and expanding the approach to nonlinear systems, fractional systems, and high-dimensional systems which will help to validate and broaden the proposed method's practical uses.

Acknowledgments

The authors deeply appreciate the reviewers for their helpful and constructive suggestions, which can help further improve this paper. The first author thanks to Harran University due to their support via a Postdoc position. All data that support the findings of this study are included within the article.

Funding

This research received no external funding.

Conflict of interest

There is no conflict of interest to disclose.

Author contributions

Yamini Parthiban: Data curation, Investigation, Writing – original draft, Writing – review & editing, Methodology. **Prabakaran Raghavendran:** Conceptualization, Methodology, Supervision, Validation, Formal analysis, Writing – review & editing. **Dinesh Thakur:** Formal analysis, Validation, Investigation. **Srinivasan Madhumitha:** Software, Visualization, Writing – review & editing.

Declaration of using AI tools

The authors declare that they have not used any type of generative artificial intelligence for the writing of this manuscript, nor for the creation of images, graphics, tables, or their corresponding captions.

References

[1] A. Mousa, "Application of the Upadhyaya transform to Volterra integral equations of the first kind," *Bulletin of Pure and Applied Sciences Section E: Mathematics & Statistics*, vol. 40E, no. 2, pp. 140–148, 2021. https://doi.org/10.5958/2320-3226.2021.00016.3

[2] D. Patil, "Application of integral transform (Laplace and Shehu) in chemical sciences," *SSRN*, vol. 88, pp. 437–441, 2022. https://doi.org/10.2139/ssrn.4006213

[3] S. Kulkarni and P. Mahagaonkar, "Study on motion of an electron in a physical system by using some integral transforms," *Eur. Chem. Bull.*, vol. 12, no. 8, pp. 967–974, 2023.

[4] D. Thakur and E. A. Kuffi, "Exact solutions of cardiovascular models by using Upadhyaya Transform," *Journal of Kufa for Mathematics and Computer*, vol. 11, no. 1, pp. 37–42, 2024. https://doi.org/10.31642/JoKMC/2018/110107

[5] D. Thakur, P. Raghavendran, T. Gunasekar, P. C. Thakur, B. Krishan, and S. Kumar, "Solving the chemical reaction models with the Upadhyaya Transform," *Orient. J. Chem.*, vol. 40, no. 3, pp. 767–772, 2024. https://doi.org/10.13005/ojc/400318

[6] P. Raghavendran, T. Gunasekar, D. Thakur, P. C. Thakur, and B. Krishan, "Predictive modeling of chemical processes using differential equations and machine learning synergy," *Orient. J. Chem.*, vol. 41, no. 2, pp. 386–392, 2025. https://doi.org/10.13005/ojc/410206

[7] P. Raghavendran, T. Gunasekar, and S. Gochhait, "A new approach for solving fractional differential equations incorporating Ramadan Group Transform and machine learning," *EAI Endorsed Trans IoT*, vol. 11, pp. 1–12, 2025. https://doi.org/10.4108/eetiot.7134

[8] H. Jafari, S. Aggarwal, A. Kumar, and S. Bansal, "Anuj Integral Transform to solving Abel's integral equation of classical mechanics," *Natl. Acad. Sci. Lett.*, pp. 1–5, 2025. https://doi.org/10.1007/s40009-024-01597-9

[9] P. Beeken, "Atwood's heavy chain," *Phys. Teach.*, vol. 49, no. 8, pp. 470–472, 2011. https://doi.org/10.1119/1.3651724

[10] T. B. Greenslade, Jr., "Atwood's machine," *Phys. Teach.*, vol. 29, no. 1, pp. 24–28, 1985. https://doi.org/10.1119/1.2341703

[11] G. Scholz and F. Scholz, "First-order differential equations in chemistry," *ChemTexts*, vol. 1, no. 1, p. 1, 2014. https://doi.org/10.1007/s40828-014-0001-x

[12] A. A. Mahmud, "Considerable traveling wave solutions of the generalized Hietarinta-type equation," *International Journal of Mathematics and Computer in Engineering*, vol. 3, no. 2, pp. 185–200, 2024. https://doi.org/10.2478/ijmce-2025-0015

[13] A. A. Mahmud, T. Tanriverdi, and K. A. Muhamad, "Exact traveling wave solutions for the (2+1)-dimensional Konopelchenko–Dubrovsky equation using hyperbolic trigonometric function methods," *International Journal of Mathematics and Computer in Engineering*, vol. 1, no. 1, pp. 11–24, 2023. https://doi.org/10.2478/ijmce-2023-0002

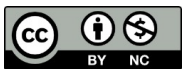

All open access articles published in Transactions on Computational Modeling and Intelligent Systems (http://tcmis.org) are distributed under the terms of the CC BY-NC 4.0 license (Creative Commons Attribution Non-Commercial 4.0 International Public License as currently displayed at http://creativecommons.org/licenses/by-nc/4.0/legalcode) which permits unrestricted use, distribution, and reproduction in any medium, for non-commercial purposes, provided the original work is properly cited.

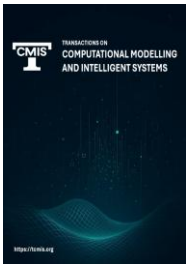

Transactions on
Computational Modeling and Intelligent Systems

Volume 4, July 2026, Article 10092
https://doi.org/10.65112/tcmis.10092

eISSN: 3108-5202
www.tcmis.org

RESEARCH ARTICLE

A machine-learning decision support system for demand-driven nurse staffing in outpatient clinics: Design and validation at an Indonesian public hospital

Muhammad Fadhillah Hadi and Asmuliardi Muluk*

Department of Industrial Engineering, Faculty of Engineering, Universitas Andalas, Padang, Indonesia.

**Corresponding Author. Email: asmuliardi@gmail.com (A. Muluk)*

Article Information

Received: 4 June 2026
Accepted: 7 July 2026
Published: 11 July 2026

AMS 2020 Classification:
62M10, 68T05, 90B90

Abstract

Public hospitals in developing countries often plan their health workforce reactively despite highly variable daily patient demand, leading to uneven workloads and longer waiting times. This study designed, verified, and retrospectively evaluated a web-based decision support system (DSS) that couples daily demand forecasting with a transparent workload-based nurse-staffing rule and automated cross-unit reallocation, using five years of outpatient records (2021–2025; 364,849 visits) from a class-B public hospital in Batam, Indonesia. ARIMA, long short-term memory (LSTM), and Prophet models were compared for the five highest-volume clinics under a single consistent protocol across three horizons—one-step-ahead, rolling-origin seven-day-ahead, and long-horizon multi-step—using MAE, RMSE, and the scale-free MASE against a seasonal-naive benchmark, with Diebold–Mariano tests for significance. ARIMA was the most reliable model: at the operational seven-day horizon it achieved a mean MASE of 0.79 and significantly outperformed the naive benchmark in four of five clinics, whereas at long horizons all models converged toward naive-level accuracy. A retrospective counterfactual simulation, in which implied nurse requirements are derived from the same workload rule used by the DSS, indicates that forecast-driven recommendations would have reduced total staffing mismatch by 55.9% under realistic seven-working-day planning (60.3% in the one-step upper bound), versus 43.2% for seasonal-naive staffing recommendations, and reveals structural misallocation across clinics, 56% of which could be covered by same-day reallocation. Sensitivity analyses over preprocessing choices, workload parameters, and weekly-lag specifications support the robustness of these findings. System computations were verified exactly, and a single-expert review by the hospital's Head of Services established face validity of the tool. The results demonstrate that an auditable forecasting-to-staffing pipeline is feasible on routine hospital data, and that evaluation protocol and forecast horizon critically shape conclusions about model superiority.

Keywords: Decision support system, demand forecasting, ARIMA, nurse staffing, healthcare operations, time-series analysis

1. Introduction

Access to quality health care depends not only on clinical capability but on how efficiently hospitals plan and allocate their human resources [1], [2]. As outpatient demand grows and fluctuates, the mismatch between available staff and actual workload directly affects waiting times, staff fatigue, and service quality [3]. Hospitals are therefore increasingly expected to support operational decisions with structured, data-driven methods rather than experience-based intuition [4].

The case institution, a class-B public hospital in Batam, Indonesia (RSUD Embung Fatimah), is the city's only municipally owned hospital and a referral centre for the surrounding region [5]. Its outpatient volume is large and uneven: daily visits vary sharply within the week, while clinic staffing is determined in a largely static, reactive

manner. Documented service complaints and long waiting times indicate an imbalance between demand and service capacity. Such variability makes fixed daily staffing inefficient: under-staffing on peak days raises waiting times and workload, while over-staffing on quiet days wastes scarce personnel.

Decision support systems (DSS) provide an established means of structuring semi-structured operational decisions by combining data, models, and interactive interfaces [6–8]. When coupled with machine learning, a DSS can learn historical demand patterns and translate them into proactive resource recommendations [9]. Patient-arrival forecasting has been studied extensively in emergency and outpatient settings [10], [11]. However, two gaps remain. First, much of this work stops at the forecasting model and is not embedded in a deployable decision tool that converts predictions into concrete staffing actions, including reallocation across units. Second, comparative forecasting studies frequently report accuracy under evaluation protocols that do not match how the model would be used in deployment, which can overstate real-world performance.

This study addresses both gaps by designing, implementing, and validating an end-to-end web DSS for nurse staffing, and by re-examining model performance under a consistent, deployment-aligned, statistically tested evaluation. The contributions are: (i) an integrated forecasting-to-staffing pipeline with transparent, auditable logic and automated cross-unit reallocation, evaluated on five years of real hospital data; (ii) a fair, horizon-aware comparison of ARIMA, LSTM, and Prophet using scale-free metrics, a seasonal-naive benchmark, and Diebold–Mariano significance tests; and (iii) a retrospective counterfactual simulation that quantifies, under deployment-aligned planning horizons and against both fixed and seasonal-naive staffing baselines, the operational value of forecast-driven staffing. Three research questions guide the work: RQ1—what are the temporal patterns of outpatient demand across the busiest clinics? RQ2—under a consistent protocol, which model best forecasts daily visits, and at which horizons? RQ3—how can forecasts be integrated into a verifiable web DSS, and what operational value does it offer?

2. Literature review

2.1. Demand forecasting in health care

Time-series forecasting is widely used to anticipate hospital demand. Classical statistical models such as ARIMA remain strong baselines for outpatient and primary-care visit forecasting [12], [13], while deep-learning approaches such as LSTM have been applied to surgical caseloads and related volumes [14]. Recent work emphasises feature-aware and probabilistic forecasting of emergency arrivals to support capacity planning [10], [11]. Comparative reviews report that no single model family dominates across datasets, with classical models remaining competitive in a substantial share of applications, particularly on univariate series with limited data [15]. Cross-domain comparisons of ARIMA, LSTM, and Prophet similarly reach context-dependent conclusions [16–18].

2.2. Forecast evaluation and staffing methods

Prophet is an additive model designed for business time series with strong seasonality and holiday effects [19]; unlike ARIMA and LSTM it is not autoregressive, a property that materially affects how it should be evaluated. LSTM networks capture nonlinear temporal dependencies through gated recurrent units [20–22]. Sound evaluation requires metrics appropriate to the data: percentage errors such as MAPE are unstable when actual values are small, motivating scale-free alternatives such as MASE [23], [24], and formal comparison of predictive accuracy is enabled by the Diebold–Mariano test [25]. On the operations side, the Workload Indicators of Staffing Need (WISN) method links staffing requirements to measured workload and is used in Indonesian health facilities [26], [27]. Reviews of health information systems note that decision support remains under-integrated into routine workforce planning [28], [29]. The present study connects these strands by embedding a rigorously evaluated forecaster into a WISN-inspired, auditable DSS and quantifying its operational value.

3. Methodology

3.1. Study site and data

Routine outpatient registration records of RSUD Embung Fatimah covering January 2021–December 2025 were used, comprising 364,849 visits. The unit of analysis is the daily visit count per clinic. The five highest-volume clinics were analysed: Internal Medicine, Medical Rehabilitation, Cardiology, Pulmonology, and General/MCU (Table 1). Only the visit date and clinic fields were extracted from the registration system and aggregated to anonymous daily counts per clinic before analysis; no patient-identifying information was accessed, and no personal data left the hospital environment. The study received ethical approval from the Health Research Ethics Committee of RSUD Embung Fatimah, Batam (approval no. 0498/500.10.30.8/II/2026, dated 18 February 2026), and institutional permission for research and data collection was granted by the Director of RSUD Embung Fatimah (letter no. 4710/800.2.1.2/XI/2025, dated 28 November 2025), following a formal request from Universitas Andalas (letter no. B/1191/UN16.9.5.3/PK.01.06/2025).

Table 1. Outpatient dataset summary (2021–2025).

Clinic	Records	Modelled daily obs.	Existing nurses
Internal Medicine	64,004	1,202	3
Medical Rehabilitation	37,235	1,191	6
Cardiology	34,934	1,158	2
Pulmonology	25,587	1,167	2
General / MCU	24,128	778	3

3.2. Pre-processing and series characterisation

Records were aggregated to daily counts per clinic. Saturdays, Sundays, and Indonesian national holidays were excluded because the clinics operate on weekdays, and low-activity days (count ≤ 5) were removed, consistent with the original study design. The scale of these exclusions and their consequences are quantified in Table 8: weekend and holiday activity is negligible in four of the five clinics, and the low-activity rule removes only 0.5–1.7% of working days in four clinics, but 33.6% in General/MCU, whose walk-in medical check-up demand is intermittent; a robustness check retaining low-activity days is reported alongside. Each series was split 80/20 chronologically into training and test segments. Before modelling, each series was characterised using augmented Dickey–Fuller (ADF) and KPSS stationarity tests and STL decomposition [30], from which trend and seasonal strengths were computed (Table 2). Three of five series are non-stationary in level, supporting first differencing. The 2021 pandemic period constitutes a regime shift: mean daily visits in 2021 were 21–87% below the 2022–2025 average, so part of the apparent long-term growth reflects post-COVID recovery rather than organic demand growth.

Table 2. Series characteristics per clinic (training period).

Clinic	Mean/day	CV	ADF p	KPSS p	Trend str.	Seasonal str.
Internal Medicine	53.2	0.39	0.271	0.01	0.58	0.29
Medical Rehabilitation	31.2	0.33	0.262	0.01	0.79	0.38
Cardiology	30.1	0.50	0.479	0.01	0.55	0.18
Pulmonology	21.9	0.38	0.011	0.01	0.30	0.26
General / MCU	28.9	1.45	0.000	0.10	0.59	0.00

3.3. Forecasting models and model selection

Three models were implemented. ARIMA used order (7,1,1), reflecting a weekly autoregressive structure with first differencing. To verify this specification, a per-clinic order search over $p \in \{0,1,2,3,5,7\}$, $q \in \{0,1,2\}$ with d set by the ADF test was conducted using the Akaike information criterion, and residuals of the selected models were tested with the Ljung–Box statistic (Table 3). The search selected (7,1,1) for Internal Medicine, and the near-equivalent (7,1,2) for Medical Rehabilitation and Cardiology ($\Delta AIC \leq 3.5$ relative to (7,1,1)), all with white-noise residuals. For the two series classified as level-stationary by the ADF test, Pulmonology and General/MCU, the best specification within $d = 0$ was (5,0,2); because AIC values are not comparable across different orders of differencing, the competing specifications were additionally compared out of sample under the rolling seven-day protocol (Table 9), where the largest MASE difference in any clinic is 0.04. Under (7,1,1), residual autocorrelation remained for Pulmonology (Ljung–Box $p < 0.05$), which is acknowledged as a limitation. The seven-lag autoregressive window was retained—although the working-day series has a five-day week—because it nests the five-day weekly lag on the consecutive working-day index and matches the deployed system's specification; the seven-day LSTM input window follows the same convention, and Table 9 confirms that five-lag and seasonal ($m = 5$) alternatives do not change the conclusions. LSTM used a 7-day input window, one 50-unit LSTM layer (ReLU) and a dense output, trained for 20 epochs (Adam, MSE) on min–max-scaled inputs with the scaler fitted on training data only. Prophet used additive weekly and yearly seasonality with Indonesian holidays [19].

Table 3. ARIMA order selection and residual diagnostics.

Clinic	Selected order (AIC)	AIC	(7,1,1) AIC	Ljung–Box p	White residuals
Internal Medicine	(7,1,1)	7931.9	7931.9	0.535	yes
Medical Rehabilitation	(7,1,2)	6207.9	6211.4	0.936	yes
Cardiology	(7,1,2)	7068.3	7069.2	0.463	yes
Pulmonology	(5,0,2)	6497.4	6477.9	0.000	no
General / MCU	(5,0,2)	5682.5	5710.7	0.065	yes (marginal)

3.4. Evaluation protocol

All models were evaluated under one identical protocol, reported for three horizons that bracket realistic deployment. (a) One-step-ahead: each model predicts day t given all actual data up to t−1, reflecting a DSS re-run daily as new counts arrive. (b) Rolling-origin seven-day-ahead: from 17 forecast origins spaced 14 days apart across the test segment, each model forecasts the next 7 working days using parameters estimated on the training segment and data observed up to the origin; this reflects weekly staff planning [23]. Throughout, "seven-day" denotes seven consecutive working days (≈1.4 calendar weeks) on the working-day index. (c) Long-horizon multi-step: a single fit on the training segment forecasting the entire test segment. This design corrects a protocol inconsistency in which autoregressive models (ARIMA, LSTM) would receive one-step information while the non-autoregressive Prophet would not. Accuracy was measured by MAE, Eq. (1); RMSE, Eq. (2); MAPE, Eq. (3); and the scale-free MASE, Eq. (4), computed against a seasonal-naive benchmark with period m = 5 working days. MASE below 1 indicates accuracy better than seasonal-naive. Differences from ARIMA were tested with the Diebold–Mariano statistic with the Harvey small-sample correction [25].

$$\mathrm{MAE} = (1/n)\ \Sigma\ |y_t - \hat{y}_t| \tag{1}$$

$$\mathrm{RMSE} = [\ (1/n)\ \Sigma\ (y_t - \hat{y}_t)^2\ ]^{1/2} \tag{2}$$

$$\mathrm{MAPE} = (100\%/n)\ \Sigma\ |(y_t - \hat{y}_t)/y_t| \tag{3}$$

$$\mathrm{MASE} = \mathrm{MAE} / [\ (1/(N-m))\ \Sigma\ |y_i - y_{i-m}|\ ] \tag{4}$$

3.5. Workload-based staffing rule

Forecasts are converted into nurse requirements using a transparent, WISN-inspired rule. For predicted daily volume A, total standard activity time per patient T_s (minutes) and effective working time per shift T_e (minutes), the required number of nurses is given by Eq. (5). This is a simplified workload-to-capacity ratio derived from WISN principles rather than a full WISN computation. Of the WISN components, the rule retains the activity (service) standard—the measured time per patient for the direct nursing tasks of an outpatient encounter—and the effective working time per shift; it omits WISN's annual available-working-time calculation (leave, absence, training), the category and individual allowance standards for non-patient activities, and the annual standard-workload aggregation, because the DSS makes a daily, per-clinic decision for which these annualised components act as approximately constant scaling factors. The simplification is stated explicitly as a limitation, and a sensitivity analysis over T_s and T_e is reported with the results. Default parameters elicited from the hospital in the underlying operational study are T_s = 35 minutes (initial assessment 10, nursing documentation 15, physician support 10) and T_e = 420 minutes of effective time per shift; both are user-adjustable in the DSS.

$$N = \lceil\ (A \times T_s) / T_e\ \rceil \tag{5}$$

3.6. DSS architecture

The DSS was implemented as an interactive web application (Streamlit). Per-clinic models are trained offline and serialised; at run time the application generates the daily forecast, applies Eq. (5) with user-adjustable activity times and shift length, and displays recommended versus existing staffing with a gap indicator. When a clinic shows a deficit, the system scans the remaining clinics for a same-day surplus and proposes a cross-unit reallocation. Reallocation proposals are advisory: they indicate where a same-day surplus exists but do not yet encode nurse skill compatibility, per-clinic minimum-staffing floors, or transfer feasibility, which remain

managerial checks before any transfer is executed. Figure 1 summarises the research methodology and Figure 2 the system architecture.

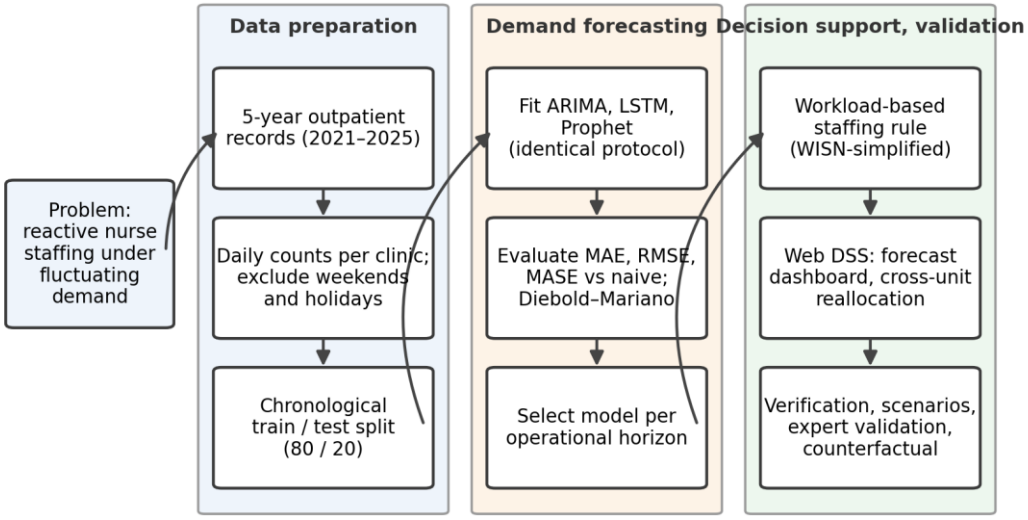
Data preparation
Demand forecasting
Decision support, validation
Problem: reactive nurse staffing under fluctuating demand
5-year outpatient records (2021–2025)
Daily counts per clinic; exclude weekends and holidays
Chronological train / test split (80 / 20)
Fit ARIMA, LSTM, Prophet (identical protocol)
Evaluate MAE, RMSE, MASE vs naive; Diebold–Mariano
Select model per operational horizon
Workload-based staffing rule (WISN-simplified)
Web DSS: forecast dashboard, cross-unit reallocation
Verification, scenarios, expert validation, counterfactual

Figure 1. Research methodology flowchart.

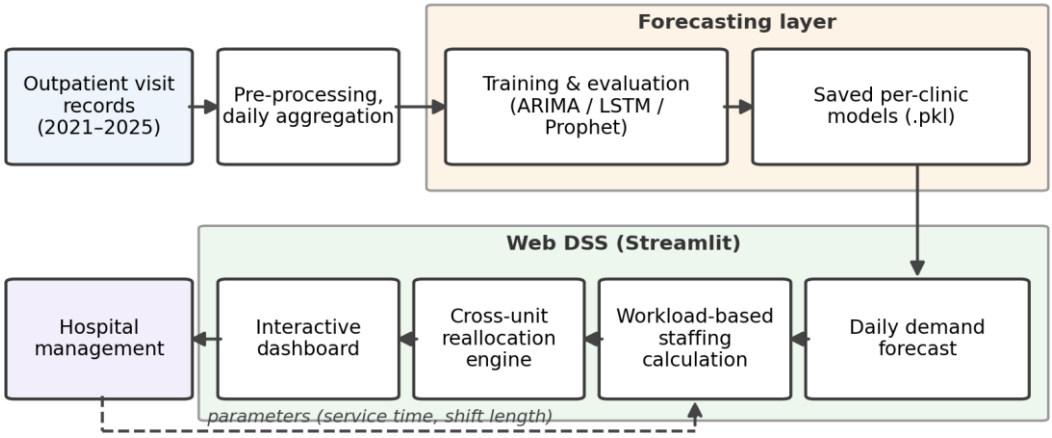

Figure 2. DSS system architecture.

3.7. Verification, validation, and counterfactual evaluation

Four complementary checks were designed: (i) computational verification, comparing system output against manual calculations of Eq. (5); (ii) functional scenario testing covering prediction, holiday handling, gap analysis, and reallocation; (iii) single-expert face validation with the hospital's Head of Services; and (iv) a retrospective counterfactual simulation of operational value. In the simulation, the daily nurse requirement implied by actual demand, $N^a = \lceil(\text{actual} \times T_s)/T_e\rceil$, is compared over the test period against alternative staffing policies, with mismatch measured in nurse-days as $\Sigma|N(\text{policy}) - N^a|$. Four policies are evaluated: the hospital's current fixed allocation; DSS recommendations in one-step mode, an information-rich upper bound corresponding to a system re-run each day for the next day; DSS recommendations under rolling seven-working-day planning, in which forecasts for the coming week are generated at weekly origins from data observed up to each origin with parameters estimated on the training segment—the horizon at which rosters are realistically fixed; and staffing recommendations derived from seasonal-naive forecasts under the same weekly protocol, as the appropriate naive benchmark. The implied requirement is a workload-rule proxy for need rather than an observed outcome such as waiting time or overtime; the analysis is therefore a simulation of operational value, not operational validation, and is labelled accordingly throughout.

4. Experimental tests and results

4.1. Demand patterns and series characteristics (RQ1)

Aggregate visits show a fluctuating, gradually rising trajectory over 2021–2025 (Figure 3), part of which reflects post-pandemic recovery (Section 3.2). At the operational scale a consistent weekly seasonality dominates: demand peaks on Monday and declines toward Friday in every clinic (Figure 4); for Internal Medicine, mean daily visits fall from 63.9 (Monday) to 40.3 (Friday). STL decomposition of the Internal Medicine series (Figure 5) confirms a marked trend component and a stable weekly seasonal component. General/MCU is an outlier: with a coefficient of variation of 1.45 and seasonal strength of 0.00 (Table 2), it is intrinsically hard to forecast, which anticipates the model results below.

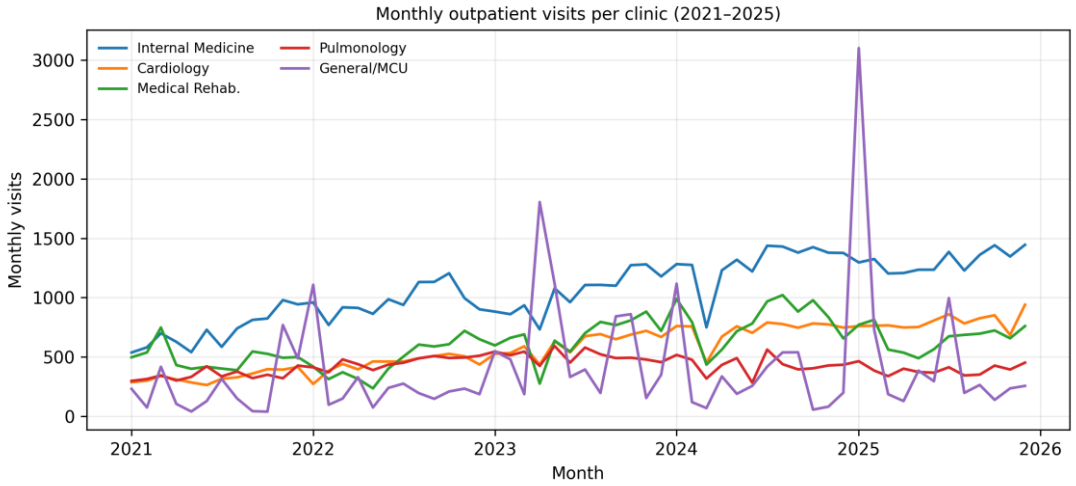

Figure 3. Monthly outpatient visits per clinic, 2021–2025.

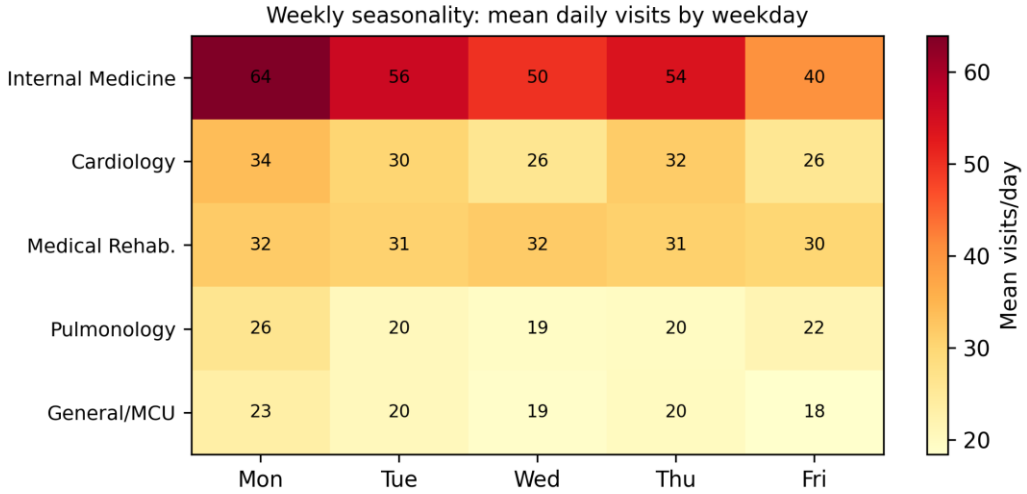

Figure 4. Weekly seasonality: mean daily visits by weekday and clinic.

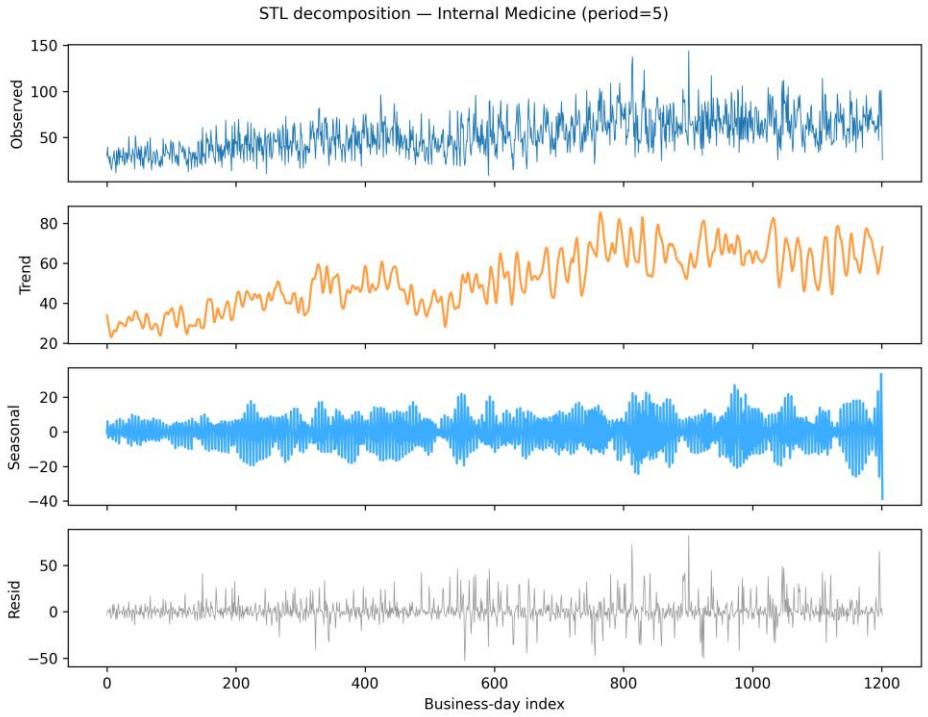

Figure 5. STL decomposition of the Internal Medicine series (period = 5 working days).

4.2. Forecasting accuracy across horizons (RQ2)

Table 4 reports accuracy averaged over the five clinics for the three horizons, and Figure 6 visualises the one-step versus long-horizon contrast. Three findings stand out. First, under one-step forecasting ARIMA is the most accurate model (MAE 9.8, MASE 0.75). Second, at the operational seven-day rolling horizon ARIMA remains the most reliable model (mean MASE 0.79): it attains MASE below 1 in every clinic and outperforms the seasonal-naive benchmark significantly in four of five clinics (Diebold–Mariano $p < 0.01$; Table 5, Figure 7), while never being significantly worse than any competitor. LSTM is competitive (mean MASE 0.85) and marginally—but not significantly—better than ARIMA in the two most irregular series. Prophet is unreliable (MASE 2.17 in Medical Rehabilitation and 1.27 in General/MCU); because it is not autoregressive its accuracy is identical across horizons, which also explains why protocols granting autoregressive models one-step information would disadvantage it. Third, at the long multi-step horizon all models converge (MAE ≈ 15) and perform only marginally better than—and for General/MCU not significantly different from—seasonal-naive (MASE 1.1–1.2). MAPE proved unstable (inflated by low-count days, exceeding 80% on average at the long horizon) and is therefore not used as a primary criterion [24].

Table 4. Forecasting accuracy by model and horizon (mean over five clinics; MAE / MASE).

Horizon	ARIMA	LSTM	Prophet	Seasonal-naive
One-step (daily update)	9.8 / 0.75	10.3 / 0.79	15.3 / 1.23	13.8 / 1.04
Rolling origin, h = 7	10.6 / 0.79	11.4 / 0.85	15.4 / 1.21	13.3 / 1.03
Long-horizon multi-step	15.2 / 1.13	15.0 / 1.16	15.3 / 1.23	16.9 / 1.37

Table 5. Rolling-origin seven-day-ahead MASE per clinic and Diebold–Mariano p-values (reference: ARIMA).

Clinic	ARIMA	LSTM	Prophet	Naive	p vs LSTM	p vs Prophet	p vs Naive
Internal Medicine	0.86	1.02	0.95	1.13	0.041	0.477	0.005
Medical Rehabilitation	0.71	0.76	2.17	0.91	0.431	0.000	0.003
Cardiology	0.95	1.11	0.96	1.30	0.041	0.635	0.000
Pulmonology	0.72	0.70	0.72	1.02	0.399	0.878	0.001
General / MCU	0.72	0.68	1.27	0.78	0.280	0.001	0.609

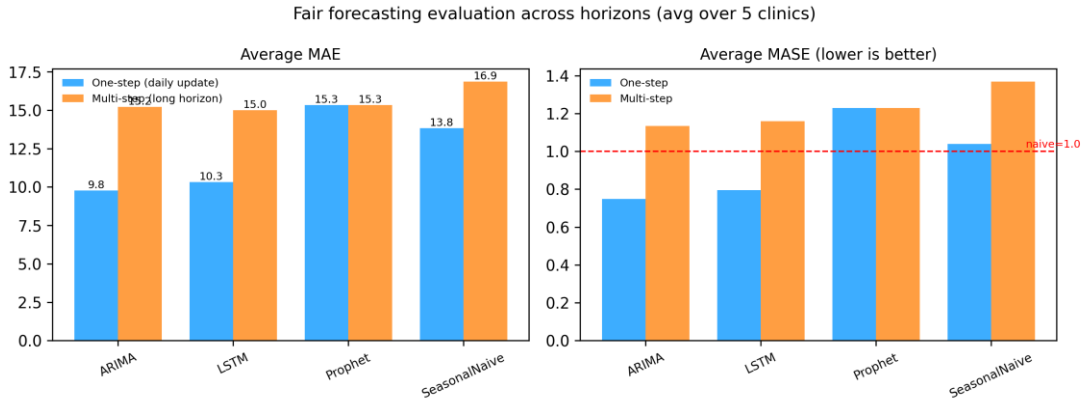

Figure 6. Fair evaluation across horizons: average MAE and MASE per model (naive reference at MASE = 1).

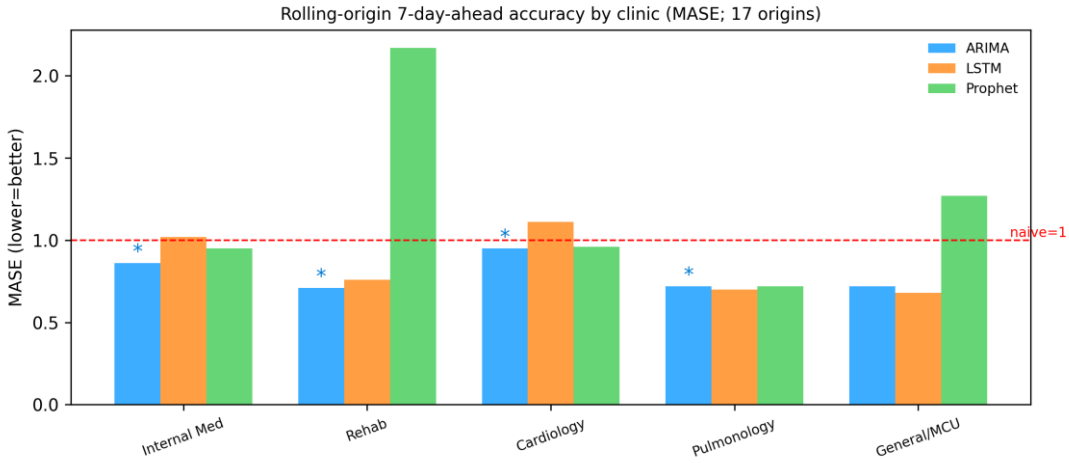

Figure 7. Rolling-origin seven-day-ahead MASE by clinic; * marks clinics where ARIMA is significantly better than seasonal-naive (DM $p < 0.05$).

4.3. Operational value: counterfactual staffing evaluation (RQ3)

Table 6 and Figure 8 compare staffing mismatch against implied need over the test period. All figures are outputs of the retrospective counterfactual simulation defined in the methodology, not observed operational outcomes. Under the current fixed allocation the five clinics accumulate 2,132 nurse-days of mismatch. Forecast-driven DSS recommendations reduce this to 941 nurse-days (a 55.9% reduction) under realistic rolling seven-working-day planning, and to 846 nurse-days (60.3%) in the one-step upper bound; staffing driven by seasonal-naive forecasts under the same weekly protocol attains 1,211 nurse-days (43.2%). At the horizon at which rosters are actually planned, the forecast-driven policy therefore retains a 12.7-percentage-point advantage over the naive staffing benchmark. The simulation also reveals structural misallocation that no daily rule can fix alone: Medical Rehabilitation (6 nurses) is over-staffed on 239 of 239 test days, while Internal Medicine (3 nurses) is under-staffed

on 232 of 241 days. This is precisely the situation the DSS's reallocation engine targets: summing across clinics, 56% of all deficit nurse-days could be covered by a same-day surplus elsewhere. The evaluation is honest about heterogeneity: in Pulmonology, where fixed staffing already matches need closely, forecast noise makes the DSS marginally worse (+5.6% mismatch at the weekly horizon), and in the intermittent General/MCU series the weekly-horizon gain shrinks to 2.3% (26.9% one-step); forecast-driven staffing adds most value where demand is volatile relative to current allocation, and least where demand is intermittent.

Table 6. Retrospective counterfactual staffing mismatch over the test period (nurse-days), by staffing policy; percentage change is relative to fixed staffing.

Clinic	Fixed staffing	DSS one-step	DSS 7-day	Seasonal-naive 7-day	Change (DSS 7-day)
Internal Medicine (3)	704 (under-staffed 232/241 days)	278	288	388	−59%
Medical Rehabilitation (6)	651 (over-staffed 239/239 days)	66	73	93	−89%
Cardiology (2)	424	215	228	304	−46%
Pulmonology (2)	89	94	94	144	+6%
General / MCU (3)	264	193	258	282	−2%
Total	2,132	846	941	1,211	−55.9%

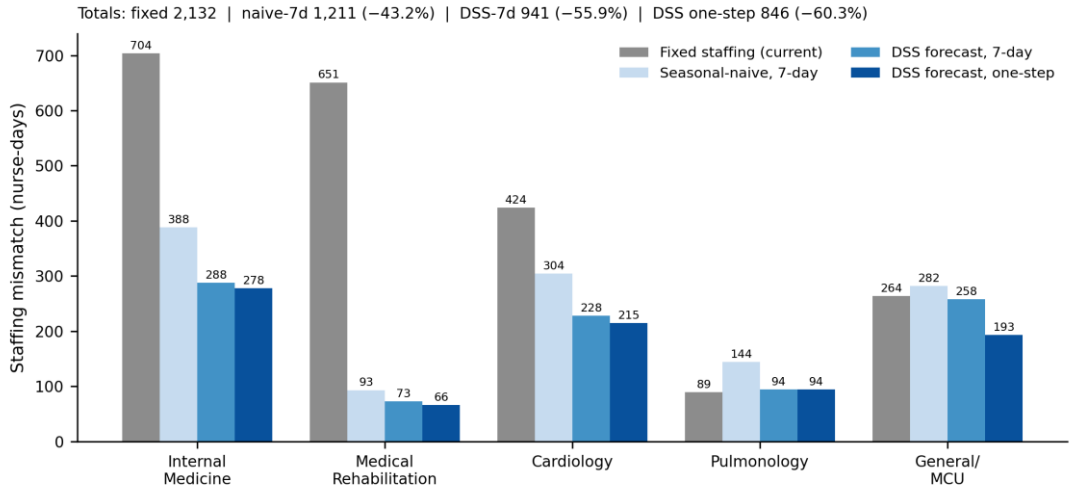

Figure 8. Retrospective counterfactual simulation: staffing mismatch versus implied need under fixed staffing, forecast-driven DSS (one-step and seven-day modes), and seasonal-naive staffing.

4.4. Sensitivity and robustness analyses

Three analyses probe the robustness of the reported results. First, preprocessing: Table 8 quantifies the excluded observations per clinic. Weekend and holiday rows are rare because the clinics operate on weekdays; the exception is General/MCU, whose occasional Saturday check-up sessions account for 419 visits on 8 weekend days over five years. The low-activity rule (count ≤ 5) removes only 0.5–1.7% of working days in four clinics but 33.6% in General/MCU. Re-running the rolling seven-day evaluation with low-activity days retained leaves ARIMA more accurate than the concurrent seasonal-naive benchmark in all five clinics, and accuracy is materially affected only in General/MCU (ARIMA MASE 0.72 → 1.33; naive 0.78 → 1.75), whose series becomes strongly intermittent; in Medical Rehabilitation the degradation is moderate (0.71 → 0.86) and elsewhere it is negligible. The exclusion therefore biases neither the model ranking nor the conclusions for the four regular clinics, but forecasts—and staffing values derived from them—for General/MCU should be read with caution.

Second, workload parameters: varying T_s over 25–45 minutes and T_e over 390–450 minutes changes the seven-day DSS mismatch reduction from 52.1% to 61.3% (55.9% at the default (35, 420)). The qualitative conclusion—

forecast-driven staffing removes roughly half or more of the mismatch—is insensitive to the WISN simplification within this range, although the absolute nurse-day figures scale with the assumed activity time.

Third, the weekly-lag specification: Table 9 compares ARIMA(7,1,1) with five-lag and seasonal five-day alternatives under the rolling seven-day protocol. The largest MASE difference in any clinic is 0.04, confirming that the seven- versus five-lag choice is immaterial out of sample and that the conclusions do not depend on this specification.

Table 8. Preprocessing sensitivity: working days per clinic, observations removed by the low-activity rule (count ≤ 5), and rolling seven-day accuracy with the rule applied (filtered) versus retained (all); MASE is computed within each preprocessing variant.

Clinic	Working days	Removed by count ≤ 5 (%)	ARIMA MASE (filtered → all)	Naive MASE (filtered → all)
Internal Medicine	1,209	7 (0.6%)	0.86 → 0.84	1.13 → 1.11
Medical Rehabilitation	1,197	6 (0.5%)	0.71 → 0.86	0.91 → 1.17
Cardiology	1,178	20 (1.7%)	0.95 → 0.96	1.30 → 1.31
Pulmonology	1,187	20 (1.7%)	0.72 → 0.75	1.02 → 0.92
General / MCU	1,172	394 (33.6%)	0.72 → 1.33	0.78 → 1.75

Table 9. Weekly-lag specification sensitivity: rolling-origin seven-day MASE by clinic.

Clinic	ARIMA (7,1,1)	ARIMA (5,1,1)	ARIMA (5,1,2)	SARIMA $(1,1,1)(1,0,1)_5$
Internal Medicine	0.86	0.90	0.89	0.91
Medical Rehabilitation	0.71	0.71	0.71	0.70
Cardiology	0.95	0.95	0.95	0.98
Pulmonology	0.72	0.70	0.70	0.69
General / MCU	0.72	0.73	0.74	0.73

4.5. System verification and expert face validation

Computational verification reproduced manual results exactly: for Cardiology with a predicted volume of 44 patients, Eq. (5) yields $\lceil(44 \times 35)/420\rceil = 4$ nurses, identical to the system output. Functional testing confirmed correct behaviour in all five scenarios (Table 7). In expert validation, the hospital's Head of Services judged the dashboard outputs clear, the staffing logic transparent, and the recommendations relevant to daily operations. Because this involved a single domain expert, it establishes face validity rather than broad user acceptance; a multi-user usability study is identified as future work.

Table 7. Functional scenario testing.

Function	**Scenario**	**Expected result**	**Status**
Patient prediction	Select working day	Forecast displayed	Pass
Holiday detection	Select weekend/holiday	"Unit closed", zero patients	Pass
Requirement calculation	Enter service times	Nurses computed via Eq. (5)	Pass
Gap analysis	Need exceeds existing	Deficit indicator raised	Pass
Reallocation	Surplus available elsewhere	Transfer suggestion shown	Pass

4.6. Discussion

The results carry a clear methodological message: conclusions about model superiority depend on the evaluation protocol and the forecast horizon. A single headline number (e.g., MAE ≈ 9.8 for ARIMA) without a stated horizon overstates what a planner experiences when forecasting a week or more ahead. For this application the operationally relevant result is the rolling seven-day evaluation, where ARIMA is accurate, statistically better than naive in four of five clinics, computationally light, and interpretable—making it a defensible default for a daily-updated DSS. The convergence of all models toward naive-level accuracy at long horizons, and the failure of all models to beat naive significantly in the structurally irregular General/MCU clinic, are honest boundaries of applicability that managers should know. The counterfactual simulation reframes the contribution: beyond forecast accuracy, the DSS's simulated value lies in correcting a structural misallocation (a chronically over-staffed unit coexisting with a chronically under-staffed one) and in enabling same-day reallocation that could absorb 56% of deficits. Importantly, most of the simulated benefit survives the move from one-step to realistic weekly planning (60.3% to 55.9%), and the forecast-driven policy continues to dominate the seasonal-naive staffing benchmark (43.2%) at the planning horizon. Limitations include: a single hospital and five clinics; exogenous drivers (outbreaks, policy and referral changes) not modelled; a simplified WISN ratio as the need proxy, so mismatch is measured against a modelled rather than observed requirement; clinic-invariant service times (T_s), although workload intensity plausibly differs across outpatient specialties—the T_s/T_e sensitivity analysis only partially mitigates this; exclusion of low-activity days, which is consequential for the intermittent General/MCU series; reallocation logic that does not yet encode nurse skill compatibility, minimum-staffing floors, or transfer feasibility; lightly tuned LSTM; rolling-origin evaluation with fixed parameters; single-expert face validation rather than a multi-user usability study; and a counterfactual that simulates rather than observes operational outcomes such as waiting times, overtime, or service quality.

5. Conclusions and future research

This study designed, verified, and retrospectively evaluated a web-based DSS that converts five years of routine outpatient records into demand-driven nurse-staffing recommendations for an Indonesian public hospital. Outpatient demand exhibits strong weekly seasonality with a Monday peak, a post-pandemic recovery trend, and one structurally irregular clinic (RQ1). Under a consistent, multi-horizon, significance-tested evaluation, ARIMA is the most reliable forecaster at operational horizons (rolling seven-day MASE 0.79; significantly better than seasonal-naive in four of five clinics), while all models converge to naive-level accuracy at long horizons (RQ2). Integrated with a transparent workload rule and reallocation logic, the forecast-driven DSS would—in a retrospective counterfactual simulation—reduce staffing mismatch by 55.9% relative to the current fixed allocation under realistic weekly planning (60.3% in the one-step upper bound, versus 43.2% for seasonal-naive staffing), and exposes structural misallocation, with 56% of deficits coverable by same-day reallocation; its computations were verified exactly and a single-expert review established face validity (RQ3). Future research will incorporate exogenous regressors and full WISN parameters, probabilistic forecasts with service-level staffing, constraint-aware reallocation (nurse skill compatibility, minimum-staffing floors, transfer feasibility), automatic per-series model selection and tuning, integration with the hospital information system, multi-user usability evaluation, prospective evaluation against observed waiting-time and workload outcomes, and shift-level scheduling optimisation.

Acknowledgments

None.

Funding

This research received no external funding.

Conflict of interest

There is no conflict of interest to disclose.

Author contributions

M. F. Hadi: Conceptualization, data curation, software, investigation, formal analysis, writing - original draft. **A. Muluk:** Conceptualization, methodology, supervision, validation, writing - review and editing.

Declaration of using AI tools

The authors used an AI assistant to support English drafting and editing and to reproduce data figures from the authors' own data; all analyses, content, and conclusions were verified by and are the responsibility of the authors. No generative-AI-created imagery was used; data charts were generated from source data and diagrams were author-designed.

Ethics approval and institutional permission

The study was approved by the Health Research Ethics Committee of RSUD Embung Fatimah, Kota Batam, Indonesia (approval no. 0498/500.10.30.8/II/2026, dated 18 February 2026). Institutional permission for research and data collection was granted by the Director of RSUD Embung Fatimah (letter no. 4710/800.2.1.2/XI/2025, dated 28 November 2025), following the formal request of the Department of Industrial Engineering, Universitas Andalas (letter no. B/1191/UN16.9.5.3/PK.01.06/2025). The study used routinely collected registration records; only visit dates and clinic identifiers were processed, records were aggregated to anonymous daily counts per clinic, and no patient-identifying information was accessed or stored.

Data and code availability

The patient-level registration data cannot be shared publicly. The anonymised aggregate daily visit counts per clinic (date, clinic, count) that support all analyses, together with the full analysis code (data preparation, model estimation, rolling-origin evaluation, counterfactual simulation, and sensitivity analyses; Python 3 with statsmodels, Prophet, and TensorFlow, fixed random seed), are available from the corresponding author upon reasonable request.

References

[1] W. D. Savira and W. Subadi, "Kualitas pelayanan kesehatan dilihat dari aspek tangible dalam rangka meningkatkan pelayanan kesehatan pada Puskesmas Hikun," *Jurnal Administrasi Publik dan Administrasi Bisnis*, vol. 6, no. 2, pp. 749–762, 2023.

[2] Badan Pusat Statistik, Profil Statistik Kesehatan 2025. Jakarta, Indonesia: Badan Pusat Statistik, 2025.

[3] R. Amran, A. Apriyani, and N. P. Dewi, "Peran penting kelengkapan rekam medik di rumah sakit," *Baiturrahmah Medical Journal*, vol. 1, no. 1, pp. 69–76, 2021.

[4] A. Komashie, S. Hinrichs-Krapels, and P. J. Clarkson, "Systems approaches to healthcare systems design and care delivery: an overview of the literature," *Proceedings of the Design Society*, vol. 1, pp. 2941–2950, 2021, doi: 10.1017/pds.2021.555.

[5] Peraturan Wali Kota Batam No. 140 Tahun 2024 tentang Rumah Sakit Umum Daerah Embung Fatimah, 2024.

[6] A. Sebaa, A. Nouicer, A. Tari, R. Tarik, and O. Abdellah, "Decision support system for health care resources allocation," *Electronic Physician*, vol. 9, no. 6, pp. 4661–4668, 2017, doi: 10.19082/4661.

[7] D. J. Power, *Decision Support Systems: Concepts and Resources for Managers*. Westport, CT, USA: Quorum Books, 2002.

[8] E. Turban, J. E. Aronson, and T. P. Liang, *Decision Support Systems and Intelligent Systems*, 7th ed. New Delhi, India: Prentice-Hall, 2007.

[9] A. Aditya et al., *Machine Learning*. Padang, Indonesia: PT Global Eksekutif Teknologi, 2023.

[10] B. M. Porto and F. S. Fogliatto, "Enhanced forecasting of emergency department patient arrivals using feature engineering approach and machine learning," *BMC Medical Informatics and Decision Making*, vol. 24, no. 1, Art. no. 377, 2024, doi: 10.1186/s12911-024-02788-6.

[11] B. Rostami-Tabar, J. Browell, and I. Svetunkov, "Probabilistic forecasting of hourly emergency department arrivals," *Health Systems*, vol. 13, no. 2, pp. 133–149, 2024, doi: 10.1080/20476965.2023.2200526.

[12] I. Basri K., "Peramalan jumlah kunjungan pasien rawat jalan menggunakan metode ARIMA, SES dan Holt-Winters di Balai Kesehatan Masyarakat XYZ," *Jurnal Tata Kelola dan Kerangka Kerja Teknologi Informasi*, vol. 7, no. 1, pp. 29–39, 2021, doi: 10.34010/jtk3ti.v7i1.5548.

[13] N. Manabung, C. Mongi, and Y. Langi, "Peramalan banyaknya pasien yang berobat di Puskesmas Bengkol dengan menggunakan metode ARIMA," *Jurnal LPPM Bidang Sains dan Teknologi*, vol. 9, no. 1, pp. 11–19, 2024.

[14] H. Bui, S. D. Ekşioğlu, A. A. Villafranca, J. A. Sanford, and K. W. Sexton, "A long short-term memory model for forecasting the surgical case volumes at a hospital," *IISE Transactions on Healthcare Systems Engineering*, vol. 13, no. 3, pp. 226–236, 2023.

[15] V. I. Kontopoulou, A. D. Panagopoulos, I. Kakkos, and G. K. Matsopoulos, "A review of ARIMA vs. machine learning approaches for time series forecasting in data driven networks," *Future Internet*, vol. 15, no. 8, Art. no. 255, 2023, doi: 10.3390/fi15080255.

[16] I. G. T. Suryawan, I. K. N. Putra, P. M. Meliana, and I. G. I. Sudipa, "Performance comparison of ARIMA, LSTM, and Prophet methods in sales forecasting," *Sinkron: Jurnal dan Penelitian Teknik Informatika*, vol. 8, no. 4, pp. 2410–2421, 2024, doi: 10.33395/sinkron.v8i4.14057.

[17] S. Albahli, "LSTM vs. Prophet: achieving superior accuracy in dynamic electricity demand forecasting," *Energies*, vol. 18, no. 2, Art. no. 278, 2025, doi: 10.3390/en18020278.

[18] R. Anwar and L. Rassiyanti, "Analisis komparasi model peramalan Prophet dan ARIMA dalam memprediksi harga saham penutupan PT ANTM," *Lattice Journal: Journal of Mathematics Education and Applied*, vol. 5, no. 1, pp. 57–74, 2025.

[19] S. J. Taylor and B. Letham, "Forecasting at scale," *The American Statistician*, vol. 72, no. 1, pp. 37–45, 2018, doi: 10.1080/00031305.2017.1380080.

[20] T. Fischer and C. Krauss, "Deep learning with long short-term memory networks for financial market predictions," *European Journal of Operational Research*, vol. 270, no. 2, pp. 654–669, 2018, doi: 10.1016/j.ejor.2017.11.054.
[21] I. Goodfellow, Y. Bengio, and A. Courville, *Deep Learning*. Cambridge, MA, USA: MIT Press, 2016.
[22] A. Graves, *Supervised Sequence Labelling with Recurrent Neural Networks*. Berlin, Germany: Springer, 2012.
[23] R. J. Hyndman and G. Athanasopoulos, *Forecasting: Principles and Practice*, 2nd ed. Melbourne, Australia: OTexts, 2018.
[24] S. Kim and H. Kim, "A new metric of absolute percentage error for intermittent demand forecasts," *International Journal of Forecasting*, vol. 32, no. 3, pp. 669–679, 2016, doi: 10.1016/j.ijforecast.2015.12.003.
[25] F. X. Diebold and R. S. Mariano, "Comparing predictive accuracy," *Journal of Business & Economic Statistics*, vol. 13, no. 3, pp. 253–263, 1995, doi: 10.1080/07350015.1995.10524599.
[26] A. D. Wahuningtyas, R. B. M. T. Pangestu, R. P. Hariono, F. Falah, O. M. Prawiryanto, and D. W. Sutha, "Analisis kebutuhan tenaga kerja berdasarkan beban kerja dengan metode Workload Indicator of Staffing Need (WISN) unit rekam medis di Puskesmas 'X'," *MEJORA: Medical Journal Awatara*, vol. 2, no. 1, pp. 25–31, 2024, doi: 10.61434/mejora.v2i1.142.
[27] J. Natassa, N. Maimun, H. M. Ulfa, S. Wardani, and R. Isnani, "Analisis kebutuhan tenaga rekam medis menggunakan metode WISN," *Jurnal Kesehatan Komunitas*, vol. 10, no. 3, pp. 546–554, 2025, doi: 10.25311/keskom.Vol10.Iss3.1734.
[28] A. Epizitone, S. P. Moyane, and I. E. Agbehadji, "A systematic literature review of health information systems for healthcare," *Healthcare*, vol. 11, no. 7, Art. no. 959, 2023, doi: 10.3390/healthcare11070959.
[29] K. F. Nisa, T. Dompak, and K. T. Lodan, "Perbandingan sistem pelayanan kesehatan di Indonesia dan di Singapura," *Prosiding Seminar Nasional Ilmu Sosial dan Teknologi (SNISTEK)*, vol. 6, pp. 72–77, 2024.
[30] R. B. Cleveland, W. S. Cleveland, J. E. McRae, and I. Terpenning, "STL: a seasonal-trend decomposition procedure based on loess," *Journal of Official Statistics*, vol. 6, no. 1, pp. 3–73, 1990.

All open access articles published in Transactions on Computational Modeling and Intelligent Systems (http://tcmis.org) are distributed under the terms of the CC BY-NC 4.0 license (Creative Commons Attribution Non-Commercial 4.0 International Public License as currently displayed at http://creativecommons.org/licenses/by-nc/4.0/legalcode) which permits unrestricted use, distribution, and reproduction in any medium, for non-commercial purposes, provided the original work is properly cited.

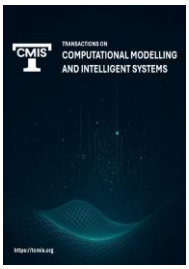

Transactions on
Computational Modeling and Intelligent Systems

Volume 4, July 2026, Article 10087
https://doi.org/10.65112.tcmis.10087

eISSN: 3158-5202
www.tcmis.org

RESEARCH ARTICLE

Nonlinear buoyancy-driven thermal energy transport on a moving vertical plate with boundary slips and non-uniform heat source/sink

Astick Banerjee[1], Sohita Rajput[2*], Krishnendu Bhattacharyya[3], Mitu Dular[3], Dimpal Sharma[3] and Sanat Kumar Mahato[4]

[1]*Department of Mathematics and Computing, Biswa Bangla Biswabidyalay, Bolpur, Birbhum-723104, West Bengal, India.*
[2]*Mathematics Section, Department of Science and Humanity, Sershah Engineering College, Sasaram-821113, Bihar, India.*
[3]*Department of Mathematics, Institute of Science, Banaras Hindu University, Varanasi-221005, Uttar Pradesh, India.*
[4]*Department of Mathematics, Sidho-Kanho-Birsha University, Purulia-723104, West Bengal, India.*

[*]*Corresponding Author. Email: sohita.math@gmail.com (S. Rajput)*

Article Information

Received: 17 May 2026
Accepted: 15 July 2026
Published: 19 July 2026

AMS 2020 Classification:
76D10, 80A19

Abstract

This work investigates the key controlling mechanisms of two-dimensional buoyancy-driven nonlinear mixed convection and thermal energy transport in the flow generated by a vertically moving plate with partial slip and variable heat source/sink effects. The problem is motivated by applications in nuclear power systems, polymer processing, and other industrial operations where nonlinear heat convection and controllable heat generation are essential. By employing suitable similarity transformations, the governing nonlinear partial differential equations are reduced to coupled ordinary differential equations, which are solved using the MATLAB bvp4c solver. A combination of graphical and tabulated results is used to illustrate the influence of key controlling parameters. The analysis uncovers several notable physical trends. Nonlinear mixed convection significantly lowers fluid temperature while enhancing near-wall velocity. Both temperature-dependent and space-dependent heat sources or sinks intensify or reduce the velocity and temperature distributions and simultaneously cause the thickening or thinning of the associated boundary layers. Velocity slip and thermal jump at the surface reduce the near-wall momentum, which causes a reduction in velocity inside the boundary layer. Heat sources, whether spatially-dependent or temperature-dependent, consistently reduce surface drag force and cooling rate, whereas heat sinks boost both drag force and heat removal. Most importantly, temperature-dependent and space-dependent heat source/sink mechanisms exhibit a stronger influence on heat transport regulation, making them an important mode of thermal control. Overall, the results demonstrate that mixed convection flow is highly sensitive to nonlinear buoyancy and non-uniform heat generation/absorption. These findings provide useful insights for the design and optimization of thermal management systems across a wide range of engineering applications.

Keywords: Thermal energy transport, nonlinear buoyancy, moving vertical plate, partial slip, non-uniform heat source/sink.

1. Introduction

Boundary layer flow and the associated heat transfer over flat plates have attracted substantial attention due to their fundamental importance in widespread engineering applications, including electronic cooling, nuclear reactor thermal management, heat exchangers, coating processes, polymer extrusion, geothermal energy systems, and other manufacturing operations involving moving surfaces. The two classical boundary layer flow models are the Blasius flow model [1], which models a fixed flat plate in a moving fluid, and the Sakiadis flow model [2], which reports a moving plate in a still fluid. Their corresponding heat transfer characteristics were examined by

Pohlhausen [3] and Tsou *et al.* [4], respectively. To simultaneously represent the two aforementioned models involving both surface and ambient fluid velocities, Abdelhafez [5], Afzal et al. [6], Ishak [7] and Mukhopadhyay et al. [8] developed generalised formulations based on composite velocity boundary conditions. More recently, Dholey [9], Renuka et al. [10], and Khashi'ie et al. [11] further extended those models by scrutinizing the influence of various physical mechanisms on boundary layer flow and thermal transport over flat plates.

Convection is one of the primary modes of heat transfer in boundary layer flows, facilitating the exchange of thermal energy among a solid surface and the surrounding fluid. Based on the mechanism responsible for fluid motion, convection is generally categorised as forced, free (natural), or mixed convection. Forced convection occurs when the flow is generated by external devices such as pumps, fans, or moving surfaces, while free convection results from buoyancy forces produced by temperature-dependent density differences within the fluid. When both mechanisms act simultaneously, the resulting flow is referred to as mixed convection. In such cases, the combined influence of inertial and buoyancy forces may either assist or oppose the flow, depending on their relative directions. Mixed convection is encountered in numerous practical situations, including electronic cooling, heat exchangers, solar thermal systems, nuclear reactor cooling, geothermal applications, and atmospheric transport, making it an important topic of research [12]. Detailed studies on mixed convection boundary layer flows are available in Refs. [13–16].

Many previous investigations have been carried out within the framework of linear mixed convection by adopting the Boussinesq approximation, which assumes a linear variation of fluid density with temperature. This approximation is generally adequate when the temperature difference is small. However, its accuracy decreases as the temperature difference increases, since the density–temperature relationship becomes nonlinear. The resulting change in buoyancy force can substantially affect both the flow and heat transfer characteristics. As a result, predictions of velocity, temperature, wall drag force, and heat transfer rate based on the linear approximation may no longer be reliable. To capture these effects more accurately, nonlinear buoyancy models are required, particularly in high-temperature applications such as solar thermal systems, combustion chambers, nuclear reactors, thermal energy storage units, glass manufacturing, and high-temperature material processing.

To overcome the limitations of the linear Boussinesq approximation, Goren [17] introduced a quadratic density-temperature relation in the buoyancy term for free convection flows, making the model applicable to situations involving large temperature differences. Later, Bandaru et al. [18] extended this idea to mixed convection by incorporating both linear and quadratic density-temperature variations in the analysis of flow over a rotating cone in a porous medium. Their study showed that accounting for nonlinear buoyancy leads to a more realistic prediction of flow and heat transfer properties. Since then, nonlinear mixed convection has been investigated extensively because of its importance in thermal systems with large temperature gradients. Recent studies [19–22] have examined such flows over different configurations, including stretching surfaces, vertical plates, vertically moving cylinders, and wedges. These investigations have consistently shown that the nonlinear thermal buoyancy parameter has a much greater influence on the flow and temperature fields than the concentration-dependent buoyancy parameter, emphasizing its dominant role in boundary layer transport.

Internal heat generation and absorption have a pronounced effect on thermal transport in boundary layer flows by modifying the energy balance within the fluid. Heat generation increases the fluid temperature, resulting in a thicker thermal boundary layer and altering the wall temperature gradient, which directly affect the rate of heat transfer. In contrast, heat absorption removes thermal energy from the fluid, reducing the thermal boundary layer thickness and increasing the temperature gradient at the surface. Because buoyancy-driven flow in mixed convection is closely linked to the temperature field, the presence of a heat source or sink can significantly influence both the flow and heat transfer. These effects are important in many engineering applications, including electronic cooling, nuclear reactor thermal management, residual heat removal from nuclear debris, radioactive waste disposal, polymer extrusion, rubber and plastic processing, geothermal energy systems, chemical reactors, and various metallurgical and energy conversion processes. In such systems, proper regulation of internal heat generation or absorption is essential for maintaining thermal stability and improving overall performance.

Early investigations primarily focused on uniform heat source/sink models, in which the rate of internal heat generation or absorption depends only on the local temperature field. Such models were employed by Mukhopadhyay [23], Gireesha et al. [24], and Roy and Pop [25] to examine the influence of temperature-dependent heat generation/absorption on boundary layer heat transfer. Although these studies provided valuable insights into the role of internal heating and cooling, they assumed that the heat source/sink remained spatially uniform throughout the flow domain, which may not accurately represent many practical thermal systems. In realistic engineering processes, however, the intensity of internal heat generation or absorption often varies with both the local temperature and the spatial location due to non-uniform energy production, localized heating, chemical reactions, electromagnetic heating, radiation, or variable material properties. To capture these physical characteristics more accurately, several researchers, including Abel and Mahesha [26], Mythili and Sivaraj [27], Gireesha et al. [28], and Khan et al. [29], incorporated non-uniform heat source/sink models in which the internal heat generation/absorption is presumed to depend simultaneously on temperature and spatial coordinates. Such

models provide a more realistic representation of practical thermal systems and enable a better understanding of how localized energy generation or absorption influences the development of thermal boundary layers, wall heat transfer, and the overall transport process.

The no-slip boundary condition, which assumes that the fluid velocity at a solid surface is equal to the velocity of the surface, has been a basic assumption in continuum fluid mechanics for many years. It provides reliable predictions for most macroscopic flows, where the interaction between the fluid and the solid boundary is sufficiently strong to eliminate any relative motion at the interface. However, this assumption is not always valid in microscale and nanoscale systems. In applications involving rarefied gases, hydrophobic and superhydrophobic surfaces, porous or coated materials, polymeric fluids, and microelectromechanical systems (MEMS), finite slip may occur because of weak intermolecular interactions and limited momentum exchange near the wall. Gad-el-Hak [30] emphasized that neglecting slip effects in such situations can lead to significant errors in predicting flow and heat transfer characteristics. To account for these effects, the no-slip condition is replaced by a partial slip boundary condition that allows a finite tangential velocity at the wall. Navier [31] first proposed this model by relating the slip velocity to the tangential shear rate at the surface. A similar idea is used for heat transfer through the thermal slip, or temperature jump, condition, in which the temperature difference among the wall and the adjacent fluid is proportional to the normal temperature gradient. These boundary conditions provide a more realistic description of momentum and heat transfer at fluid–solid interfaces, particularly in microscale transport problems. In fact, velocity slip reduces the transfer of momentum from the wall to the fluid, leading to lower wall shear stress and changes in the momentum boundary layer. Likewise, thermal slip limits the amount of heat transferred from the surface to the nearby fluid, thereby decreasing the wall heat flux and modifying the thermal boundary layer. As a result, partial slip provides an effective way to regulate both flow resistance and heat transfer, which is particularly useful in microfluidic devices, MEMS/NEMS, biomedical applications, advanced cooling systems, lubrication, coating technologies, and energy conversion equipment. Owing to these practical advantages, slip boundary conditions have been widely adopted in studies of fluid flow and heat transfer [32–35]. For instance, Li et al. [36] examined magnetohydrodynamic flow with Navier slip under a modified heat conduction model and showed that wall slip reduces the surface cooling rate by lowering the wall heat flux. More recently, Uddin et al. [37] investigated unsteady mixed convection flow with velocity slip and activation energy, demonstrating that slip has a significant effect on both the flow and thermal fields. These studies underline the importance of incorporating velocity and thermal slip in the analysis of microscale flows and other situations where the classical no-slip assumption is no longer appropriate.

Motivated by the limitations of earlier studies, the present work investigates the combined effects of several physical mechanisms that have rarely been considered together in boundary layer flow and heat transfer. Unlike most previous investigations, which were limited to linear mixed convection, uniform heat generation/absorption, stationary surfaces, and no-slip boundary conditions, the present model considers nonlinear mixed convection over a vertically moving plate in the presence of a spatially-dependent and temperature-dependent heat source/sink, together with velocity and thermal slip at the wall. By accounting for nonlinear buoyancy, wall motion, non-uniform internal heat generation/absorption, and finite momentum and thermal exchange at the fluid–solid interface, the model provides a more realistic description of the transport processes. The interaction of these effects has a marked influence on the velocity and thermal boundary layers, wall shear stress, and surface heat transfer. The findings of this study are expected to be valuable in the design and analysis of advanced cooling systems, nuclear reactor thermal management, geothermal energy extraction, polymer processing, coating operations, microfluidic devices, and other thermal systems involving moving surfaces, internal heat generation, and slip effects. The results therefore provide useful insights into the design and optimization of thermal systems where precise control of fluid flow and heat transfer is essential.

The governing equations for the conservation of mass, momentum, and energy are first transformed into a system of coupled nonlinear ordinary differential equations using suitable similarity transformations. The transformed boundary value problem is then solved numerically with the MATLAB bvp4c solver, which has been widely used for nonlinear boundary layer problems because of its accuracy and reliability. A detailed parametric study is carried out to examine the effects of the governing parameters on the velocity and temperature distributions, skin-friction coefficient, and local Nusselt number. The results are presented through graphs and tables to clearly illustrate how the controlling parameters influence the flow and heat transfer characteristics.

The key novelty of this investigation comes from the combined and simultaneous consideration of several complex physical phenomena which have not been addressed together previously:

(a) Incorporation of nonlinear mixed convection with temperature-dependent and space-dependent non-uniform heat source/sink, permitting a more realistic representation of internal heating designs found in advanced thermal systems.

(b) Inclusion of both velocity slip and thermal jump boundary conditions, accounting for microscale surface interactions that considerably alter transport phenomena near the plate.

(c) Coupling of a moving vertical plate with buoyancy-driven effects, producing a multi-driving force flow environment that introduces additional nonlinear behaviour.

(d) Detailed quantification of competing thermal and momentum transport mechanisms, revealing how slip, heat source/sink strength, buoyancy, and wall motion interact to shape shear stress and heat transfer characteristics.

To the best of the authors' knowledge, such a combination of nonlinear mixed convection, non-uniform heat source/sink, moving surface, and dual slip boundary conditions has not been previously reported, and thus provides new physical insights into boundary-layer transport phenomena relevant to modern thermal engineering applications.

2. Formulation and basic equations

Consider the steady-state non-linear buoyancy-driven mixed convection over a vertical plate incorporating non-uniform heat source/sink. The *x*-axis is taken along the plate, while the *y*-axis is considered perpendicular to it. Governing equations within boundary layer are specified as [21, 22, 24]:

$$\frac{\partial u}{\partial x}+\frac{\partial v}{\partial y}=0\,, \tag{1}$$

$$u\frac{\partial u}{\partial x}+v\frac{\partial v}{\partial y}=\upsilon\frac{\partial^2 u}{\partial y^2}+g[\beta_0(T-T_\infty)+\beta_1(T-T_\infty)^2]\,, \tag{2}$$

$$u\frac{\partial T}{\partial x}+v\frac{\partial T}{\partial y}=\frac{\kappa}{(\rho c_p)}\frac{\partial^2 T}{\partial y^2}+\frac{1}{\rho c_p}q^*\,, \tag{3}$$

with boundary conditions(BCs)

$$u=U_w+L_1\frac{\partial u}{\partial y}, v=0 \text{ at } y=0\,,\ u\to 0 \text{ as } y\to\infty\,, \tag{4}$$

$$T=T_w+D_1\frac{\partial T}{\partial y} \text{ at } y=0\,,\ T\to T_\infty \text{ as } y\to\infty, \tag{5}$$

where u and v are the velocity components along *x*- and *y*-axes, respectively, T gives the temperature, $\upsilon=\mu/\rho$ denotes the kinematic viscosity, β_0 and β_1 represent linear and nonlinear thermal expansion coefficients, T_w and T_∞ respectively give the constant temperatures at the plate and in the free-stream with $T_w>T_\infty$, U_w is surface velocity, *g* is the acceleration due to gravity, and κ, (ρc_p), μ, and ρ are the thermal conductivity, heat capacity, viscosity, and density, respectively. Here, $L_1=L\,\mathrm{Re}_x^{1/2}$ and $D_1=D\,\mathrm{Re}_x^{1/2}$ are the velocity slip and thermal slip factors with *L* and *D* being the initial values of L_1 and D_1 having dimension of length, and $\mathrm{Re}_x=U_w x/\upsilon$ gives the local Reynolds number. The physical layout of the problem being investigated is depicted in Figure 1.

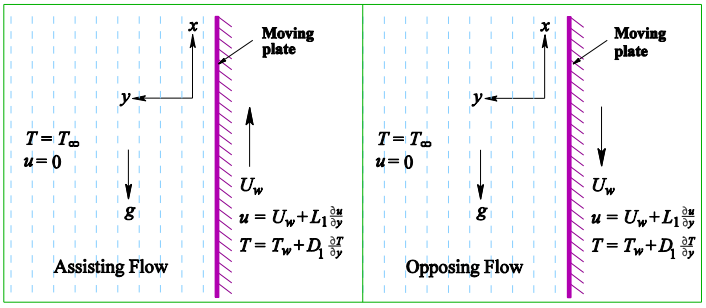

Figure 1. Physical diagram of considered problem.

The adopted heat generation/absorption model represents a non-uniform internal heat source/sink whose strength depends on both the local fluid temperature and the spatial location within the boundary layer. It is more realistic than the conventional uniform heat source/sink model because, in many practical thermal systems, heat is neither generated nor absorbed uniformly throughout the flow domain.

The dimensional heat source/sink is expressed as [24, 27]:

$$q^* = \frac{\kappa U_w}{\upsilon x}\left[q_1(T - T_\infty) + q_2(T_w - T_\infty) e^{-\frac{y}{x}\sqrt{\frac{U_w x}{\upsilon}}} \right]. \tag{6}$$

The term $q_1(T - T_\infty)$ implies that the rate of internal heat generation (or absorption) varies with the local temperature difference among the fluid and the ambient environment. Whereas, the $q_2(T_w - T_\infty)e^{-\frac{y}{x}\sqrt{\frac{U_w x}{\upsilon}}}$ term refers to the spatial variation of the heat source/sink and the exponential function decreases rapidly as the distance from the wall increases. Therefore, maximum heat generation (or absorption) occurs near the wall and the source/sink gradually weakens away from the surface. Here, q_1 and q_2 are coefficients of temperature-dependent and space-dependent heat source/sink, respectively. It should be noted that $q_1 > 0$, $q_2 > 0$ produces heat source and $q_1 < 0$, $q_2 < 0$ represents heat sink. These two parameters control the strength of the two mechanisms independently.

The following transformations are employed:

$$\psi = \sqrt{U_w \upsilon x} f(\eta) \text{ and } T = T_\infty + (T_w - T_\infty)\theta(\eta), \tag{7}$$

where $\eta = (y/x)\,\mathrm{Re}_x^{1/2}$ is a variable, f and θ are dimensionless functions.

Using aforementioned transformations, the equations and BCs reduce to

$$f''' + \frac{1}{2} f f'' + \lambda\theta(1 + \gamma\theta) = 0, \tag{8}$$

$$\theta'' + \frac{1}{2}\mathrm{Pr}\, f\theta' + q_1\theta + q_2 e^{-\eta} = 0, \tag{9}$$

with

$$f(0) = 0,\ f'(0) = 1 + \delta_1 f''(0),\ f'(\infty) = 0, \tag{10}$$

$$\theta(0) = 1 + \delta_2\theta'(0),\ \theta(\infty) = 0, \tag{11}$$

where $\lambda = \frac{Gr_x}{\mathrm{Re}_x^2}$, $Gr_x = \frac{g\beta_0(T_w - T_\infty)x^3}{\upsilon^2}$, $\gamma = \frac{\beta_1}{\beta_0}(T_w - T_\infty)$, $\mathrm{Pr} = \frac{\upsilon\rho c_p}{\kappa}$, $\delta_1 = \frac{LU_w}{\upsilon}$ and $\delta_2 = \frac{DU_w}{\upsilon}$ are the linear buoyancy parameter, local Grashof number, nonlinear convection parameter, Prandtl number, velocity and thermal slip parameters, respectively.

The local skin-friction coefficient and Nusselt number, representing the shear stress and heat transfer rate at the surface, respectively, are defined in standard form as follows:

$$C_{fx} = \frac{\tau_w}{\rho U_w^2} \text{ and } Nu_x = \frac{x q_w}{\kappa\left(T_w - T_\infty\right)}, \tag{12}$$

where $\tau_w = \mu\left(\frac{\partial u}{\partial y}\right)_{y=0}$ and $q_w = -\kappa\left(\frac{\partial T}{\partial y}\right)_{y=0}$.

So, above quantities reduce to

$$\left.\begin{aligned} \mathrm{Re}^{1/2} C_{fx} &= f''(0), \\ \mathrm{Re}^{-1/2} Nu_x &= -\theta'(0). \end{aligned}\right\} \tag{13}$$

3. Solution methodology and its validations

The coupled nonlinear ODEs given in Eqs. (8)-(11) are solved using 'bvp4c', a MATLAB program which is built on Lobatto IIIA technique (a finite difference scheme producing C^1-continuous solutions). This approach minimizes sensitivity to starting estimates by automatically adapting the computational mesh for accuracy and offering reliable results even in the absence of closed-form initial assumptions. Boundary value problems in bvp4c are solved using the setting sol=bvp4c(odefun, bcfun,solinit,options). In this case, odefun stores the system of first-order ordinary differential equations, bcfun specifies the boundary conditions, solinit describes the initial guess values, and options=bvpset('RelTol',1e-6, 'AbsTol',1e-6) is used to establish the relative and absolute error tolerances.

Since the bvp4c is applied on a first order system, the Eqs. (8)-(11) are transformed into the following first-order system:

$$\left.\begin{aligned} f' = g,\ g' = h,\ h' = -\frac{1}{2} fh - \lambda\theta\left(1+\gamma\theta\right), \\ \theta' = \Theta,\ \Theta' = -\frac{1}{2}\Pr f\Theta - q_1\theta - q_2 e^{-\eta}, \end{aligned}\right\} \tag{14}$$

with

$$f(0) = 0,\ g(0) = 1+\delta_1 h(0),\ \theta(0) = 1+\delta_2\Theta(0). \tag{15}$$

To start integration, introductory guess values of non-prescribed initial conditions $h(0)$ and $\Theta(0)$, i.e., $f''(0)$ and $\theta'(0)$ are essential and the values are selected in such a manner that they produce asymptotic convergence to specified boundary conditions. Here, the error is determined by the residual error with tolerance being 10^{-5}.

To validate the accuracy of the present numerical methodology, the computed values of the skin-friction coefficient $\mathrm{Re}^{1/2} C_{fx}$ for the forced convection case are compared with the previously reported results of Bataller [38], Ahmad et al. [39], and Rahman et al. [40], as presented in Table 1. An excellent agreement is observed between the present computations and the available benchmark solutions over the entire range of parameters considered. This close correspondence approves the accuracy and dependability of the adapted numerical procedure, thereby providing strong confidence in the correctness of the results and the subsequent physical interpretations presented in this study.

Table 1. Comparison of skin-friction coefficient $\mathrm{Re}^{1/2} C_{fx}$ for $\lambda = 0$.

δ_1	Bataller [38]	Ahmad et al. [39]	Rahman et al. [40]	Present results
0	0.4437	0.4446	0.4438	0.4439043
0.2			0.3925	0.3927017
0.4			0.3531	0.3533116

4. Results and discussion

The governing mathematical model is solved numerically to examine the underlying flow physics. Furthermore, a detailed parametric examination is conducted to assess the effects of the linear and nonlinear mixed convection parameters, temperature-dependent and space-dependent heat source/sink, and velocity and thermal slips on the velocity and temperature fields, together with the corresponding wall drag force and rate of surface cooling, as exhibited in Figures 2-25. Throughout the numerical computations, the parameter values are fixed as: $\lambda = 0.1$, $\gamma = 0.5$, $q_1 = 0.04$, $q_2 = 0.1$, $\delta_1 = 0.2$, $\delta_2 = 0.1$ and ($q_1 = -0.04$, $q_2 = -0.1$, in case of a sink). Unless otherwise specified, these values remain unchanged.

The effects of varying the convection parameters on the velocity and temperature profiles are illustrated in Figures 2-5. Here, $\lambda < 0$, $\lambda > 0$, and $\lambda = 0$ correspond to opposing, assisting, and forced convection flows, respectively. The fluid velocity rises with an increase in the linear mixed convection parameter under assisting flow conditions $(\lambda > 0)$ as demonstrated by Figure 2. This enhancement occurs because the buoyancy force acts in the identical direction as the main flow, accelerating the fluid, raising the momentum boundary layer thickness (BLT), and producing a more favourable flow environment. In contrast, under opposing flow situations $(\lambda < 0)$, the buoyancy force executes against the fluid motion, thereby decelerating the flow and thinning the momentum boundary layer. Consequently, the velocity attained in the forced convection case $(\lambda = 0)$ lies between those of the assisting and opposing flow regimes. The corresponding temperature distributions are presented in Figure 3. An opposite trend is observed with respect to the velocity field. As the linear mixed convection parameter grows, the temperature and thermal BLT decrease because the accelerated fluid transports heat away from the surface more effectively, thereby enhancing convective heat transfer. Conversely, the decelerated flow in the opposing convection regime weakens convective transport, allowing more thermal energy to collect within the boundary layer, which produces higher temperature of fluid and a thicker thermal boundary layer. Accordingly, the temperature in the forced convection case remains lower than that in opposing flow but higher than that in assisting flow.

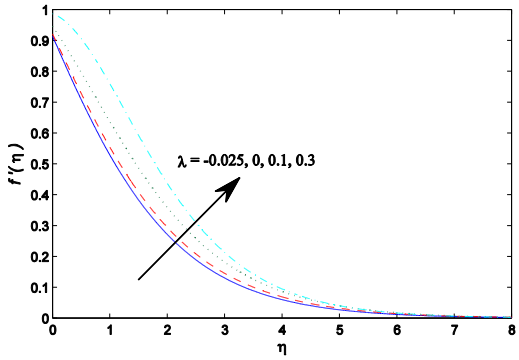

Figure 2. Variations in $f'(\eta)$ for several λ with $\gamma = 0.5$, $q_1 = 0.04$, $q_2 = 0.1$, $\delta_1 = 0.2$, $\delta_2 = 0.1$.

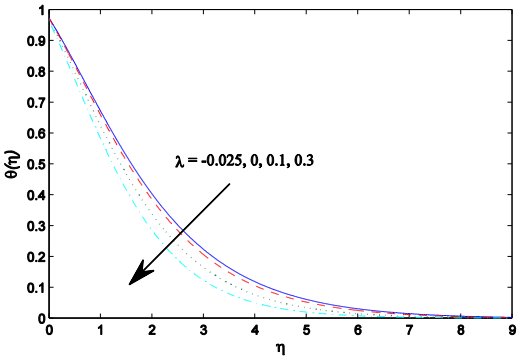

Figure 3. Variations in $\theta(\eta)$ for several λ with $\gamma = 0.5$, $q_1 = 0.04$, $q_2 = 0.1$, $\delta_1 = 0.2$, $\delta_2 = 0.1$.

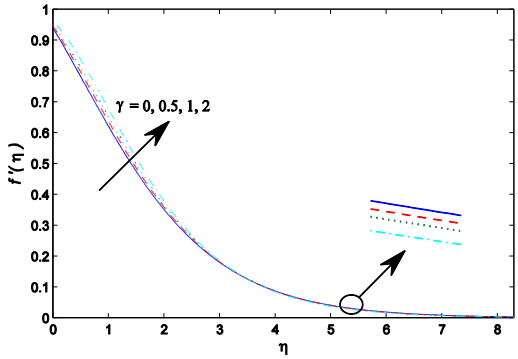

Figure 4. Variations in $f'(\eta)$ for several γ with $\lambda = 0.1$, $q_1 = 0.04$, $q_2 = 0.1$, $\delta_1 = 0.2$, $\delta_2 = 0.1$.

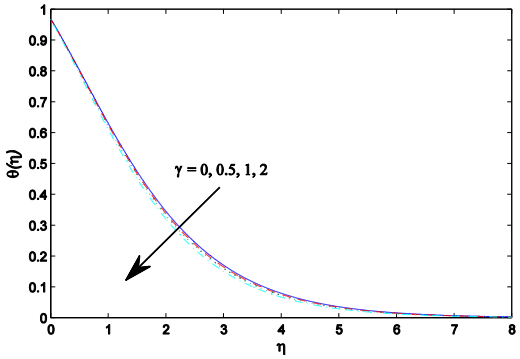

Figure 5. Variations in $\theta(\eta)$ for several γ with $\lambda = 0.1$, $q_1 = 0.04$, $q_2 = 0.1$, $\delta_1 = 0.2$, $\delta_2 = 0.1$.

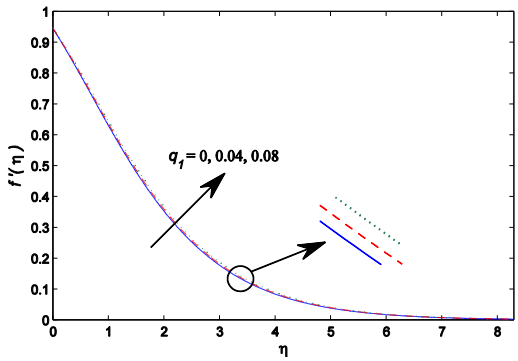

Figure 6. Variations in $f'(\eta)$ for several $q_1(\geq 0)$ with $\lambda = 0.1$, $\gamma = 0.5$, $q_2 = 0.1$, $\delta_1 = 0.2$, $\delta_2 = 0.1$.

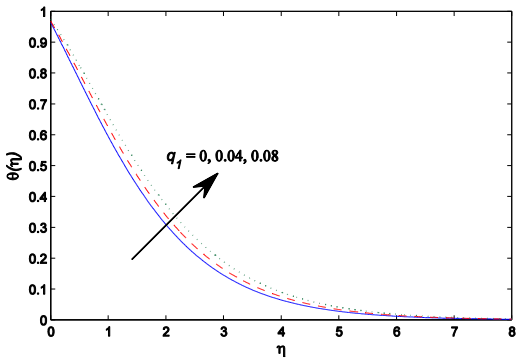

Figure 7. Variations in $\theta(\eta)$ for several $q_1(\geq 0)$ with $\lambda = 0.1$, $\gamma = 0.5$, $q_2 = 0.1$, $\delta_1 = 0.2$, $\delta_2 = 0.1$.

The effects of the nonlinear mixed convection parameter (γ) on the velocity and temperature distributions are illustrated in Figures 4 and 5. It is worth mentioning that ($\gamma = 0$) corresponds to the classical linear mixed convection model. As γ increases, the velocity exhibits a non-uniform response: the fluid velocity increases in the vicinity of the surface, whereas it declines in the outer region of the boundary layer. This performance is attributed to the nonlinear dependence of the buoyancy force on temperature. Near the heated plate, where the temperature difference among the wall and the nearby fluid is huge, the resulting nonlinear buoyancy force becomes stronger, producing an additional driving force that accelerates the fluid motion. However, as the distance from the surface increases, the temperature difference reduces quickly, consequently causing the nonlinear buoyancy effect to weaken. Hence, the momentum produced by buoyancy becomes inadequate to sustain the enhanced flow, leading to a decrease in velocity in the far-field region. Figure 5 unveils that raising the nonlinear mixed convection parameter diminishes both the fluid temperature and the thermal BLT. The strengthened near-wall buoyancy rushes the fluid motion, which promotes stronger convective transport of thermal energy away from the heated plate wall and accordingly it suppresses the thermal boundary layer development. Furthermore, the temperature and thermal

boundary layer are in higher level for the linear convection case $(\gamma = 0)$ than for the nonlinear convection case. In the linear model, the buoyancy force changes in direct proportion to temperature, whereas the nonlinear model produces a stronger buoyancy force in the high-temperature region near the wall. As the fluid temperature gradually approaches the free-stream value, the nonlinear buoyancy effect weakens. Consequently, nonlinear convection transfers heat more efficiently in the near-wall region, resulting in lower fluid temperatures and a thinner thermal boundary layer.

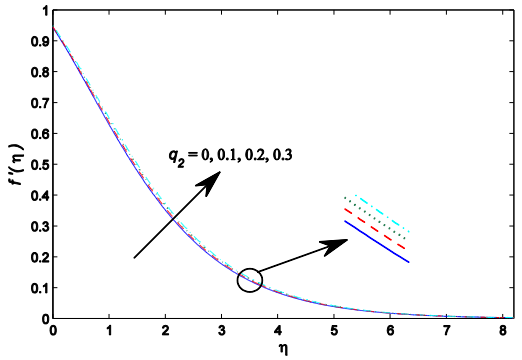

Figure 8. Variations in $f'(\eta)$ for several $q_2(\geq 0)$ with $\lambda = 0.1,\ \gamma = 0.5,\ q_1 = 0.04,\ \delta_1 = 0.2,\ \delta_2 = 0.1$.

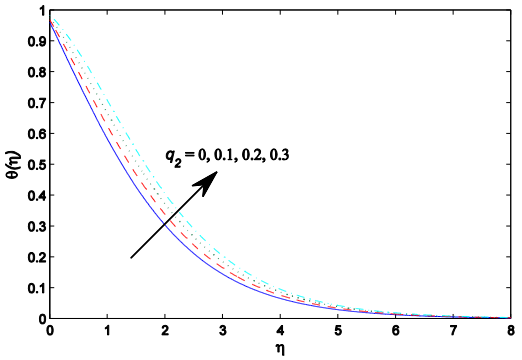

Figure 9. Variations in $\theta(\eta)$ for several $q_2(\geq 0)$ with $\lambda = 0.1,\ \gamma = 0.5,\ q_1 = 0.04,\ \delta_1 = 0.2,\ \delta_2 = 0.1$.

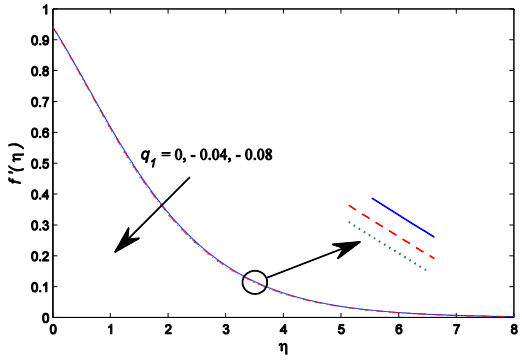

Figure 10. Variations in $f'(\eta)$ for several $q_1(\leq 0)$ with $\lambda = 0.1,\ \gamma = 0.5,\ q_2 = -0.1,\ \delta_1 = 0.2,\ \delta_2 = 0.1$.

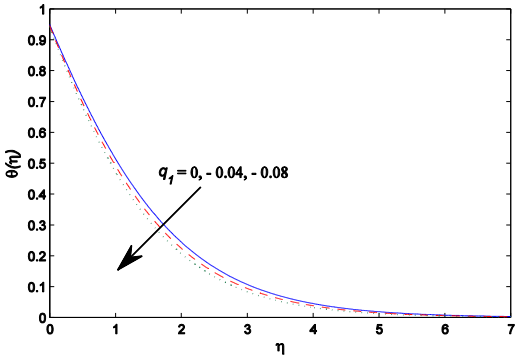

Figure 11. Variations in $\theta(\eta)$ for several $q_1(\leq 0)$ with $\lambda = 0.1,\ \gamma = 0.5,\ q_2 = -0.1,\ \delta_1 = 0.2,\ \delta_2 = 0.1$.

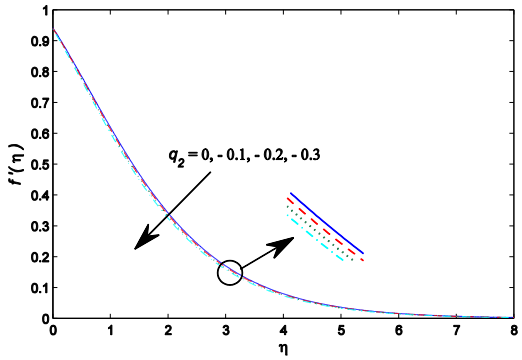

Figure 12. Variations in $f'(\eta)$ for several $q_2(\leq 0)$ with $\lambda = 0.1,\ \gamma = 0.5,\ q_1 = -0.04,\ \delta_1 = 0.2,\ \delta_2 = 0.1$.

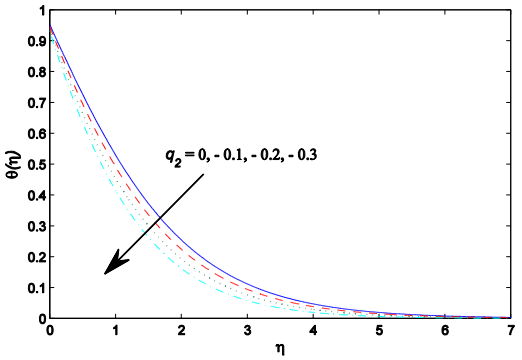

Figure 13. Variations in $\theta(\eta)$ for several $q_2(\leq 0)$ with $\lambda = 0.1,\ \gamma = 0.5,\ q_1 = -0.04,\ \delta_1 = 0.2,\ \delta_2 = 0.1$.

The variations of velocity and temperature distributions with the temperature-dependent and space-dependent heat source/sink parameters are depicted in Figures 6-13. In the presence of a heat source, both the velocity and temperature upsurge, whereas the opposite trend is observed when there is a heat sink. This impact is a direct consequence of the modification of the thermal energy within the boundary layer. Moreover, the presence of a heat source uninterruptedly supplies thermal energy to the fluid, causing temperature hike by strengthening the thermal buoyancy force. The enhanced buoyancy produces acceleration in the fluid flow, which causes higher velocities and a thicker momentum boundary layer. On the contrary, a heat sink removes thermal energy from the fluid,

which reduces the temperature difference among the wall and the nearby fluid and the weaker buoyancy force causes a reduction in the fluid velocity throughout the boundary layer. The corresponding temperature distributions exhibit that both the temperature-dependent and space-dependent heat source/sink parameters produce similar influences on the thermal variations. Increasing any source parameter introduces extra heat into the fluid, causing the rise of temperature and a larger thermal BLT. In contrast, increasing the strength of either heat sink parameter enhances heat absorption from the fluid, thereby suppressing the thermal distribution, reducing the thermal BLT, and promoting a steeper temperature gradient at the wall. From a heat transfer perspective, the heat source weakens the wall heat transfer rate by increasing the thermal energy within the boundary layer, whereas the heat sink intensifies this wall heat transfer through the continuous removal of thermal energy from the fluid. Consequently, the thermal boundary layer becomes thicker in the presence of a heat source and thinner when a heat sink is applied.

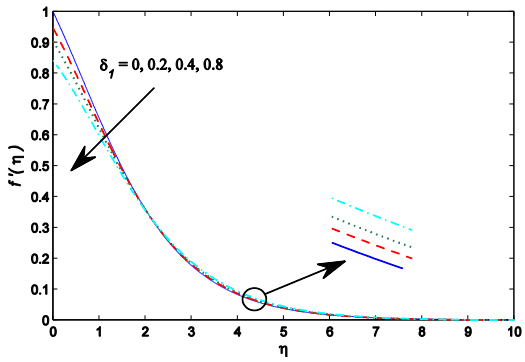

Figure 14. Variations in $f'(\eta)$ for several δ_1 with $\lambda = 0.1$, $\gamma = 0.5$, $q_1 = 0.04$, $q_2 = 0.1$, $\delta_2 = 0.1$.

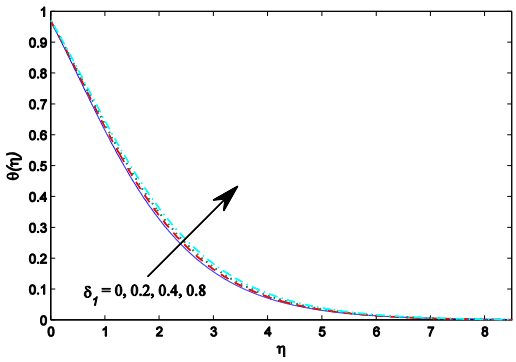

Figure 15. Temperature $\theta(\eta)$ for various δ_1 with $\lambda = 0.1$, $\gamma = 0.5$, $q_1 = 0.04$, $q_2 = 0.1$, $\delta_2 = 0.1$.

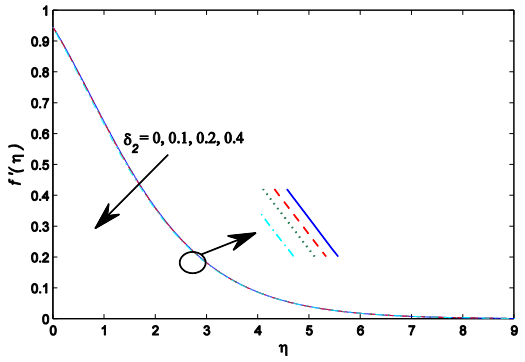

Figure 16. Variations in $f'(\eta)$ for several δ_2 with $\lambda = 0.1$, $\gamma = 0.5$, $q_1 = 0.04$, $q_2 = 0.1$, $\delta_1 = 0.2$.

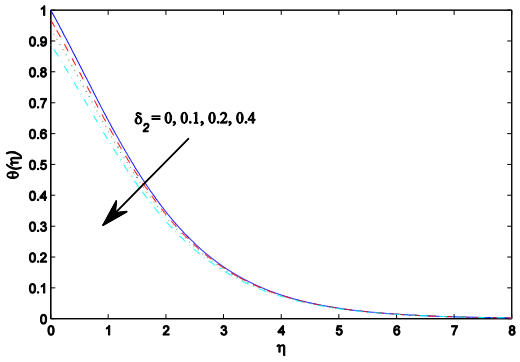

Figure 17. Temperature $\theta(\eta)$ for various δ_2 with $\lambda = 0.1$, $\gamma = 0.5$, $q_1 = 0.04$, $q_2 = 0.1$, $\delta_1 = 0.2$.

The differences in velocity and temperature due to changes in the velocity and thermal slip parameters are demonstrated in Figures 14-17. It should be noted that the present slip model reduces to the classical no-slip/no-temperature-jump boundary condition when the corresponding slip parameters are set to zero. The results in Figure 14 establish that increasing the velocity slip parameter produces a dual effect on the velocity field. In the vicinity of the wall, the fluid velocity decreases because the tangential slip weakens the momentum transfer from the moving surface to the adjacent fluid layers. As a result, the wall exerts less shear stress on the fluid, reducing its acceleration near the boundary. However, farther away from the surface, the velocity becomes slightly higher than that of the no-slip case owing to the redistribution of momentum within the boundary layer. The reduced wall friction delays the decay of the fluid motion, thereby yielding relatively higher velocities in the outer region of the boundary layer. Increasing the velocity slip parameter uplifts the fluid temperature and increases the thermal BLT (Figure 15). This behaviour arises because the weakened momentum transfer suppresses fluid mixing and convective heat transport near the wall, allowing heat energy to gather inside the boundary layer. Consequently, the thermal diffusion process becomes more dominant, resulting in higher temperatures throughout the flow field.

The impact of thermal slip (thermal jump) is presented in Figures 16 and 17. It is observed that increasing the thermal slip parameter reduces both the fluid velocity and temperature. Physically, thermal slip introduces a finite temperature discontinuity at the wall, thereby reducing the amount of heat transferred from the surface to the adjacent fluid. The reduction in thermal energy weakens the buoyancy force, which drives the mixed convection flow and due to this weaker buoyancy force fluid velocity reduces. At the same time, the decrease in wall heat flux suppresses the thermal field, generating a noticeable reduction in the fluid temperature and in the thermal BLT.

This cooling effect is more dominant near the wall, where the thermal slip condition restricts heat transfer from the surface to the adjacent fluid. As the distance from the wall increases, the influence of thermal slip gradually diminishes because the fluid temperature progressively approaches the ambient value.

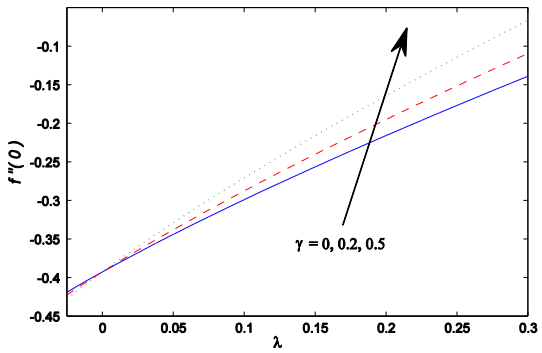

Figure 18. Local skin-friction $f''(0)$ with λ for various γ with $q_1 = 0.04,\ q_2 = 0.1,\ \delta_1 = 0.2,\ \delta_2 = 0.1$.

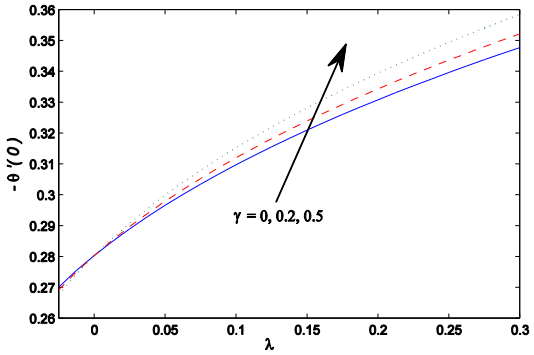

Figure 19. Local Nusselt number $-\theta'(0)$ with λ for various γ with $q_1 = 0.04,\ q_2 = 0.1,\ \delta_1 = 0.2,\ \delta_2 = 0.1$.

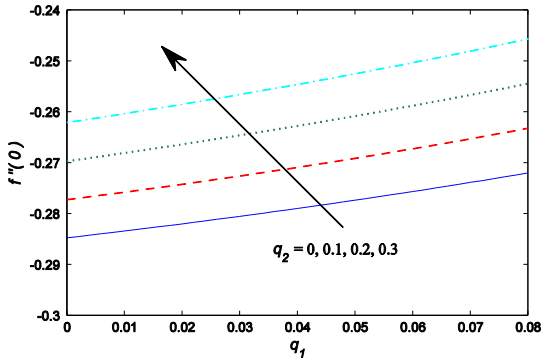

Figure 20. Local skin-friction $f''(0)$ with $q_1(\geq 0)$ for various $q_2(\geq 0)$ with $\lambda = 0.1,\ \gamma = 0.5,\ \delta_1 = 0.2,\ \delta_2 = 0.1$.

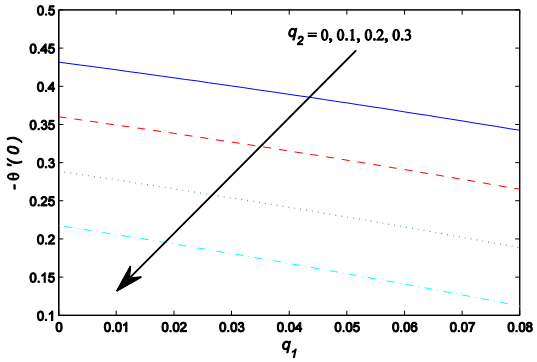

Figure 21. Local Nusselt number $-\theta'(0)$ with $q_1(\geq 0)$ for various $q_2(\geq 0)$ with $\lambda = 0.1,\ \gamma = 0.5,\ \delta_1 = 0.2,\ \delta_2 = 0.1$.

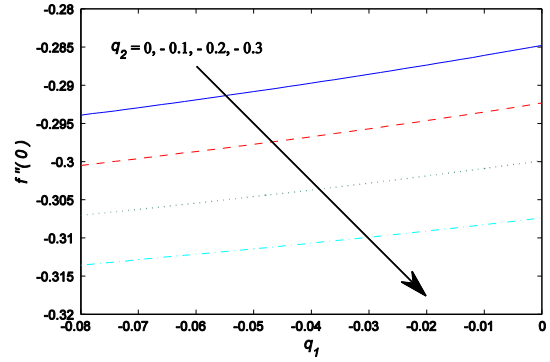

Figure 22. Local skin-friction $f''(0)$ with $q_1(\leq 0)$ for various $q_2(\leq 0)$ with $\lambda = 0.1,\ \gamma = 0.5,\ \delta_1 = 0.2,\ \delta_2 = 0.1$.

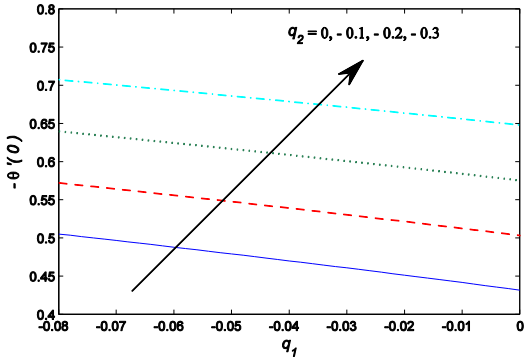

Figure 23. Local Nusselt number $-\theta'(0)$ with $q_1(\leq 0)$ for various $q_2(\leq 0)$ with $\lambda = 0.1,\ \gamma = 0.5,\ \delta_1 = 0.2,\ \delta_2 = 0.1$.

Finally, the impacts of the linear and nonlinear mixed convection parameters, temperature-dependent and space-dependent heat source/sink parameters, and partial velocity and thermal slips on the engineering quantities of practical interest, namely the surface drag force and the heat transfer rate at the wall are exemplified Figures in 18-25. It is witnessed that under assisting flow conditions, increasing either the linear or nonlinear mixed convection parameter diminishes the magnitude of the surface drag force while simultaneously enhancing the rate of heat transport from the heated wall. In assisting flow, the buoyancy force acts in the direction of the externally driven flow, thereby accelerating the fluid and reducing the velocity gradient at the wall, which lowers the wall shear stress. At the same time, the stronger fluid motion intensifies convective heat transport, resulting in a sharper temperature gradient at the wall and hence a higher Nusselt number. In the opposing flow case, the buoyancy force acts against the primary flow which originates a decline in the fluid motion and an increment in the wall shear

stress. The reduced convective transport also produces a lower wall heat transfer rate. These effects become more pronounced near the heated wall, where the larger temperature difference gives rise to stronger nonlinear buoyancy. Consequently, nonlinear mixed convection has a significant influence on both the wall drag force and the heat transfer rate at the wall.

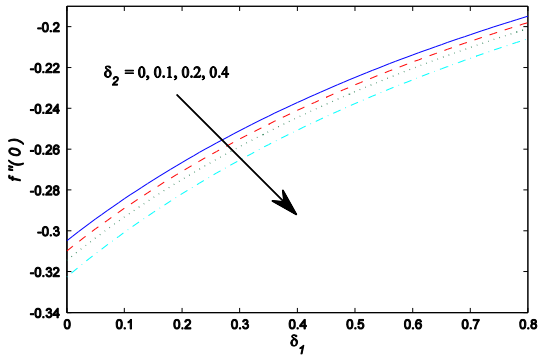

Figure 24. Local skin-friction $f''(0)$ with δ_1 for various δ_2 with $\lambda = 0.1,\ \gamma = 0.5,\ q_1 = 0.04,\ q_2 = 0.1$.

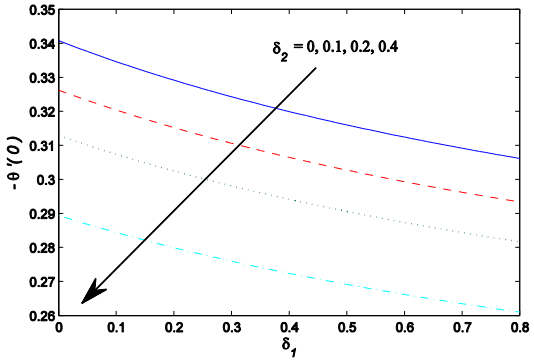

Figure 25. Local Nusselt number $-\theta'(0)$ with δ_1 for various δ_2 with $\lambda = 0.1,\ \gamma = 0.5,\ q_1 = 0.04,\ q_2 = 0.1$.

The influences of the temperature-dependent and space-dependent heat source/sink parameters on the engineering quantities are portrayed in Figures 20-23. It is evident that growing the strengths of both heat sources causes a decrease in the magnitude of the skin-friction coefficient, whereas the opposite trend is witnessed for the heat sink. Physically, the additional thermal energy added by the heat source uplifts the fluid temperature and increases the thermal BLT. This accumulation of heat energy weakens the wall velocity gradient, which reduces the surface drag exerted by the surface on the fluid. Conversely, a heat sink nonstop removes heat energy from the fluid, which reduces the thermal BLT and produces an increment in velocity gradient near the wall, i.e., the skin-friction coefficient. Similarly, the presence of a heat source reduces the wall temperature gradient because the heat energy is gathered within the boundary layer, which results in a lower Nusselt number. In contrast, a heat sink endlessly removes heat energy from the fluid, which promotes more efficient surface cooling, i.e., increases the rate of heat transfer.

The influences of velocity and thermal slips on the wall shear stress and heat transfer rate are exhibited in Figures 24 and 25. With a larger the velocity slip parameter, the magnitude of the skin-friction coefficient decreases because the slip boundary condition decays the transfer of tangential momentum from the wall to the fluid and it reduces the wall shear stress. In contrast, with increasing values of the thermal slip parameter, the skin-friction coefficient intensifies. Since thermal slip limits the transfer of heat from the wall to the nearby fluid, the buoyancy force reduces. Accordingly, this slows down the fluid motion and produces a superior wall drag force. In addition, increments of both velocity and thermal slip parameters reduce the local Nusselt number. Velocity slip reduces convective transport by dipping the momentum transport from the wall to the fluid, while thermal slip introduces a finite temperature jump at the wall, which diminishes the wall heat transfer rate.

The numerical values of the skin-friction coefficient and the local Nusselt number for different combinations of the governing parameters are presented in Table 2. These results are in close agreement with the graphical observations and this reconfirms of the trends discussed earlier regarding the impacts of the physical parameters on the flow field and thermal transport.

5. Conclusions and future research

The present study examines thermal energy transport in nonlinear mixed convection flow of a viscous fluid over a vertically moving plate in the presence of a temperature-dependent and space-dependent heat source/sink. To provide a more realistic description of the fluid-solid interface, the classical no-slip boundary conditions are replaced with partial velocity and thermal slip conditions. The resulting nonlinear boundary value problem is solved numerically using the MATLAB “bvp4c” solver, and the influences of the governing parameters on the flow and thermal fields, skin-friction coefficient, and heat transfer rate are analyzed in detail through graphical and numerical results. The major findings of the current investigation are summarized as follows:

- The linear mixed convection parameter has a significant influence on the flow and heat transfer characteristics. In the assisting flow case, the buoyancy force enhances the fluid motion, reduces the thickness of the momentum boundary layer, and improves the wall cooling rate. In contrast, opposing flow weakens the fluid motion, thickens the momentum boundary layer, and reduces the surface heat transfer rate.

Table 2. The values of $\mathrm{Re}^{1/2} C_{fx}$ and $\mathrm{Re}^{-1/2} Nu_x$ for the parameters λ, γ, q_1, q_2, δ_1, δ_2 and Pr.

λ	γ	q_1	q_2	δ_1	δ_2	Pr	$f''(0)$	$-\theta'(0)$
-0.025	0.5	0.04	0.1	0.2	0.1	1	-0.42771733	0.26760789
-0.01	0.5	0.04	0.1	0.2	0.1	1	-0.40637026	0.27552261
0	0.5	0.04	0.1	0.2	0.1	1	-0.39270177	0.28026413
0.1	0.5	0.04	0.1	0.2	0.1	1	-0.27085974	0.31522155
0.2	0.5	0.04	0.1	0.2	0.1	1	-0.16425981	0.33935216
0.3	0.5	0.04	0.1	0.2	0.1	1	-0.06633702	0.35845010
0.1	0	0.04	0.1	0.2	0.1	1	-0.29905004	0.30969727
0.1	0.25	0.04	0.1	0.2	0.1	1	-0.28486048	0.31250381
0.1	0.5	0.04	0.1	0.2	0.1	1	-0.27085974	0.31522155
0.1	0.75	0.04	0.1	0.2	0.1	1	-0.25703658	0.31785711
0.1	1	0.04	0.1	0.2	0.1	1	-0.24338094	0.32041637
0.1	1.25	0.04	0.1	0.2	0.1	1	-0.22988373	0.32290455
0.1	1.5	0.04	0.1	0.2	0.1	1	-0.21653675	0.32532632
0.1	1.75	0.04	0.1	0.2	0.1	1	-0.20333252	0.32768587
0.1	2	0.04	0.1	0.2	0.1	1	-0.19026425	0.32998699
0.1	0.5	-0.02	-0.1	0.2	0.1	1	-0.29463241	0.52187413
0.1	0.5	-0.04	-0.1	0.2	0.1	1	-0.29674266	0.53942356
0.1	0.5	-0.06	-0.1	0.2	0.1	1	-0.29870189	0.55626739
0.1	0.5	-0.08	-0.1	0.2	0.1	1	-0.30051242	0.57247451
0.1	0.5	0	0.1	0.2	0.1	1	-0.27722275	0.36006792
0.1	0.5	0.02	0.1	0.2	0.1	1	-0.27418990	0.33823133
0.1	0.5	0.04	0.1	0.2	0.1	1	-0.27085974	0.31522155
0.1	0.5	0.06	0.1	0.2	0.1	1	-0.26721264	0.29088397
0.1	0.5	0.08	0.1	0.2	0.1	1	-0.25943242	0.26287313
0.1	0.5	-0.04	-0.05	0.2	0.1	1	-0.29323511	0.50466836
0.1	0.5	-0.04	-0.1	0.2	0.1	1	-0.29674266	0.53942356
0.1	0.5	-0.04	-0.15	0.2	0.1	1	-0.30024249	0.57423564
0.1	0.5	-0.04	-0.2	0.2	0.1	1	-0.30373453	0.60910534
0.1	0.5	-0.04	-0.25	0.2	0.1	1	-0.30721875	0.64403345
0.1	0.5	-0.04	-0.3	0.2	0.1	1	-0.31068077	0.67901834
0.1	0.5	0.04	0	0.2	0.1	1	-0.27900698	0.38945331
0.1	0.5	0.04	0.05	0.2	0.1	1	-0.27493326	0.35228947
0.1	0.5	0.04	0.1	0.2	0.1	1	-0.27085974	0.31522155
0.1	0.5	0.04	0.15	0.2	0.1	1	-0.26678615	0.27824730
0.1	0.5	0.04	0.2	0.2	0.1	1	-0.26271225	0.24136462
0.1	0.5	0.04	0.25	0.2	0.1	1	-0.25863780	0.20457151
0.1	0.5	0.04	0.3	0.2	0.1	1	-0.25456261	0.16786604
0.1	0.5	0.04	0.1	0	0.1	1	-0.30987824	0.32623277
0.1	0.5	0.04	0.1	0.1	0.1	1	-0.28896798	0.32038814
0.1	0.5	0.04	0.1	0.2	0.1	1	-0.27085974	0.31522155
0.1	0.5	0.04	0.1	0.3	0.1	1	-0.25500365	0.31061414
0.1	0.5	0.04	0.1	0.4	0.1	1	-0.24098880	0.30647463
0.1	0.5	0.04	0.1	0.5	0.1	1	-0.22850113	0.30273144
0.1	0.5	0.04	0.1	0.6	0.1	1	-0.21729591	0.29932748
0.1	0.5	0.04	0.1	0.7	0.1	1	-0.20717930	0.29621655
0.1	0.5	0.04	0.1	0.8	0.1	1	-0.19799550	0.29336080
0.1	0.5	0.04	0.1	0.2	0	1	-0.26649202	0.32915924
0.1	0.5	0.04	0.1	0.2	0.1	1	-0.27085974	0.31522155
0.1	0.5	0.04	0.1	0.2	0.2	1	-0.27484186	0.30246671
0.1	0.5	0.04	0.1	0.2	0.3	1	-0.27848853	0.29074521
0.1	0.5	0.04	0.1	0.2	0.4	1	-0.28184136	0.27993238
0.1	0.5	0.04	0.1	0.2	0.1	0.5	-0.21568045	0.14050573
0.1	0.5	0.04	0.1	0.2	0.1	1	-0.27085974	0.31522155
0.1	0.5	0.04	0.1	0.2	0.1	1.5	-0.29540403	0.44029304
0.1	0.5	0.04	0.1	0.2	0.1	2	-0.30961321	0.54080633
0.1	0.5	0.04	0.1	0.2	0.1	2.5	-0.31913355	0.62636326
0.1	0.5	0.04	0.1	0.2	0.1	3	-0.32608624	0.70165325

- The nonlinear mixed convection parameter affects the velocity field in a non-uniform way. It hurries the fluid motion in the region close to the plate wall, but it reduces the velocity away from the plate. In addition, it causes a decline in the thermal BLT and an enhancement in convective heat transfer compared with the linear mixed convection case.

- Both temperature-dependent and space-dependent heat sources increase the fluid temperature, thicken the thermal boundary layer, and reduce the wall heat transfer rate, whereas the corresponding heat sinks effectively enhance surface cooling by promoting heat removal from the fluid.
- The temperature-dependent and space-dependent heat source/sink parameters exhibit similar qualitative effects on the thermal field, indicating that both mechanisms are equally effective in controlling the thermal transport within the boundary layer.
- Increasing the velocity slip parameter weakens the momentum transfer from the wall to the fluid, resulting in lower wall shear stress, higher fluid temperature, and a larger thermal BLT.
- Thermal slip (temperature jump) reduces the amount of heat transferred from the surface to the fluid, thereby lowering both the fluid temperature and the fluid velocity while suppressing the development of the thermal boundary layer.
- The magnitude of the skin-friction coefficient declines with increasing assisting and nonlinear mixed convection parameters, heat source strength, and velocity slip, whereas it rises under opposing convection, heat sink conditions, and higher thermal slip.
- The local Nusselt number upsurges under assisting and nonlinear mixed convection as well as heat sink conditions, while it decays in the presence of heat sources and both velocity and thermal slips due to the reduction in the wall temperature gradient.

The present investigation focuses on nonlinear mixed convection over a vertically moving surface in the presence of temperature-dependent and space-dependent heat source/sink under partial slip boundary conditions. The current model can be extended to explore a wider range of practical thermal engineering applications by incorporating electrically conducting nanofluids or hybrid nanofluids in the presence of magnetic (MHD) effects, which provide additional mechanisms for controlling fluid motion and heat transfer. Furthermore, the analysis may be generalized by considering alternative boundary conditions, such as convective heating, variable wall temperature or variable heat flux, wall permeability, and nonlinear slip models, to better represent realistic industrial and technological processes.

Acknowledgments

The authors would like to express their sincere gratitude to the esteemed reviewers for their valuable comments and constructive suggestions, which have significantly improved the quality of the manuscript.

Funding

None.

Conflict of interest

There is no conflict of interest to disclose.

Author contributions

All authors contributed equally to this work and approved the final version of the manuscript.

Declaration of using AI tools

The authors declare that they have not used any type of generative artificial intelligence for the writing of this manuscript, nor for the creation of images, graphics, tables, or their corresponding captions.

References

[1] H. Blasius, “Grenzschichten in Flüssigkeiten mit kleiner Reibung,” *Z. Math. Phys.*, vol. 56, pp. 1-37, 1908.

[2] B. C. Sakiadis, “Boundary-layer behaviour on continuous solid surfaces: boundary-layer equations for two dimensional and axisymmetric flow,” *AIChE J.*, vol. 7, pp. 26-28, 1961.

[3] E. Pohlhausen, “Der Wärmeaustausch zwischen festen Körpern und Flüssigkeiten mit kleiner Reibung und kleiner Wärmeleitung,” *Z. Angew. Math. Mech.*, vol. 1, pp. 121-151, 1921.

[4] F.K. Tsou, E.M. Sparrow, and R.J. Goldstein, “Flow and heat transfer in the boundary layer on a continuous moving surface,” *Int. J. Heat Mass Transf.*, vol. 10, pp. 219-235, 1967.

[5] T. A. Abdelhafez, “Skin friction and heat transfer on a continuous flat surface moving in a parallel free stream,” *Int. J. Heat Mass Transf.*, vol. 28, pp. 1234-1237, 1985.

[6] N. Afzal, A. Badaruddin, and A. A. Elgarvi, “Momentum and heat transport on a continuous flat surface moving in a parallel stream,” *Int. J. Heat Mass Transf.*, vol. 36, no. 13, pp. 3399-3403, 1993.

[7] A. Ishak, “Radiation effects on the flow and heat transfer over a moving plate in a parallel stream,” Chin. Phys. Lett., vol. 26, no. 3, art. id 034701, 2009.

[8] S. Mukhopadhyay, K. Bhattacharyya, and G. C. Layek, "Steady boundary layer flow and heat transfer over a porous moving plate in presence of thermal radiation," *Int. J. Heat Mass Transf.*, vol. 54, no. 13-14, pp. 2751-2757, 2011.

[9] S. Dholey, "On the fluid dynamics of unsteady separated stagnation-point flow of a power-law fluid on the surface of a moving flat plate," *Eur. J. Mech. B Fluids*, vol. 70, pp. 102-114, 2018.

[10] A. Renuka, M. Muthtamilselvan, Q. M. Al-Mdallal, D. H. Doh, and B. Abdalla, "Unsteady Separated Stagnation Point Flow of Nanofluid past a Moving Flat Surface in the Presence of Buongiorno's Model," J. Appl. Comput. Mech., vol. 7, no. 3, pp. 1283-1290, 2021.

[11] N. S. Khashi'ie, N. M. Arifin, and I. Pop, "Magnetohydrodynamics (MHD) boundary layer flow of hybrid nanofluid over a moving plate with Joule heating," *Alex. Eng. J.*, vol. 61, no. 3, pp. 1938-1945, 2022.

[12] B. Gebhart, Y. Jaluria, R.L. Mahajan, and B. Sammakia, *Buoyancy Induced Flows and Transport*, New York, Hemisphere, 1988.

[13] N. Afzal, and T. Hussain, "Mixed convection over a horizontal plate," *J. Heat Transf.*, vol. 106, pp. 240-241, 1986.

[14] A. Hamid, M. Alghamdi, M. Khan, and A. S. Alshomrani, "An investigation of thermal and solutal stratification effects on mixed convection flow and heat transfer of Williamson nanofluid," *J. Mol. Liq.*, vol. 284, pp. 307-315, 2019.

[15] A. Abbas, M. Ashraf, and A.J. Chamkha, "Combined effects of thermal radiation and thermophoretic motion on mixed convection boundary layer flow," *Alex. Eng. J.*, vol. 60, no. 3, pp. 3243-3252, 2021.

[16] N. S. Wahid, N. M. Arifin, N. S. Khashi'ie, I. Pop, N. Bachok, and M. E. Hafidzuddin, "MHD mixed convection flow of a hybrid nanofluid past a permeable vertical flat plate with thermal radiation effect," *Alex. Eng. J.*, vol. 61, no. 4, pp. 3323-3333, 2022.

[17] S. L. Goren, "On free convection in water at 4°C," *Chem. Eng. Sci.*, vol. 21, no 6-7, pp. 515-518, 1966.

[18] M. Bandaru, M. M. Rashidi, and H. S. Raju, "Influence of non-linear convection and thermophoresis on heat and mass transfer from a rotating cone to fluid flow in porous medium," *Ther. Sci.*, vol. 21, no. 6 Part B, pp. 2781-2793, 2017.

[19] A. Alsaedi, T. Hayat, S. Qayyum, and R. Yaqoob, "Eyring–Powell nanofluid flow with nonlinear mixed convection: entropy generation minimization," *Comput. Methods Programs Biomed.*, vol. 186, pp. 105183, 2020.

[20] P. M. Patil, and M. Kulkarni, "Nonlinear mixed convective nanofluid flow along moving vertical rough plate," *Revista mexicana de fisica.*, vol. 66, no. 2, pp. 153-161, 2020.

[21] P. M. Patil, M. Kulkarni, and P. S. Hiremath, "Nonlinear mixed convection flow of nanofluid past a moving vertical slender cylinder," *Arab. J. Sci. Eng.*, vol. 45, no. 2, pp. 1219-1228, 2020.

[22] S. Rajput, V. K. Verma, K. Bhattacharyya, and A. J. Chamkha, "Unsteady nonlinear mixed convective flow of nanofluid over a wedge: Buongiorno model," *Waves Random Complex Media*, 2021, DOI: 10.1080/17455030.2021.1987586.

[23] S. Mukhopadhyay, "Heat transfer analysis of the unsteady flow of a Maxwell fluid over a stretching surface in the presence of a heat source/sink," *Chin. Phys. Lett.*, vol. 29, no. 5, art. id. 054703, 2012.

[24] B. J. Gireesha, K. G. Kumar, G. K. Ramesh, and B. C. Prasannakumara, "Nonlinear convective heat and mass transfer of Oldroyd-B nanofluid over a stretching sheet in the presence of uniform heat source/sink," Results Phys., 2018;9:1555-63.

[25] N. C. Roy, and I. Pop, "Dual solutions of magnetohydrodynamic mixed convection flow of an Oldroyd-B nanofluid over a shrinking sheet with heat source/sink," *Alex. Eng. J.*, vol. 61, no. 8, pp. 5939-5948, 2022.

[26] M. S. Abel, and N. Mahesha, "Heat transfer in MHD viscoelastic fluid flow over a stretching sheet with variable thermal conductivity, non-uniform heat source and radiation," *Appl. Math. Model.*, vol. 32, no. 10, pp. 1965-1983, 2008.

[27] D. Mythili, and R. Sivaraj, "Influence of higher order chemical reaction and non-uniform heat source/sink on Casson fluid flow over a vertical cone and flat plate," *J. Mol. Liq.*, vol. 216, pp. 466-475, 2016.

[28] B. J. Gireesha, B. Mahanthesh, R. S. Gorla, and K. L. Krupalakshmi, "Mixed convection two-phase flow of Maxwell fluid under the influence of non-linear thermal radiation, non-uniform heat source/sink and fluid-particle suspension," *Ain Shams Eng. J.*, vol. 9, no. 4, pp. 735-746, 2018.

[29] U. Khan, A. Zaib, A. Ishak, E. S. Sherif, I. Waini, Y. M. Chu, and I. Pop, "Radiative mixed convective flow induced by hybrid nanofluid over a porous vertical cylinder in a porous media with irregular heat sink/source," *Case Stud. Therm. Eng.*, vol. 30, art. id. 101711, 2022.

[30] M. Gad-el-Hak, "The Fluid Mechanics of Microdevices – The Freeman Scholar Lecture," J. Fluids Eng., vol. 121, art. id. 5, 1999.

[31] C. L. M. H. Navier, "Memoire Surles du Movement des," *Mémoires de l'Académie Royale des Sciences de l'Institut de France*, vol. 1, no. 6, pp. 414-416, 1823.

[32] S. Shah, and S. Hussain, "Slip effect on mixed convective flow and heat transfer of magnetized UCM fluid through a porous medium in consequence of novel heat flux model," *Results Phys.*, vol. 20, art. id. 103749, 2021.

[33] A. Haritha, Y. Devasena, and B. Vishali, "MHD heat and mass transfer of the unsteady flow of a Maxwell fluid over a stretching surface with Navier slip and convective boundary conditions," *Global J. Pure Appl. Math.*, vol. 13, no. 6, pp. 2169-2179, 2017.

[34] W. Ibrahim, and M. Negera, "MHD slip flow of upper-convected Maxwell nanofluid over a stretching sheet with chemical reaction," *J. Egypt. Math. Soc*., vol. 7, pp. 1-28, 2020.

[35] H. Waqas, M. Imran, S. Khan, S. A. Shehzad, and M. A. Meraj, "Slip flow of Maxwell viscoelasticity-based micropolar nanoparticles with porous medium: a numerical study," *Appl. Math. Mech. (Engl. Ed.*), vol. 40, pp. 1255-1268, 2019.

[36] J. Li, L. Zheng, and L. Liu, "MHD viscoelastic flow and heat transfer over a vertical stretching sheet with Cattaneo-Christov heat flux effects," *J. Mol. Liq.*, vol. 221, pp. 19-25, 2016.

[37] I. Uddin, R. Akhtar, M. A. R. Khan, Z. Zhiyu, S. Islam, M. Shoaib, and M. A. Z. Raja, "Numerical treatment for fluidic system of activation energy with non-linear mixed convective and radiative flow of magneto nanomaterials with Navier's velocity slip," AIP Adv., vol. 9, art. id. 055210, 2019.

[38] R. C. Bataller, "Numerical comparisons of Blasius and Sakiadis flows," Matematika, vol. 26, pp. 187-196, 2010.

[39] S. Ahmad, A. M. Rohni, and I. Pop, "Blasius and Sakiadis problems in nanofluids," Acta Mechanica, vol. 218, pp. 195-204, 2011.

[40] N. H. A. Rahman, N. Bachok, and H. Rosali, "Boundary-layer flow and heat transfer of blasius and sakiadis problems in nanofluids with partial slip and thermal convection," CFD Letters, vol. 11, pp. 53-65, 2019.

All open access articles published in Transactions on Computational Modeling and Intelligent Systems (http://tcmis.org) are distributed under the terms of the CC BY-NC 4.0 license (Creative Commons Attribution Non-Commercial 4.0 International Public License as currently displayed at http://creativecommons.org/licenses/by-nc/4.0/legalcode) which permits unrestricted use, distribution, and reproduction in any medium, for non-commercial purposes, provided the original work is properly cited.

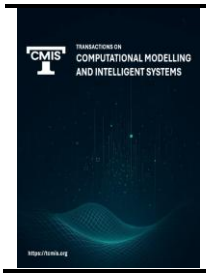

Transactions on
Computational Modeling
and Intelligent Systems

Volume 4, July 2026, Article 10080
https://doi.org/10.65112/tcmis.10080

eISSN: 3108-5202
www.tcmis.org

RESEARCH ARTICLE

Comparative study on heat and mass transfer performance of ternary hybrid nanoliquid over an exponentially stretching surface

Gangadhar Poojari Ashwinkumar[1*], Uppar Shivakumar[1], Bhandare Ranjana[1,2], and Pradeep Nanda[1,3]

[1] *Department of Mathematics, Vijayanagara Sri Krishnadevaraya University, Ballari, Karnataka, India.*
[2] *Department of Mathematics, Government First Grade College, Haliyal 581329, India.*
[3] *Department of Mathematics, Government First Grade College, Yelburga 583236, India.*

[*] *Corresponding Author. Email: ashwinpuje@gmail.com (G.P. Ashwinkumar)*

Article Information

Received: 14 April 2026
Accepted: 22 July 2026
Published: 25 July 2026

AMS 2020 Classification:
76W05, 76D10, 76-10

Abstract

Nowadays, enhanced heat transfer in conventional liquids is a major task in several nanotechnological applications. This work addresses the above issue by exploring the intuition behind hybrid nanoliquids by augmenting the thermal conductivity of a conventional liquid. For this, we performed a comparative analysis to evaluate the superior heat conduction properties of the three diverse solutions, namely nanoliquid, hybrid nanoliquid and ternary hybrid nanoliquid flow above an exponentially stretched surface under the action of uneven heat rise/fall effects. For the estimation of the enhanced thermal conductivity, three distinct systems were analyzed: a water-based Al nanofluid (NF), an Al+AA7072 hybrid mixture (HNF), and a tri-hybrid composition (THNF) consisting of Al+AA7072+AA7075, and we discussed the results in detail using simultaneous outcomes. The transformed governing equations are solved numerically using the MATLAB bvp5c solver. The influences of magnetic field, thermal radiation, non-uniform heat source/sink, chemical reaction, and nanoparticle volume fraction on the velocity, temperature, concentration, local Nusselt number, and Sherwood number are systematically investigated. The results demonstrate that the ternary hybrid nanoliquid exhibits superior heat- and mass-transfer performance compared with the corresponding hybrid and mono nanofluids.

Keywords: Magnetohydrodynamics, heat transfer, exponential stretched surface, nanofluid, and thermal radiation

1. Introduction

A nanofluid refers to a colloidal mixture where sub-micron particles are dispersed within a carrier medium. Nanoliquids exhibit an elevated thermal capacity and greater stability when combined with base fluids. These liquids typically offer superior Heating and refrigerating performance in Numerous engineering applications, including built-up procedures, microchip cooling, and astrophysical cooling systems. The study of nanoliquids originated with Choi and Eastman [1]. Later, the role of solar energy on the Lorentz force-influenced motion of nanofluids in a planar domain was analyzed via numerical techniques by Ghasemi et al. [2] using Rosseland approximation across a stretching plate. Eid [3] simulated the power of Thermal energy production under an MHD stream of nanoliquid above an exponentially stretching sheet. Ahmad and others [4] employed the Maxwell model to study the thermal transport characteristics of a water ferrofluid past a bidirectionally expanding exponential sheet. Moreover, Sulochana et al. [5] examined the effect of the Buongiorno slip mechanism on magnetohydrodynamic nanofluid flows over a permeable stretched surface and concluded that the energy transmission rate is enhanced with increasing Soret number. The current advances in analysing the energy-transfer performance of nanoliquids are reported in [6-10].

Later, Ghadikolaei et al. [11] numerically examined the dynamics of an MHD Casson nanoliquid past a nonlinear permeable spreading sheet with radiation. Further, Srinivasacharya and others [12] scrutinized the implications of velocity slip and ohmic heating, together with convective edge effects, over a stretched sheet. The motion of Oldroyd-B nanoliquid throughout an exponentially stretched region in the presence of microbes was discussed by Muhammad et al. [13]. The significance of extended heat flux for an MHD motion across a time-dependent, expanding region was established by Ahmed et al. [14]. Later, Seid et al. [15] theoretically simulated the cause of porosity and the effect of an applied magnetic field on a nanofluid stream in a vertically stretched region. The flow and energy transport behaviour of Maxwell nanoliquid under the control of heat radiation and chemical responses along an extending surface was clarified by the authors [16, 17].

Additionally, the thermal efficiency of nanoliquids is significantly enhanced by combining two distinct nanoparticles with similar or varying volumes in the base fluid, forming mixed or hybrid nanofluids. Compared with mono-nanofluids, these mixed nanofluids act as more effective heat-transfer agents. Many researchers presented their work on these advanced fluid types. Masoud et al. [18] experimentally studied the implications of nanomaterials pertaining to the rheological nature of $Fe_3O_4 - Ag/EG$ mixed nanoliquid. The Investigation on the impact of an induced magnetic force on stagnation-point movement for a past-extending plan was reported by Iqbal et al. [19]. Meanwhile, Hayat et al. [20] utilised a 3D pattern to witness the consequences of thermal emission and molecular interactions. The characteristics of the spinning flow of a $Cu - Al_2O_3$ Mixed nanoliquid with nonlinear radiation were modelled by Usman and colleagues [21].

The comparative motion analysis of three-dimensional MHD nanofluid and hybrid nanofluid across a stretching plane of uneven thickness was given by the researchers [22]. Later, Urmi and others [23] experimentally scrutinized the thermo-physical characteristics of $TiO_2 - Al_2O_3$ mixed nanofluid containing 0% ethylene glycol-based solvent. Sreedevi et al. [24] addressed the energy and mass transport phenomena of an electromagnetically influenced hybrid nanoliquid past a spreading sheet with suction and chemical effects. Further, Madhukesh et al. [25] performed the motion of a mixed nanoliquid ahead of a nonlinear, expanding boundary subjected to convective-type heating.

Recently, several researchers have found that tri-hybrid nanofluids demonstrate enhanced thermal conductivity when measured against dual-component hybrid systems. Ternary mixed nanofluids are a mixture of metallic or non-metallic oxides of three different nanomaterials in the elementary fluid. Hazarika et al. [26] examined the stream containing three nanoparticles Cu, Ag and Fe_3O_4 across a porous stretched geometry. Puneet et al. [27] addressed the stream and thermal transport nature of trihybrid nanofluids utilizing a refined Buongiorno model in the presence of bio-active mixers. The Motion and energy transport features of a trihybrid nanofluid across a curved, enlarged domain, as elaborated by Buongiorno's concept, were elaborated by Sarada and co-workers [28]. Building on this, Manjunath et al. [29] explained the Momentum and heat patterns transfer mechanism of ternary nanoliquid over a linear extending surface. The velocity analysis of a ternary hybrid nanoliquid along a vertical thermal cylinder is interpreted by Nazir et al. [30]. The entropy analysis of nanoparticles with H_2O+EG base liquid was discussed by Sohail et al. [31]. Additionally, Farhan et al. [32] investigated the stasis-point flow behaviour of a trihybrid nanoliquid past a stretchy rotating disc. The relative flow analysis of a graphene/magnesium oxide mixed nanofluid and a graphene/zirconium oxide/magnesium oxide trihybrid nanofluid, along with the slip effect across a moving plate, was presented by Prakash et al. [33].

Although several studies have investigated heat transfer in mono, hybrid, and ternary hybrid nanofluids over stretching surfaces, most have focused on a single fluid configuration or considered limited physical mechanisms. A systematic comparison of the thermal performance of Water–Al, Water–Al+AA7072, and Water–Al+AA7072+AA7075 nanofluids under identical flow conditions, including magnetohydrodynamic effects, thermal radiation, non-uniform heat source/sink, and chemical reaction, has received comparatively little attention. The present work addresses this gap by providing a unified computational framework to evaluate the influence of these governing parameters on momentum, thermal, and concentration fields, thereby identifying the relative heat-transfer enhancement achieved by ternary hybrid nanofluids.

The novelty of the present work lies not in introducing a new numerical algorithm or a new stretching-sheet model, but in establishing a unified comparative framework for evaluating the thermal performance of mono, hybrid, and ternary hybrid nanofluids under identical physical conditions. This approach enables the direct quantification of the incremental heat-transfer enhancement achieved through successive incorporation of multiple nanoparticles, which has received limited attention in previous studies.

Motivated by the aforementioned investigations, this research seeks to evaluate the heat transmission efficiency across three distinct fluid categories, namely traditional nanofluids, dual-hybrid, and tri-hybrid flow above an exponentially stretched surface under the action of uneven heat rise/fall effects. The original Problem is transformed into a boundary restricted model of a first-order Ordinary Differential Equation using the similarity method, and then tackled invoking the bvp5c MATLAB tool. The nature of the properties on streamlines and isotherms for various physical constraints on Motion and heat dissipation performance is illustrated in simple

diagrams. For the purpose of simplification, simultaneous solutions are provided for ternary hybrid, hybrid and simple nano-liquids.

The remainder of this paper is organized as follows. Section 2 presents the mathematical formulation of the physical model together with the governing equations and associated boundary conditions. Section 3 describes the similarity transformations, numerical methodology, and the evaluation of engineering quantities of interest. Section 4 discusses the numerical results and the physical interpretation of the effects of various governing parameters on the flow, thermal, and concentration fields. Finally, Section 5 summarizes the major findings and concluding remarks of the present study.

2. Mathematical modelling

Figure 1 illustrates the physical configuration of the present problem. A two-dimensional, steady, incompressible, electrically conducting ternary hybrid nanofluid flows over an exponentially stretching sheet. with stretching velocity $u = u_w = U_0 e^{x/l}$ and wall temperature $T(x) = T_\infty + T_0 e^{x/2l}$.

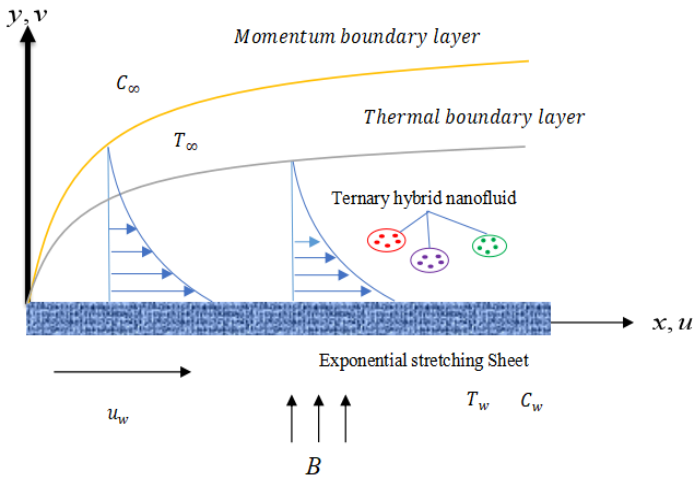

Figure 1. Flow configuration.

The x-axis is taken along the stretching surface, while the y-axis is normal to it. The sheet stretches with an exponential velocity, generating a boundary layer adjacent to the surface. A uniform transverse magnetic field is applied perpendicular to the flow direction. The surface is maintained at an exponentially varying temperature, whereas the ambient fluid is kept at a constant temperature. Thermal radiation, non-uniform heat source/sink, and chemical reaction effects are incorporated into the model. Under the boundary-layer approximations, the governing conservation equations are formulated and subsequently transformed into a system of ordinary differential equations using suitable similarity transformations.

The exponentially varying wall temperature is adopted to model practical manufacturing processes in which the heating intensity is intentionally varied along the stretching direction. Such thermal conditions arise in polymer extrusion, continuous metal strip processing, hot rolling, glass-fiber production, and coating technologies, where localized heaters, induction heating systems, or variable energy inputs generate non-uniform surface temperatures. Consequently, the exponential thermal boundary condition provides a physically meaningful representation of spatially varying heating encountered in industrial thermal processing and enables a realistic assessment of the resulting heat-transfer characteristics.

Considering the above-described conditions, the fundamental conservation equations for the fluid flow are formulated as stated below,

$$u_x + u_y = 0, \tag{1}$$

$$u(u_x) + v(u_y) = \frac{\mu_{tnf}}{\rho_{tnf}} u_{yy} - \frac{\sigma_{tnf}}{\rho_{tnf}} B_0^2 u, \tag{2}$$

$$uT_x + vT_y = \frac{k_{tnf}}{(\rho Cp)_{tnf}} T_{yy} + \frac{16\sigma^* T_\infty^3}{3k^* (\rho Cp)_{tnf}} T_{yy} + \frac{1}{(\rho Cp)_{tnf}} q''', \tag{3}$$

$$uC_x + vC_y = -Kr(C - C_\infty) + D_B C_{yy}, \tag{4}$$

with proper edge constraints

$$\left.\begin{array}{l} u = u_w = \dfrac{U_0}{e^{-x/l}}, v = 0,\ T = T_0,\ C = C_0 \quad \text{at } y = 0 \\ u \to 0,\ T \to T_\infty,\ C \to C_\infty \quad \text{as } y \to \infty \end{array}\right\}, \tag{5}$$

here [*u, v*] represent the flow velocity projections in the horizontal and vertical directions.

The material properties for the unary, hybrid, and tri-component nanofluid cases are defined as follows,

Property	**Nanofluid**
Viscosity	$\dfrac{\mu_{NF}}{\mu_F} = \left(1-\Phi_1\right)^{-2.5}$
Density	$\rho_{NF} = \rho_F\left(1-\Phi_1\right) + \rho_{P1}\Phi_1$
Specific heat capacity	$\left(\rho Cp\right)_{NF} = \left(\left(\rho Cp\right)_{P1} - \left(\rho Cp\right)_F\right)\Phi_1 + \left(\rho Cp\right)_F$
Thermal conductivity	$\dfrac{k_{NF}}{k_F} = \dfrac{2\left(k_F + k_{P1}\right) - k_{P1} - 2\Phi_1\left(k_F - k_{P1}\right)}{2\left(k_F + k_{P1}\right) - k_{P1} + \Phi_1\left(k_F - k_{P1}\right)}$
Electrical conductivity	$\dfrac{\sigma_{NF}}{\sigma_F} = \dfrac{\left(\sigma_{P1} + \sigma_F\right) + 2\Phi_1\left(\sigma_{P1} - \sigma_F\right)}{\left(\sigma_{P1} + \sigma_F\right) + \Phi_1\left(\sigma_F - \sigma_{P1}\right)}$

Property	**Hybrid nanofluid**
Viscosity	$\mu_{HNF} = \mu_F \dfrac{\left(1-\Phi_1\right)^{-2.5}}{\left(1-\Phi_2\right)^{2.5}}$
Density	$\dfrac{\rho_{HNF}}{\rho_F} = \left(1-\Phi_2\right)\left[\left(1-\Phi_1\right) + \Phi_1\dfrac{\rho_{P1}}{\rho_F}\right] + \Phi_2\left\{\dfrac{\rho_{P2}}{\rho_F}\right\}$
Specific heat capacity	$\dfrac{\left(\rho Cp\right)_{HNF}}{\left(\rho Cp\right)_F} = \left(1-\Phi_2\right)\left[\left(1-\Phi_1\right) + \Phi_1\dfrac{\left(\rho Cp\right)_{P1}}{\left(\rho Cp\right)_F}\right] + \Phi_2\dfrac{\left(\rho Cp\right)_{P2}}{\left(\rho Cp\right)_F}$
Thermal conductivity	$\dfrac{k_{HNF}}{k_{NF}} = \dfrac{k_{P2}\left(1+2\Phi_2\right) + 2k_{NF}\left(1+\Phi_2\right)}{k_{P2}\left(1-\Phi_2\right) + k_{NF}\left(2+\Phi_2\right)}$
Electrical conductivity	$\dfrac{\sigma_{HNF}}{\sigma_{NF}} = \dfrac{\left(\sigma_{P2} + \sigma_{NF}\right) + 2\Phi_2\left(\sigma_{P2} - \sigma_{NF}\right)}{\left(\sigma_{P2} + \sigma_{NF}\right) + \Phi_2\left(\sigma_{NF} - \sigma_{P2}\right)}$

Property	**Ternary hybrid nanofluid**
Viscosity	$\mu_{THNF} = \mu_F \dfrac{\left(1-\Phi_2\right)^{-2.5}}{\left(1-\Phi_1\right)^{2.5}\left(1-\Phi_3\right)^{2.5}} = A_1$
Density	$\dfrac{\rho_{THNF}}{\rho_F} = \left(1-\Phi_3\right)\left\{\left(1-\Phi_2\right)\left[\left(1-\Phi_1\right) + \Phi_1\dfrac{\rho_{P1}}{\rho_F}\right] + \Phi_2\dfrac{\rho_{P2}}{\rho_F}\right\} + \Phi_3\dfrac{\rho_{P3}}{\rho_F} = A_2$
Specific heat capacity	$\dfrac{\left(\rho Cp\right)_{THNF}}{\left(\rho Cp\right)_F} = \left(1-\Phi_3\right)\left\{\begin{array}{l}\left(1-\Phi_2\right)\left[\left(1-\Phi_1\right) + \Phi_1\dfrac{\left(\rho Cp\right)_{P1}}{\left(\rho Cp\right)_F}\right] \\ +\Phi_2\dfrac{\left(\rho Cp\right)_{P2}}{\left(\rho Cp\right)_F}\end{array}\right\} + \Phi_3\dfrac{\left(\rho Cp\right)_{P3}}{\left(\rho Cp\right)_F} = A_3$
Thermal conductivity	$\dfrac{k_{THNF}}{k_{HNF}} = \dfrac{k_{P3} + 2k_{HNF} - 2\Phi_3\left(k_{HNF} - k_{P3}\right)}{k_{P3} + 2k_{HNF} + \Phi_3\left(k_{HNF} - k_{P3}\right)}$
Electrical conductivity	$\dfrac{\sigma_{THNF}}{\sigma_{HNF}} = \dfrac{\left(\sigma_{P3} + \sigma_{HNF}\right) + 2\Phi_3\left(\sigma_{P3} - \sigma_{HNF}\right)}{\left(\sigma_{P3} + \sigma_{HNF}\right) - \Phi_3\left(\sigma_{P3} - \sigma_{HNF}\right)}$

The flow governing equations are altered by applying the following similarity aspects:

$$\left.\begin{aligned}
&\xi = e^{x/l},\ \eta = \sqrt{\frac{u_w}{2l\upsilon_f}}y, u = U_0 e^{x/l} F_\eta(\xi,\eta), u_w(x) = U_0 e^{x/l} \\
&v = -\sqrt{\frac{\upsilon_f U_0}{2l}} e^{\frac{x}{2l}} F(\xi,\eta) - \sqrt{\frac{2\upsilon_f U_0 \xi}{l}} \xi F_\xi(\xi,\eta) - y\frac{U_0}{2l}\xi F_\eta(\xi,\eta) \\
&\Theta = (T - T_\infty)(T_0 - T_\infty)^{-1},\ T(x) = T_\infty + T_0 e^{x/2l} \\
&\Psi = (C - C_\infty)(C_0 - C_\infty)^{-1},\ C(x) = C_\infty + C_0 e^{x/2l}
\end{aligned}\right\}, \tag{6}$$

Using Eq. (6), the nonlinear PDEs (2)-(4) are changed to the nonlinear ODEs as,

$$2(F_\eta^{\,2}) + 2\xi F_\eta(F_{\xi\eta}^2) = 2\xi(F_\xi)(F_{\eta\eta}) + \frac{1}{A_1 A_2}(F_{\eta\eta\eta}) - \frac{2}{A_2}\frac{\sigma_{tnf}}{\sigma_f}\frac{M}{\xi}F_\eta + F(F_{\eta\eta}), \tag{7}$$

$$\left.\begin{aligned}
A_3 \Pr\left[2\xi(F_\eta)(\Theta_\xi) + \Theta(F_\eta) - F(\Theta_\eta) - 2\xi(F_\xi)(\Theta_\eta)\right] = \left(\frac{k_{tnf}}{k} + Rd\right)(\Theta_{\eta\eta}) + \\
2\frac{k_{tnf}}{k_f} A_1 A_2 (F_\eta)(A^* F' + B^* \Theta)
\end{aligned}\right\}, \tag{8}$$

$$\xi F_\eta \Psi_\xi - \left(\frac{F}{2} + \xi F_\xi\right)\Psi_\eta = -k_0 \Psi + \frac{Sc}{2}(\Psi_{\eta\eta}), \tag{9}$$

The modified edge boundaries are,

$$\left.\begin{aligned}
&\frac{dF}{d\eta} = 1,\ F = -\xi\left(\frac{dF}{d\xi}\right),\ \Theta = 1, \Psi = 1, \text{ as } \eta = 0 \\
&\frac{dF}{d\eta} = 0,\ \Theta = 0, \Psi = 0 \quad as\ \ \eta \to \infty
\end{aligned}\right\}, \tag{10}$$

In the above Eqs. (7) – (9), the dimensionless constants $M, Pr, R\,d, Sc$ and q''' represent a magnetic field, Prandtl number, thermal radiation, Schmid number, and non-uniform heat source parameter, respectively. And given by the equation below,

$$\left.\begin{aligned}
&M = \frac{\sigma_F B_0^2 l}{U_0 \rho_F},\ \Pr = \frac{(\mu C_p)_F}{k_F},\ Rd = \frac{16\sigma^* T_\infty^3}{3k^* k_F},\ \text{Sc} = \frac{D_B}{\upsilon}, \\
&q''' = \frac{k_{tnf}}{x\upsilon_{tnf}} u[A^*(T_w - T_\infty) f' + B^*(T - T_\infty)]
\end{aligned}\right\}, \tag{11}$$

3. Methodological framework

To obtain a similarity solution, we consider the local boundary-layer approximation corresponding to the region where ξ <<1. Under this condition, the streamwise variations are much smaller than the transverse variations, and hence the derivative terms with respect to ξ become asymptotically negligible compared with the derivatives in the similarity variable. Consequently, the governing partial differential equations reduce to a system of ordinary differential equations representing the leading-order boundary-layer flow. Physically, this approximation is valid in the vicinity of the leading edge of the exponentially stretching surface, where the streamwise development of the boundary layer is relatively weak. Therefore, the present similarity solution should be interpreted as a local solution applicable within the range ξ <<1, rather than a global solution over the entire stretching surface.

In a comparable result, we take the derivative-bearing terms w.r.t. $\xi\,(i.e.(.)_\xi)$ in Eqs. (7) – (9) become minimal for ξ <<1 and prime denotes the ordinary derivative $\frac{d}{d\eta}$, Thus the Eqs. (7) – (9) become

$$\frac{1}{A_1 A_2} F''' - 2F'^2 + FF'' - \frac{2}{A_2}\frac{\sigma_{inf}}{\sigma_f}\frac{M}{\xi}F' - = 0, \tag{12}$$

$$\left(\frac{k_{tnf}}{k_f}+Rd\right)\Theta''+2\frac{k_{tnf}}{k_f}A_1A_2F'\left(A^*F'+B^*\Theta\right)-A_3\,\mathrm{Pr}\left(\Theta F'-F\Theta'\right)=0, \tag{13}$$

$$\frac{Sc}{2}\Psi''-k_0\Psi+\frac{F}{2}\Psi'=0, \tag{14}$$

with transformed edge conditions,

$$\left.\begin{aligned}&\frac{dF}{d\eta}=1,F=0,\Theta=1,\Psi=1,\ as\ \eta=0\\&\frac{dF}{d\eta}=0,\Theta=0,\Psi=0\ as\ \ \eta\to\infty\end{aligned}\right\}, \tag{15}$$

The dimensionless parameters of practical interest, specifically the surface drag coefficient, along with the rates of heat and mass transport, are formulated as:

$$\left.\begin{aligned}C_{fx}=\frac{\tau_w}{\rho_f U_w^2},\ \ Nu_x=\frac{2lq_w}{\left(T_w-T_\infty\right)k_f},\ \ Sh_x=\frac{xq_m\left(C_w-C_\infty\right)^{-1}}{D_B}\end{aligned}\right\}, \tag{16}$$

Wherein

$$\left.\begin{aligned}\tau_w=\mu_{tnf}\left(\frac{\partial u}{\partial y}\right)\Big|_{y=0},q_w=-\left(k_{tnf}+\frac{16\sigma^*T_\infty^3}{3k^*}\right)\left(T_y\right)\Big|_{y=0},q_m=-D_B\left(C_y\right)\Big|_{y=0}\end{aligned}\right\}, \tag{17}$$

Finally, we get

$$\left.\begin{aligned}&C_{fx}\,\mathrm{Re}_x^{1/2}=\frac{1}{A_1}f''(0),\\&Nu_x=-\mathrm{Re}_x^{1/2}\left(\frac{k_{tnf}}{k_f}+Rd\right)\theta'(0),\\&Sh_x=-\mathrm{Re}_x^{1/2}\frac{x}{2l}\phi'(0)\end{aligned}\right\}, \tag{18}$$

where $Re_x=\frac{2lU_w}{\upsilon_f}$ is the Reynolds number.

4. Numerical outcomes and discussion

In this segment, Eqs. (12) – (14), along with the edge restrictions (15). Numerically integrated utilizing the MATLAB bvp5c solver. The MATLAB package 'bvp5c' package is employed to achieve a numerical solution of the above equations. In this case, the higher-order differential equations are first converted into a system of first-order differential equations, and then the solutions are obtained. The step size represents the convergence criteria of the current study, $\Delta\eta=0.0001$, accurate to 5 decimal values. The inducement of non-dimensional constraints, viz., magnetic field (M), thermal radiative component (R), variable heat source (A^*, B^*), chemical response (kr), and Nanoparticle volume concentration (Φ) on rates of momentum, thermal, and mass flow is deliberated via plots. Further, these variables influence the surface drag coefficient, thermal, and mass transmission rate are depicted in tables for the Water + Al, Water + Al + AA7072, and Water + Al + AA7072 + AA7075 fluids. An analysis of the local Nusselt number for several physical factors is presented using a bar graph.

Figures 2–3 portray the significance of Mon momentum, energy and diffusion profiles for three diverse fluids under study. Evidently, temperature and mass curves are accelerating functions of M whereas velocity is a diminishing function. Physically, the added values of M develops a repulsive force, identified as Lorentz energy, in fluid flow. Owing to this, fluid velocity declines and temperature augments. The bearing of radiative heat flux on the thermal profiles is illustrated in Figure 4. We see that the swelling values of Rsupplies supplementation thermal energy to the fluid, making a thermal rise. It is very interesting to see that temperature distribution is more boosted in a ternary hybrid nanofluid.

Figures 5 and 6 reveal the responses of $A^*$and B^*on the temperature gradient. It is evident from the plots that the magnitudes of the temperature curves are elevated for the enhancement of both $A^*$and B^*. Generally, the upshot of $A^*$and B^*performances as energy originators due to this intensification in heat energy is noted. Figure 7 interprets the resteaverberation of Kr on the concentration gradient for three diverse working fluids. The rising

values of Kr causes a diminution in the molecular dispersion, which in turn reduces the concentration field. The implication of cumulative values of Φ on stream, thermal and concentration gradients are displayed in the Figures 8–10 respectively. Clearly, thermal and concentration gradients are amplified, but the velocity gradient decays. Physically, A higher concentration of nanoparticles elevates the fluid's internal friction, gives rise to reduced velocity and a concurrent expansion of the thermal and species concentration profiles. Figures 11–15 depict the Deviation in the Nusselt number for diverse range of M, R, A^*, B^* and Φ respectively.

The thermophysical characteristics of nanomaterials *Al*, *AA7072*, *AA7075*, and conventional liquid water are described in Table 1. Further, Tables 2, 3, and 4 portray the variation in the wall drag coefficient, rates of thermal and solute migration, respectively. It is observed that, C_{fx}, Nu_x and Sh_x diminishes with growing M. No change is recorded in the C_{fx} and Sh_x for enhancement in thermal radiation and uneven heat source parameters. Rate of energy transport in enhancing the volume fraction of the nanomaterial. More heat is transferred by ternary (*Water-Aluminium+AA7072+AA7075)* hybrid nanofluid in Correlation with the hybrid (*Water-Aluminium+AA7072*) nanofluid and mono (*Water-Aluminium*) nanofluid. The Species interaction constraint intensifies the rate of mass exchange. Furthermore, the mass transmission rate is much higher for the *Water-Aluminium+AA7072+AA7075* Tri-hybridized nanoliquid. Table 5 depicts the validation of the obtained results with the available literature for the limiting case and a good agreement between the results is witnessed.

Table 1. Thermal features of nano-additives and conventional liquid.

Property	***Water***	***Al***	***AA7072***	***AA7075***
$\rho\left(Kg/m^3\right)$	997.05	2712	2720	2810
$C_p\left(JKg^{-1}K^{-1}\right)$	4181.4	903	893	960
$k\left(Wm^{-1}K^{-1}\right)$	0.606	247	222	173
$\sigma\left(S/m\right)$	5.5X10^{-6}	3.5 X 10^{7}	34.83 X 10^{6}	26.77 X 10^{6}

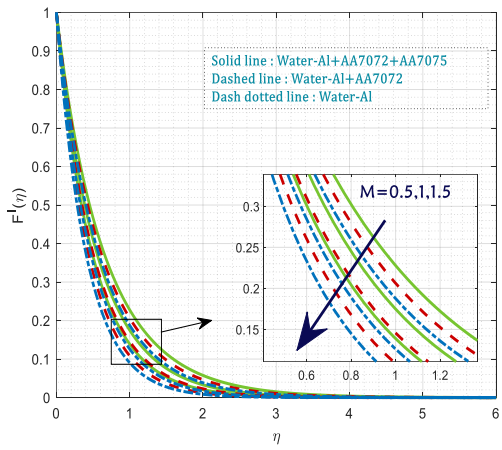

Figure 2. Result of M against $F^{|}(\eta)$.

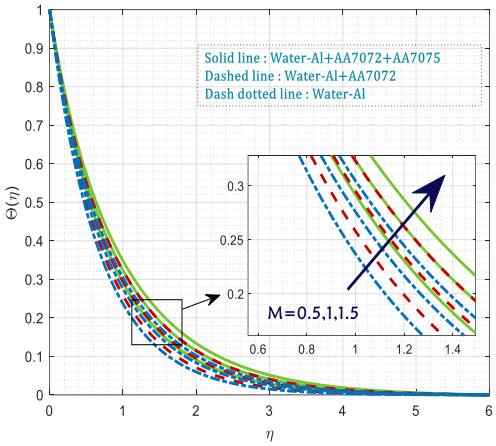

Figure 3. Result of M against $\Theta(\eta)$.

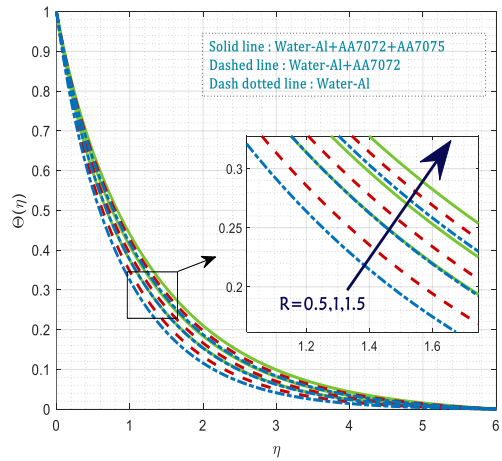

Figure 4. Result of R against $\Theta(\eta)$.

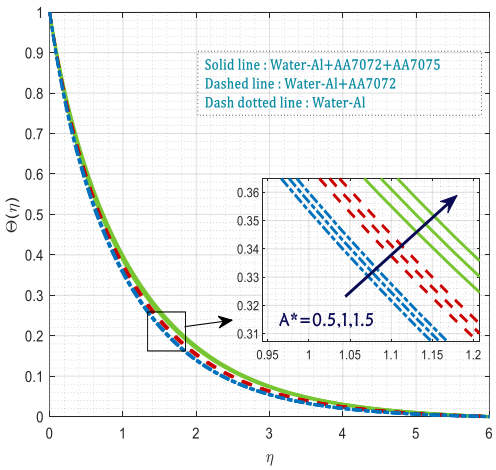

Figure 5. Result of A^* against $\Theta(\eta)$.

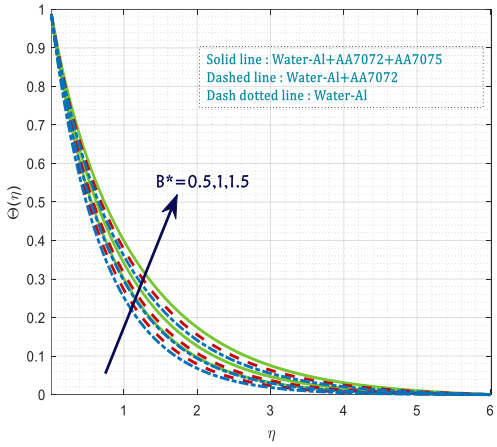

Figure 6. Result of B^* against $\Theta(\eta)$.

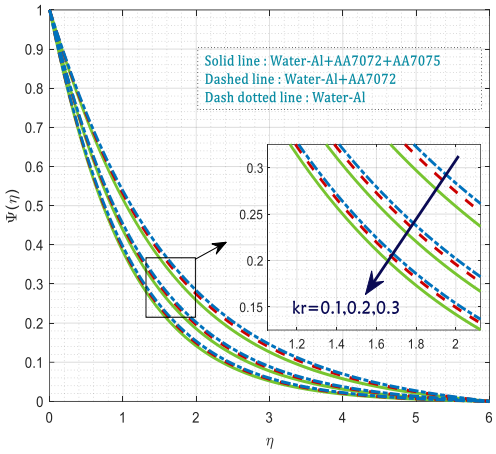

Figure 7. Effects of kr against $\Psi(\eta)$.

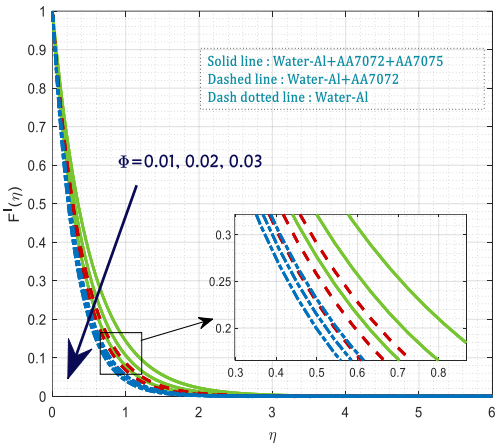

Figure 8. Effects of Φ against $F^{|}(\eta)$.

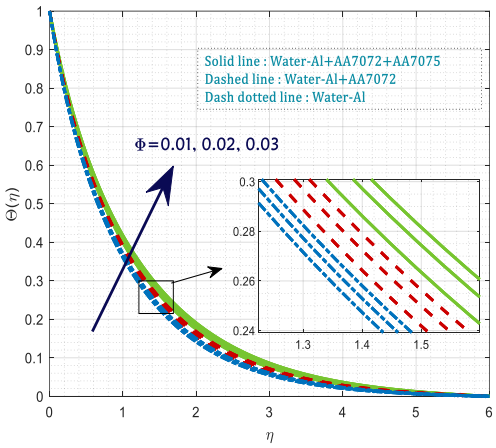

Figure 9. Outcome of Φ against $\theta(\eta)$.

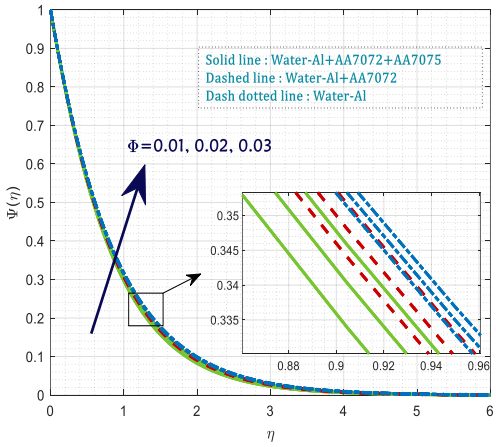

Figure 10. Outcome of Φ against $\Psi(\eta)$.

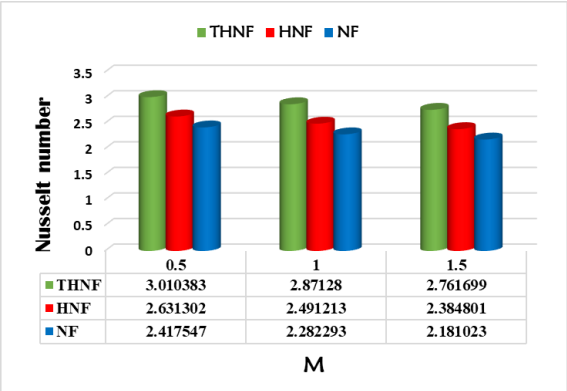

Figure 11. Variation in Nusselt number against M.

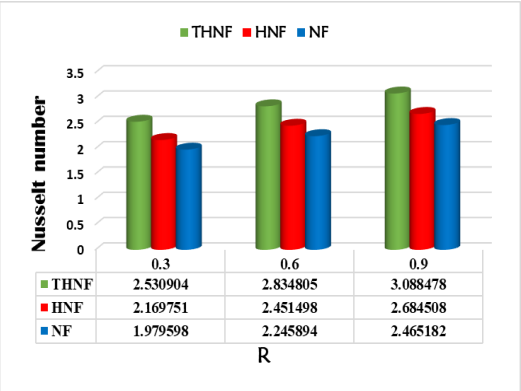

Figure 12. Nusselt number for distinct R.

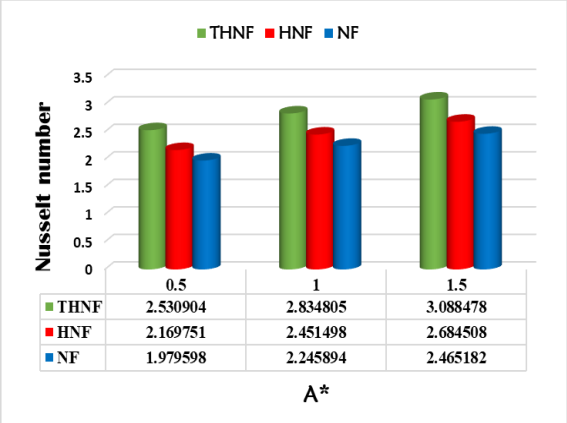

Figure 13. Nusselt Number against A^*.

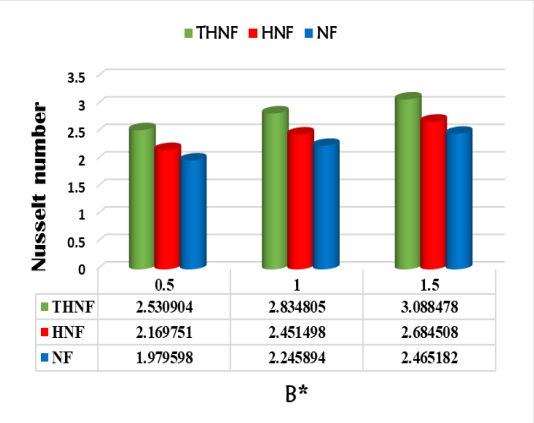

Figure 14. Nusselt Number for various B^*.

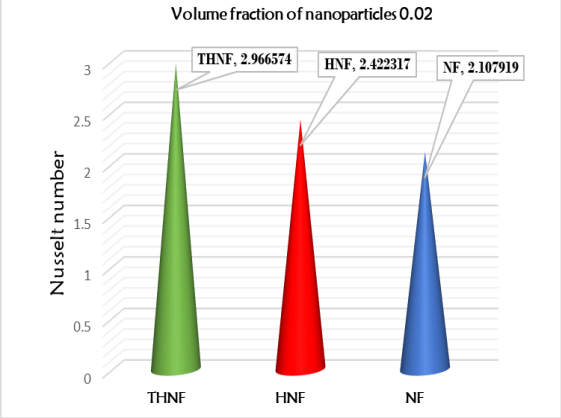

Figure 15. Heat transfer rate for $\Phi = 0.02$.

Table 2. Variation in wall friction component for ternary, hybrid and mono nanofluids.

M	Φ	Skin friction coefficient		
		Ternary nanofluid	Hybrid nanofluid	Nanofluid
0.5		-2.748644	-2.177712	-1.921859
1.0		-3.188708	-2.613745	-2.338142
1.5		-3.574249	-2.986274	-2.690366
	0.01	-4.537305	-3.895032	-3.542327
	0.02	-5.280849	-4.354013	-3.790477
	0.03	-6.165031	-4.868699	-4.054970

Table 3. Fluctuation in the local heat transport rate ternary, hybrid, and mono nanofluids.

M	R	A^*	B^*	Φ	Local Nusselt Number		
					Ternary nanofluid	Hybrid nanofluid	Nanofluid
0.5					3.010383	2.631302	2.417547
1.0					2.871280	2.491213	2.282293
1.5					2.761699	2.384801	2.181023
	0.3				2.457365	2.090379	1.895361
	0.6				2.565951	2.207112	2.018859
	0.9				2.665305	2.311656	2.127629
		0.5			2.530904	2.169751	1.979598
		1.0			2.681004	2.263682	2.052839
		1.5			2.831104	2.357614	2.126080
			0.5		2.530904	2.169751	1.979598
			1.0		2.834805	2.451498	2.245894
			1.5		3.088478	2.684508	2.465182
				0.01	2.530904	2.169751	1.979598
				0.02	2.735383	2.290178	2.041947
				0.03	2.966574	2.422317	2.107919

Table 4. Variation of Sherwood number for ternary, hybrid and mono nanofluids.

M	kr	Φ	Sherwood Number		
			Ternary nanofluid	Hybrid nanofluid	Nanofluid
0.5			1.150087	1.146000	1.142138
1.0			1.139427	1.132950	1.128119
1.5			1.131255	1.123506	1.118240
	0.1		0.613342	0.595992	0.585892
	0.2		0.774662	0.760972	0.752879
	0.3		0.904176	0.892554	0.885607
		0.01	1.114474	1.105241	1.099636
		0.02	1.117368	1.106793	1.100336
		0.03	1.121193	1.108836	1.101215

Table 5. Validation of obtained results for local Nusselt number.

Pr	Prakash et al. [33]	Present Results
0.2	0.17026	0.170262752
0.7	0.45445	0.454451586
2	0.91136	0.911368965
7	1.89540	1.895408935

5. Conclusion

An analytical assessment is undertaken to inspect the heat transport properties of nanofluid flow above exponential expansion of the boundary surface. The contribution of thermal radiation, molecular reaction, and nanoparticle volume fraction is also expounded.

The graphical results clearly demonstrate that the applied magnetic field suppresses the fluid velocity while enhancing the temperature and concentration distributions due to the Lorentz force. Thermal radiation and non-uniform heat generation significantly increase the thermal boundary-layer thickness, resulting in higher temperature profiles. An increase in the nanoparticle volume fraction improves the fluid's thermal performance but increases flow resistance due to the higher effective viscosity. Furthermore, the ternary hybrid nanofluid consistently exhibits superior heat-transfer performance compared with the hybrid and mono nanofluids, as evidenced by the temperature distributions and local Nusselt number plots. These observations confirm the effectiveness of ternary hybrid nanofluids in enhancing thermal transport in exponentially stretching surface applications.

Comprehensive results are contrasted for NF, HNF and THNF cases, yielding the following significant deductions.

- Improvements in the Lorentz force and nanomaterial density tend to reduce the wall shear stress, whereas no significant change is observed for additional thermal energy.
- An escalation in thermal radiation enhances the energy transfer rate, and this result is more significant in ternary mixed nanofluids as compared with mono and hybrid nanofluids.
- Also, the temperature is enhanced for augmenting values of uneven heat source and nanoparticle volume fraction factors.
- For lower frictional resistance of the flow, ternary hybrid nanofluid shows significant outcomes compared to the other two cases.
- The momentum and energy distributions are controllable via the Lorentz force and radiative heat transport.
- Considering three diverse solid nano-additives within the host medium is helpful for the augmented Energy transmission property of nanoliquids.

The author expresses his affectionate thanks to KSTePS DST, Government of Karnataka, India for the financial support under the grant (No. DST/KSTePS/Ph.D.Fellowship/MP-05/2024-25 dated 11th February 2025).

Acknowledgments

The authors state that no funding is involved.

Funding

The authors have no competing interests to declare that are relevant to the content of this article.

Conflict of interest

All authors contributed equally and approved the final manuscript.

Declaration of using AI tools

The authors declare that they have not used any type of generative artificial intelligence for the writing of this manuscript, nor for the creation of images, graphics, tables, or their corresponding captions.

References

[1] S. U. S. Choi and J. A. Eastman, “Enhancing thermal conductivity of fluids with nanoparticles,” ASME-Publications-Fed, vol. 66, pp. 99–105, 1995. 10.1115/IMECE1995-0926

[2] S. E. Ghasemi, M. Hatami, D. Jing, and D. D. Ganji, “Nanoparticles effects on MHD fluid flow over a stretching sheet with solar radiation: A numerical study,” J. Mol. Liq., vol. 219, pp. 890–896, 2016.

[3] M. R. Eid, “Chemical reaction effect on MHD boundary-layer flow of two-phase nanofluid model over an exponentially stretching sheet with a heat generation,” J. Mol. Liq., vol. 220, pp. 718–725, 2016.

[4] R. Ahmad, M. Mustafa, T. Hayat, and A. Alsaedi, “Numerical study of MHD nanofluid flow and heat transfer past a bidirectional exponentially stretching sheet,” J. Magn. Magn. Mater., vol. 407, pp. 69–74, 2016.

[5] C. Sulochana and G. P. Ashwinkumar, “Impact of Brownian moment and thermophoresis on the magnetohydrodynamic flow of magnetic nanofluid past an elongated sheet in the presence of thermal diffusion,” Multidiscip. Model. Mater. Struct., vol. 14, no. 4, pp. 744–755, 2018.

[6] Ashwinkumar, G. P., Ranjana, B., Sandeep, N., & Sulochana, C. Transpiration effect on magneto-flow of ternary hybrid nanofluid above an exponentially elongating sheet. Num. Heat Tran., Part B: Fundamentals, 2024; 1-18.

[7] Sandeep, N., P. Nanda, C. Sulochana, and G. P. Ashwinkumar. "Dynamics of Casson/Carreau hybrid nanofluid flow over a wedge with thermophoresis and Brownian motion effects." International Journal of Modelling and Simulation 2024; 1-12.

[8] Sandeep, N., U. Shivakumara, C. Sulochana, and G. P. Ashwinkumar. "Enhanced thermal conductivity of the Carreau nanoliquid by using Maxwell/Xue nanomodels." Num. Heat Tran., Part A: Applications (2024): 1-18.

[9] Sandeep, N., B. Ranjana, C. Sulochana, and G. P. Ashwinkumar. "Flow and heat transfer mechanism of engine-oil based hybrid nanofluid due to a nonlinearly extending surface: A comparative study." International Journal of Modelling and Simulation, 2023; 1-17.

[10] N. Sandeep, R. Suresh Babu, P. Nanda, and G. P. Ashwinkumar, "Enhanced heat transmission in conical slip flow of Walter'sB nanofluid," Int. J. Mod. Phys. B, vol. 38, no. 07, p. 2450096, 2024.

[11] S. S. Ghadikolaei, K. Hosseinzadeh, D. D. Ganji, and B. Jafari, "Hosseinzadeh, Ganji DD, Jafari B. Nonlinear thermal radiation effect on magneto Casson nanofluid flow with Joule heating effect over an inclined porous stretching sheet," Case Stud. Therm. Eng., vol. 12, pp. 176–187, 2018.

[12] D. Srinivasacharya and P. Jagadeeshwar, "Effect of Joule heating on the flow over an exponentially stretching sheet with convective thermal condition," Math. Sci., vol. 13, no. 3, pp. 201–211, 2019.

[13] M. N. Khan, S. Nadeem, N. Ullah, and A. Saleem, "Theoretical treatment of radiative Oldroyd-B nanofluid with microorganism pass an exponentially stretching sheet," Surf. Interfaces, vol. 21, p. 100686, 2020.

[14] A. M. Megahed, M. G. Reddy, and W. Abbas, "Modeling of MHD fluid flow over an unsteady stretching sheet with thermal radiation, variable fluid properties and heat flux," Math. Comput. Simul., vol. 185, pp. 583–593, 2021.

[15] E. Seid, E. Haile, and T. Walelign, "Multiple slip, Soret and Dufour effects in fluid flow near a vertical stretching sheet in the presence of magnetic nanoparticles," Int. J. Thermofluids, vol. 13, p. 100136, 2022.

[16] R. Biswas, S. Hossain, R. Islam, and S. Firoz, "Journal of Computational Mathematics and Data Science Computational treatment of MHD Maxwell nanofluid flow across a stretching sheet considering higher-order chemical reaction and thermal radiation," J. Comput. Math. Data Sci., vol. 4, p. 100048, 2022.

[17] M. A. Kumar and Y. D. Reddy, "Journal of the Indian Chemical Society Computational modelling of radiative Maxwell fluid flow over a stretching sheet containing nanoparticles with chemical reaction," J. Indian Chem. Soc., vol. 100, no. 1, p. 100877, 2023.

[18] M. Afrand, D. Toghraie, and B. Ruhani, "Effects of temperature and nanoparticles concentration on rheological behavior of Fe 3 O 4 -Ag / EG hybrid nanofluid : An experimental study," Exp. Therm. Fluid Sci., vol. 77, pp. 38–44, 2016.

[19] Z. Iqbal, E. Azhar, and E. N. Maraj, "Utilization of the computational technique to improve the thermophysical performance in the transportation of an electrically conducting Al 2 O 3 – Ag / H 2 O hybrid nanofluid," Eur. Phys. J. Plus, vol. 132, no. 544, p. 544, 2017.

[20] T. Hayat and S. Nadeem, "Results in Physics Heat transfer enhancement with Ag – CuO / water hybrid nanofluid," Results Phys., vol. 7, pp. 2317–2324, 2017.

[21] M. Usman, M. Hamid, T. Zubair, et al., "International Journal of Heat and Mass Transfer Cu-Al 2 O 3 / Water hybrid nanofluid through a permeable surface in the presence of nonlinear radiation and variable thermal conductivity via LSM," Int. J. Heat Mass Transf., vol. 126, pp. 1347–1356, 2018.

[22] I. Tlili, H. A. Nabwey, G. P. Ashwinkumar, and N. Sandeep, "3-D magnetohydrodynamic AA7072-AA7075/methanol hybrid nanofluid flow above an uneven thickness surface with slip effect," Sci. Rep., vol. 10, no. 1, p. 4265, Mar. 6 2020.

[23] W. Urmi, M. M. Rahman, and W. A. W. Hamazh, "An experimental investigation on the thermophysical properties of 40 % ethylene glycol based TiO 2 -Al 2 O 3 hybrid nanofluids," Int. Commun. Heat Mass Transf., vol. 116, p. 104663, 2020.

[24] P. S. P. Sudarsana and R. Ali, "Heat and mass transfer analysis of unsteady hybrid nanofluid flow over a stretching sheet with thermal radiation," SN Appl. Sci., vol. 2, no. 7, pp. 1–15, 2020.

[25] J. K. Madhukesh, K. R. Naveen, G. R. J. Punith, et al., "Numerical simulation of AA7072-AA7075 / water-based hybrid nanofluid flow over a curved stretching sheet with Newtonian heating : A non-Fourier heat flux model approach," J. Mol. Liq., vol. 335, p. 116103, 2021.

[26] S. Hazarika, S. Ahmed, and A. J. Chamkha, "Investigation of nanoparticles Cu, Ag and Fe3O4 on thermophoresis and vscous dissipation of MHD nanofluid over a stretching sheet in a porous Regime: A numerical modelling," Math. Comput. Simul., vol. 182, pp. 819–837, 2021.

[27] V. Puneeth, R. N. Anandika, S. Manjunatha, M. I. Khan, M. Imran Khan, A. Althobaiti, et al., "Muhammad. Implementation of modified Buongiorno's model for the investigation of chemically reacting rGo-Fe3O4-TiO2-H2O ternary nanofluid jet flow in the presence of bio-active mixers," Chem. Phys. Lett., vol. 786, p. 139194, 2022.

[28] K. Sarada, G. Fehmi, A. Amal, et al., "Case Studies in Thermal Engineering Impact of exponential form of internal heat generation on water-based ternary hybrid nanofluid flow by capitalizing non-Fourier heat flux model," Case Stud. Therm. Eng., vol. 38, p. 102332, 2022.

[29] S. Manjunatha, V. Puneeth, B. J. Gireesha, and A. J. Chamkha, "Theoretical Study of Convective Heat Transfer in Ternary Nanofluid Flowing past a Stretching Sheet," J. Appl. Comput. Mech., vol. 8, no. 4, pp. 1279–1286, 2022.

[30] N. Umar, S. Saleem, A. Al-Zubaidi, et al., "Thermal and mass species transportation in tri-hybridized Sisko martial with heat source over vertical heated cylinder," Int. Commun. Heat Mass Transf., vol. 134, p. 106003, 2022.

[31] S. A. Khan, T. Hayat, and A. Alsaedi, "Thermal conductivity performance for ternary hybrid nanomaterial subject to entropy generation," Energy Rep., vol. 8, pp. 9997–10005, 2022.

[32] F. Ali, A. Zaib, M. I. Khan, F. Alzahrani, and S. M. Eldin, "Irreversibility analysis in stagnation point flow of tri-hybrid nanofluid over a rotating disk; application of kinetic energy," J. Indian Chem. Soc., vol. 100, no. 2, pp. 2–5, 2023. 10.1016/j.jics.2022.100873

[33] D. G. Prakasha, M. V. V. N. L. Sudharani, K. G. Kumar, and A. J. Chamkha, "Comparative study of hybrid (graphene/magnesium oxide) and ternary hybrid (graphene/zirconium oxide/magnesium oxide) nanomaterials over a moving plate," Int. Commun. Heat Mass Transf., vol. 140, p. 106557, 2023.

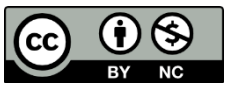

All open access articles published in Transactions on Computational Modeling and Intelligent Systems (http://tcmis.org) are distributed under the terms of the CC BY-NC 4.0 license (Creative Commons Attribution Non-Commercial 4.0 International Public License as currently displayed at http://creativecommons.org/licenses/by-nc/4.0/legalcode) which permits unrestricted use, distribution, and reproduction in any medium, for non-commercial purposes, provided the original work is properly cited.